



Strojniški vestnik

Journal of Mechanical Engineering

no. **9-10**
year **2023**
volume **69**



Strojniški vestnik – Journal of Mechanical Engineering (SV-JME)

Aim and Scope

The international journal publishes original and (mini)review articles covering the concepts of materials science, mechanics, kinematics, thermodynamics, energy and environment, mechatronics and robotics, fluid mechanics, tribology, cybernetics, industrial engineering and structural analysis.

The journal follows new trends and progress proven practice in the mechanical engineering and also in the closely related sciences as are electrical, civil and process engineering, medicine, microbiology, ecology, agriculture, transport systems, aviation, and others, thus creating a unique forum for interdisciplinary or multidisciplinary dialogue.

The international conferences selected papers are welcome for publishing as a special issue of SV-JME with invited co-editor(s).

Editor in Chief

Vincenc Butala
University of Ljubljana, Faculty of Mechanical Engineering, Slovenia

Technical Editor

Pika Škraba
University of Ljubljana, Faculty of Mechanical Engineering, Slovenia

Founding Editor

Bojan Kraut
University of Ljubljana, Faculty of Mechanical Engineering, Slovenia

Editorial Office

University of Ljubljana, Faculty of Mechanical Engineering
SV-JME, Aškerčeva 6, SI-1000 Ljubljana, Slovenia
Phone: 386 (0)1 4771 137
Fax: 386 (0)1 2518 567
info@sv-jme.eu, <http://www.sv-jme.eu>

Print: Demat d.o.o., printed in 240 copies

Founders and Publishers

University of Ljubljana, Faculty of Mechanical Engineering,
Slovenia
University of Maribor, Faculty of Mechanical Engineering,
Slovenia
Association of Mechanical Engineers of Slovenia
Chamber of Commerce and Industry of Slovenia,
Metal Processing Industry Association

President of Publishing Council

Mihael Sekavčnik
University of Ljubljana, Faculty of Mechanical Engineering, Slovenia

Vice-President of Publishing Council

Bojan Dolšak
University of Maribor, Faculty of Mechanical Engineering, Slovenia

International Editorial Board

Kamil Arslan, Karabuk University, Turkey
Hafiz Muhammad Ali, King Fahd U. of Petroleum & Minerals, Saudi Arabia
Josep M. Bergada, Politechnical University of Catalonia, Spain
Anton Bergant, Litostroj Power, Slovenia
Miha Boltežar, University of Ljubljana, Slovenia
Filippo Cianetti, University of Perugia, Italy
Janez Diaci, University of Ljubljana, Slovenia
Anselmo Eduardo Diniz, State University of Campinas, Brazil
Igor Emri, University of Ljubljana, Slovenia
Imre Felde, Obuda University, Faculty of Informatics, Hungary
Imre Horvath, Delft University of Technology, The Netherlands
Aleš Hribernik, University of Maribor, Slovenia
Soichi Ibaraki, Kyoto University, Department of Micro Eng., Japan
Julius Kaplunov, Brunel University, West London, UK
Iyas Khader, Fraunhofer Institute for Mechanics of Materials, Germany
Jernej Klemenc, University of Ljubljana, Slovenia
Milan Kljajin, J.J. Strossmayer University of Osijek, Croatia
Peter Krajnc, Chalmers University of Technology, Sweden
Janez Kušar, University of Ljubljana, Slovenia
Gorazd Lojen, University of Maribor, Slovenia
Darko Lovrec, University of Maribor, Slovenia
Thomas Lübben, University of Bremen, Germany
George K. Nikas, KADMOS Engineering, UK
Tomaž Pepelnjak, University of Ljubljana, Slovenia
Vladimir Popović, University of Belgrade, Serbia
Franci Pušavec, University of Ljubljana, Slovenia
Mohammad Reza Safaei, Florida International University, USA
Marco Sortino, University of Udine, Italy
Branko Vasić, University of Belgrade, Serbia
Arkady Voloshin, Lehigh University, Bethlehem, USA

General information

Strojniški vestnik – Journal of Mechanical Engineering is published in 6 double issues per year.

Institutional prices include print & online access: institutional subscription price and foreign subscription €100,00 (the price of a single issue is €10,00); general public subscription and student subscription €50,00 (the price of a single issue is €5,00). Prices are exclusive of tax. Delivery is included in the price. The recipient is responsible for paying any import duties or taxes. Legal title passes to the customer on dispatch by our distributor. Single issues from current and recent volumes are available at the current single-issue price. To order the journal, please complete the form on our website. For submissions, subscriptions and all other information please visit: <http://www.sv-jme.eu>.

You can advertise on the inner and outer side of the back cover of the journal. The authors of the published papers are invited to send photos or pictures with short explanation for cover content.

We would like to thank the reviewers who have taken part in the peer-review process.

The journal is subsidized by Slovenian Research and Innovation Agency.

Strojniški vestnik - Journal of Mechanical Engineering is available on <https://www.sv-jme.eu>.



Cover:
The testing rig for cutting of materials by Abrasive Water Jet is presented. The image shows a real view of the cutting process. Shown here is the workpiece fixed on the grid and subjected to AWJ at the initial cutting stage, exactly now of the first contact of the jet with the workpiece.

Image Courtesy:
Andrzej Perec, et al.
Jacob of Paradies University
Faculty of Technology
Poland

ISSN 0039-2480, ISSN 2536-2948 (online)

© 2023 with Authors.

SV-JME is indexed / abstracted in: SCI-Expanded, Compendex, Inspec, ProQuest-CSA, SCOPUS, TEMA. The list of the remaining bases, in which SV-JME is indexed, is available on the website.

Contents

Strojniški vestnik - Journal of Mechanical Engineering
volume 69, (2023), number 9-10
Ljubljana, September-October 2023
ISSN 0039-2480

Published every two months

Papers

Andrzej Perec, Elżbieta Kawecka, Aleksandra Radomska-Zalas, Frank Pude: Optimization of Abrasive Waterjet Cutting by Using the CODAS Method with Regard to Interdependent Processing Parameters	367
Dragan Rodić, Marin Gostimirović, Milenko Sekulić, Borislav Savković, Andjelko Aleksić: Fuzzy Logic Approach to Predict Surface Roughness in Powder Mixed Electric Discharge Machining of Titanium Alloy	376
Jamuna Elangandhi, Suresh Periyagounder, Mahalingam Selavaraj, Duraisivam Saminatharaja: Mechanical and Microstructural Properties of B4C/W Reinforced Copper Matrix Composite Using a Friction Stir-Welding Process	388
Amjad Alsakarneh, Lina Momani, Taha Tabaza: Fuzzy and Matlab/Simulink Modelling of the Air Compression Refrigeration Cycle	401
Qun Ma, Xiangwei Zhang: Research on an Analytical Method for the Forming Force of External Spline Cold Roll-Beating	409
Longfei Li, Xin He, Taowei Jiao, Yumeng Xiao, Xipan Wei, Wei Li: Design and Optimization of an Umbrella-Type Shield Based on 3D CFD Simulation Technology	422

Optimization of Abrasive Waterjet Cutting by Using the CODAS Method with Regard to Interdependent Processing Parameters

Andrzej Perec^{1,*} – Elżbieta Kawecka¹ – Aleksandra Radomska-Zalas¹ – Frank Pude^{2,3}

¹ Jacob of Paradies University, Faculty of Technology, Poland

² Steinbeis Consulting Center High-Pressure Waterjet Technology, Germany

³ Inspire AG, ETH Zurich, Switzerland

The paper shows performance optimization effects of steel machining by abrasive water jet (AWJ). An innovative combinative distance-based assessment method (CODAS) is implemented for the optimization of cutting parameters like pump pressure, feed rate, and abrasive flow rate over cutting depth, and cut kerf surface roughness. The CODAS algorithm is among those based on measuring the distance between a scenario (in this case processing parameters in terms of performance and quality indicators) - and a certain benchmark. A benchmark is a specific hypothetical set of processing parameters devised or determined from available data. To determine the best set of process control parameters, a CODAS approach was performed with some weighting determinations. To set the initial parameters of the weights, it was proposed to calculate based on entropy weight method (EWM), that measures output value dispersion in cutting process. This technique simplifies multiple compound responses by preserving a single response.

Keywords: abrasive waterjet cutting, process optimization, CODAS method, maximum cutting depth, minimum surface roughness welding, copper, metal matrix composite, boron carbide

Highlights

- Effect of jet pressure, traverse speed, and mass flow rate of on chromium-nickel-molybdenum steel cut surface roughness was introduced.
- An optimal set of control parameters to reach the highest cutting depth and smallest surface roughness of cut kerf was determined.
- A significant abasement in the cost of the experiments by diminution the number of required tests and shortening the time to perform with high precision of results was reached.

0 INTRODUCTION

Optimization of control parameters is used wherever many control parameters significantly affect the result. Examples include advanced industrial processes like epoxidation [1], polymerization [2], and advanced manufacturing technologies [3] to [5].

The cutting with an abrasive waterjet (AWJ) is one of the imported methods classified as advanced manufacturing technology. It is used in many industries, including aerospace [6] and [7] automotive [8], manufacturing [9] and [10] and even in medicine [11] to [13]. However, a poorly designed process can be costly and time-consuming and optimizing it can ensure that it is as efficient, quality [14] and [15] and effective as possible.

Optimizing the control parameters of AWJ machining process is essential for achieving the desired cutting results with maximum efficiency, quality, and minimum waste. The control parameters optimization of the AWJ machining process can be achieved by using statistical methods such as design of experiments (DOE), especially Taguchi

method [16], response surface methodology (RSM) [4], artificial intelligence techniques such as neural networks and genetic algorithms, expert systems, and approximate metaheuristic methods. These methods can help identify the optimal combination of control parameters that maximize the desired cutting results, reduce waste, and improve efficiency.

There are also methods from the field of decision support or multi-criteria decision-making (MCDM) that can be successfully used to optimize the AWJ process [17] and [18].

The CODAS method is a valuable tool for solving MCDM problems. It allows to consider multiple criteria simultaneously and to balance the trade-offs between them. The method can be used in fields such as mechanical engineering, among others.

The entropy-CODAS method belongs to a multi-criteria decision-making technique used for optimization of chosen problems. It is based on the concept of entropy, which is a measure of uncertainty or disorder. The basic idea behind the method is to minimize the overall distance between the alternatives

and the ideal solution while maximizing the diversity among the alternatives.

An innovative entropy-CODAS method is implemented for the optimization of cutting depth, cut surface roughness, and angle of cut kerf was conducted.

The dimension and distribution of the used abrasive grains have a noteworthy influence on the efficiency of the cutting process by AWJ. In the cutting head takes place the intensive disintegration of abrasive materials during the creation of the abrasive jet. The disintegration of chosen abrasive materials grains was tested after forming in the cutting head [19] and [20]. Additionally, it allows to carry out recovery analysis for the recycling possibility.

Hlavacova et al. [21] introduced the study of common quality steels cut by AWJ and observed the relations concerning the mechanical characteristics of quenched steels and the chosen surface roughness parameters. The differentiation of the steel microstructure was the essential property for the cutting quality because the higher the difference in the hardness of the structural constituents in the inhomogeneous microstructure was, the higher were the surface roughness values after cutting.

Perec and Musial [22] conducted research on the use of one of the methods based on decision support, namely the VIKOR method for optimizing the parameters of wear-resistant structural steel cutting by AWJ.

However, Perec et al. [23] modeled and optimized the AWJ cutting process of tool steel based on the RSM.

Other possibility of hard material machining presented Kumari and Acherjee [24]. Authors concentrated on using criteria importance through inter-criteria correlation (CRITIC) and CODAS multicriteria decision-making methods to assess the performance of proposed approach while selecting the best advanced machining process for machining titanium from the eight most often used as AWJ machining, ultrasonic machining, chemical machining, electron beam machining, laser beam machining, electrochemical machining, electro discharge machining, and plasma arc machining. Material removal rate, shape feature, work material type, tolerance and surface finish, power requirement, and cost were the criteria used to evaluate and pick the best advanced manufacturing process.

Sivalingam et al. [25] investigated the effect of cutting process parameters on Inconel 718 alloy turning in dry and (atomized spray cutting fluid) ASCF cutting environments. The cutting parameters

were adjusted using desirability functional analysis, and two types of MCDM methods were investigated: additive ratio assessment method (ARAS) and CODAS. Both MCDM approaches yielded identical results in the form of minimal surface roughness, machining cost, power consumption and maximizing tool life, compared with dry machining.

Al-Tamimi and Sanjay [26] presented an intelligent machining model which used contemporary techniques, based on CODAS and several other as artificial neural network (ANN), adaptive neuro-fuzzy inference systems, and particle swarm optimization (ANFIS-PSO) approach for minimizing resulting force, specific cutting energy, and maximizing metal removal rate in superalloys machining.

Malaga et al. [27] presented study tended to identify the proper material for metal additive manufacturing, using MCDM approach. Information entropy method (IEM) and CODAS were taken to establish the priority order of materials. The meaningful material properties were used as the material criterium for the analysis. The decision-making techniques were deployed using real data of materials.

Sivalingam et al. [28] also presented the CODAS multi-criteria decision-making techniques and additive ratio assessment method for predicting the internal combustion engine radiator performance under 27 different operating conditions using multiwall carbon nanotubes based nanofluid. The outcomes of the regression analysis designated those substantial input factors for enhancing thermal transfer with this radiator.

Due to the difficulties in the milling of steel and the difficulty in the proper selection of cutting tools, cutting conditions and parameters of the cutting process, Abas et al. [29] performed a multi-response optimization using a CODAS method in combination with criteria importance through inter-criteria correlation (CRITIC) with satisfactory results.

The CODAS method can be also used for support of optimal selection for example supplier selection [30], wind energy plant location selection [31], dam construction material selection [32], and for sustainable material selection in construction projects with incomplete weight information [33].

Krajcarz and Spadlo [34] published experimental research of the geometric accuracy of cylindrical holes made by a high-pressure jet of water. The tests were conducted according to a three-level Box-Behnken design. Changes in the input parameters during high-pressure abrasive water jet cutting resulted in the occurrence of geometric inaccuracies. The values of

the correlation coefficient confirmed that the greatest influence of the cylindrical holes was cutting speed.

The state of art includes assorted studies on the optimization of cutting parameters, including cutting depth, cut surface roughness, and angle of cut kerf, using different methods such as entropy-CODAS, VIKOR, RSM, and multicriteria decision-making techniques like CODAS, ARAS, and desirability functional analysis. These studies focused on cutting types of materials, such as common quality steels, wear-resistant structural steel, tool steel, Inconel 718 alloy, and superalloys. Additionally, it can be observed that the CODAS method was also applied to other fields.

However, to date, the CODAS method has not been used in the optimization of AWJ machining, which defines a research gap and an area for potentially new research.

The objective of this paper is to utilize entropy-CODAS to gain an optimal combination of control parameters for maximum cutting depth and minimum surface roughness and to uncover the individual result of each control parameter on cutting depth, width of the cut kerf and its surface roughness.

1 MATERIALS

1.1 Abrasive Materials

As abrasive material the crushed rock garnet type J80A from Jinhong Mining located in Jiangsu, China was used. A sample view of grain shape and grain size distribution is presented in Fig. 1.

From the details of the mineral content shown in Table 1, more than 90 % of this type of garnet is Almandine.

Almandine belongs to the silicate mineral group as part of the larger garnet group, which includes several other types of minerals with similar crystal structures. It has the chemical formula $Fe_3Al_2(SiO_4)_3$, which shows it contains both iron (Fe), aluminum (Al), and silicon (Si) atoms.

Almandine is typically found in metamorphic rocks such as mica schists, gneisses, and amphibolites. It is usually red to reddish-brown in color, although it can also appear purple or black. Almandine is a hard mineral with a Mohs hardness over 7.5, making it suitable for use as an abrasive material. Other properties are shown in Table 2.

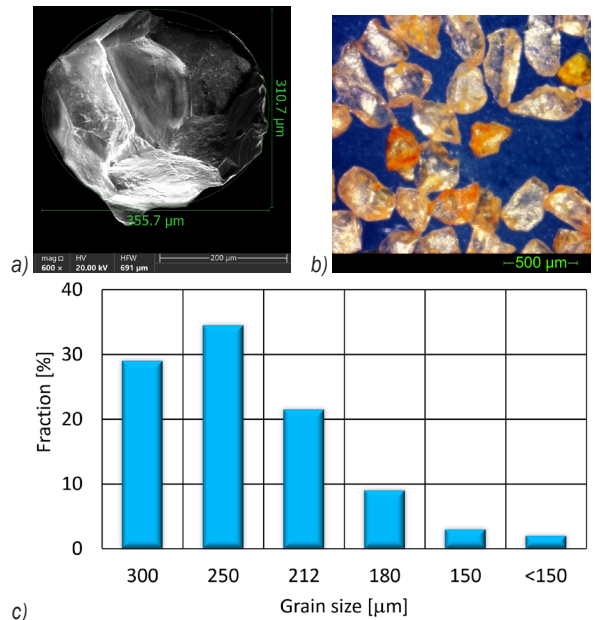


Fig. 1. Garnet abrasive grains: a) SEM view; b) optical microscope view; and c) grain size distribution

Table 1. Garnet chemical properties

Chemical composition [%]							
Fe ₂ O ₃	SiO ₂	TiO ₂	Al ₂ O ₃	FeO	CaO	MgO	MnO
17	39	0.05	21	8	9.5	5	0.4
Mineral content [%]							
Amandine	Ilmenite	Omphacite	Rutile	Quartz	Hornblende	Silica	
90-96	1.0	1.5	0.6	<0.1	<0.5	<0.5	

Table 2. Garnet physical properties

Size	Unit	Value
Density	[kg/dm ³]	3.8-4.1
Bulk gravity	[kg/dm ³]	2.3-2.4
Mohs hardness		7.5-8.0
Conductivity	[S/m]	<25
Acid solubility (HCL)	[%]	<1.0
Grain shape		Sub angular

In addition to its use as an abrasive, almandine is also used as a gemstone because of its deep red color and durability.

1.2 Cut Material

As target material 18CrNiMo7-6 steel for medium to high core strength engineering applications up to 62 HRC when carburized, hardened, and tempered was chosen to be cut. In this steel chromium-nickel-molybdenum were used as strengthening agents (Table 3).

Table 3. 18CrNiMo7-6 steel chemical composition [34]

[%]	C	Si	Mn	P	S	Cr	Ni	Mo	Cu
min	0.15	0.15	0.5	-	-	1.5	1.4	0.25	-
max	0.21	0.4	0.9	0.02	0.02	1.8	1.7	0.35	0.4

It is a high hardenability, high toughness case-hardening steel, generally supplied in the annealed condition.

It can also be used in uncarburized form as a high tensile steel, which when suitably hardened and tempered can be utilized for various applications requiring good tensile strength and toughness.

Despite difficult to cut is used extensively by all industry sectors for components and shafts requiring high surface wear resistance, high core strength and impact properties. The strength properties are presented in Table 4.

Table 4. 18CrNiMo7-6 steel typical mechanical properties [35] and [36]

Youngs module [GPa]	Poisson's ratio	Shear module [GPa]	Density [kg/m ³]	Tensile strength [MPa]	Yield strength [MPa]
210	0.3	80	7800	700	520

2 EXPERIMENTAL

2.1 Test Rig and Test Method

The cutting tests were carried out on the WaterJet CNC OMAX 60120 machining center (Fig. 2).

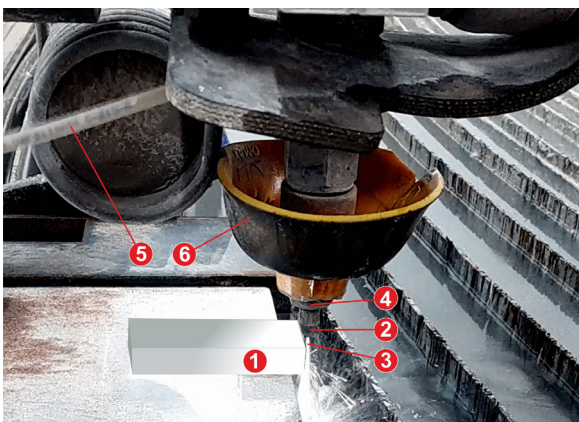


Fig. 2. AWJ cutting process: 1) target material, 2) focusing tube, 3) AWJ, 4) cutting head, 5) abrasive inlet, and 6) cutting head cover

The materials were cut by perpendicular to the workpiece directed AWJ, and a linear moving with a specific traverse speed. The thickness of the samples was selected to prevent complete separation of

material and an accurate determination of the cutting depth accordingly.

The process of AWJ 18CrNiMo7-6 steel cutting was conducted using the following parameters:

- pressure: 360 MPa; 380 MPa; 400 MPa,
- traverse speed: 50 mm/min; 150 mm/min and 250 mm/min,
- the abrasive flow rate: 250 g/min; 350 g/min and 450 g/min,
- abrasive material; garnet #80 (from crushed rock),
- water nozzle ID: 0.33 mm,
- focusing tube ID: 0.76 mm,
- stand-off distance: 2 mm.

2.1.1 Cut Kerf Geometry

The effect of the AWJ on the material is a cut kerf. Its details are shown in Fig. 3a and the actual view in Fig. 3b. The depth of the cut groove is denoted as h_c , its width as W_t , at top and W_b at bottom, and the angle of kerf inclination as δ .

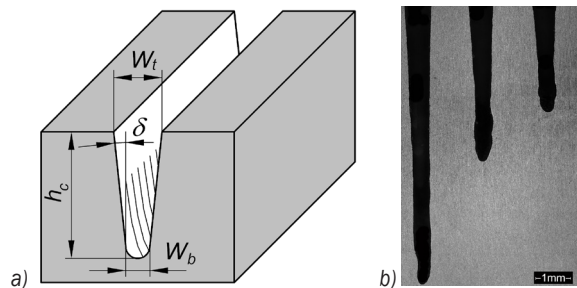


Fig. 3. Cut kerf dimensions: a) schematic, and b) optical microscope view

2.1.2 Surface Roughness

For roughness measurement the Sk_u (kurtosis) was chosen. This parameter expands the profile (line roughness) parameter Rku three dimensionally. Sk_u is used to evaluate sharpness in the height distribution [37]. It is calculated from the following equation:

$$Sk_u = \frac{1}{Sq^4} \left(\frac{1}{A} \iint_A Z^4(x, y) dx dy \right). \quad (1)$$

This parameter concerns the height distribution and is suitable for evaluating the abrasion, when (Fig. 4):

- $Sk_u = 3$: normal distribution,
- $Sk_u > 3$: height distribution is sharp, and
- $Sk_u < 3$: height distribution is even.

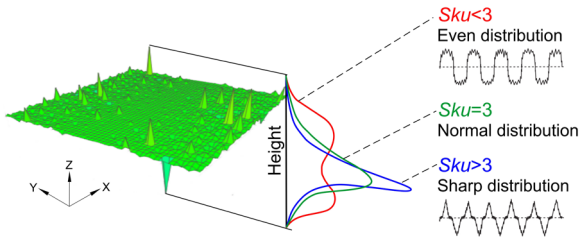


Fig. 4. *Sku roughness parameter details*

Roughness measurements were made on the high-definition Olympus DSX1000 optical microscope. The measurement area was set as $953 \mu\text{m} \times 953 \mu\text{m}$. Its location is shown in Fig. 4. The measurement signal was filtered with the Gaussian filter.

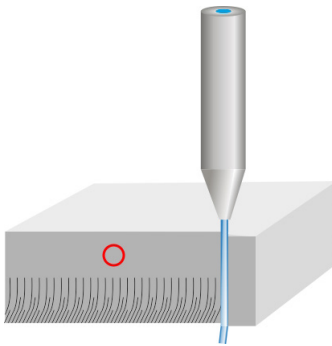


Fig. 5. *Cut kerf roughness measurement location*

2.2 CODAS Method

Combinative distance-based assessment (CODAS) is a multi-criteria decision-making method that was introduced in a paper by Ghorabaceet al. [38]. CODAS algorithm belongs to the class of those based on measuring the distance between a scenario (in our case, it will be the processing parameters in terms of performance and quality indicators), and a certain benchmark.

A benchmark is a certain hypothetical set of processing parameters, imagined or determined from available data. The idea behind the CODAS method is as follows: we are looking for a worst-case scenario, a negative ideal. We check how far each scenario (each set of machining parameters) is distanced from this worst-case scenario in the Euclidean sense. The farther away a set of parameters is from the counter-ideal, the better it is (and vice-versa).

In CODAS, we are interested in the negative ideal. First measure of this method is the distance of the scenario from this negative ideal is checked here, and this distance is calculated using the Euclidean metric. It is this metric that we consider the most

intuitive: the square root of the sum of the squares of the differences of the values of the corresponding coordinates.

The secondary measure is the taxicab distance which is related to the indifference space. The taxicab distance equation is grounded on the concept that the length between two points is determined by following a grid, rather than following a straight line. The equation is the sum of the absolute value of the difference of x values and the absolute value of the difference of y values.

The steps of the proposed CODAS method are presented as follows:

Step 1. Construct the decision-making matrix (\mathbf{X}), shown as follows:

$$\mathbf{X} = \begin{bmatrix} x_{11} & x_{12} & \dots & x_{1m} \\ x_{21} & x_{22} & \dots & x_{2m} \\ \vdots & \vdots & \ddots & \vdots \\ x_{n1} & x_{n2} & \dots & x_{nm} \end{bmatrix}, \quad (2)$$

where x_{ij} ($x_{ij} \geq 0$) denotes the performance value of j^{th} alternative on j^{th} criterion ($i \in \{1, 2, \dots, n\}$ and $j \in \{1, 2, \dots, m\}$).

Step 2. Calculate the normalized decision matrix. We use linear normalization of performance values as follows:

$$n_{ij} = \begin{cases} \frac{x_{ij}}{\max_i x_{ij}} & \text{if } j \in N_b \\ \frac{\min_i x_{ij}}{x_{ij}} & \text{if } j \in N_c \end{cases}, \quad (3)$$

where N_b and N_c represent the sets of benefit and cost (non-beneficial) criteria, respectively.

Step 3. Calculate the weighted normalized decision matrix. The weighted normalized performance values are calculated as follows:

$$r_{ij} = w_j \cdot n_{ij}, \quad (4)$$

where w_j ($0 < w_j < 1$) denotes the weight of j^{th} criterion, and

$$\sum_{j=1}^m w_j = 1. \quad (5)$$

To establish the entropy factor ($e_{i,j}$) exploiting the projection value of the alternative, the equation looks as follow:

$$e_{i,j} = -\frac{1}{\ln m} \sum_{i=1}^n T_{i,j} \ln T_{i,j}, \quad (6)$$

and the entropy weight of the j^{th} index is determined by equation:

$$w_i = \frac{1 - e_{i,j}}{\sum_{i=1}^n (1 - e_{i,j})} \tag{7}$$

This entropy technique was used to determine the level of individual weights. In this technique, the number of choices, and different criteria get to appraise multiple criteria optimizations on basis establishing a comparative decision matrix. If the number of choices (mass flow rate, pressure, and feed rate) getting as ‘M’, and the numbers of conditions are cutting depth surface rough-ness and angle of cut kerf get as ‘N’ then relative decision matrix having a dimension of M×N.

Step 4. Determine the negative-ideal solution as follows:

$$ns = [ns_j]_{1 \times m}, \tag{8}$$

$$ns_j = \min_i r_{ij}. \tag{9}$$

Step 5. Calculate the Euclidean and taxicab distances of alternatives from the negative-ideal solution, shown as follows:

$$E_i = \sqrt{\sum_{j=1}^m (r_{ij} - ns_j)^2}, \tag{10}$$

$$T_i = \sqrt{\sum_{j=1}^m |r_{ij} - ns_j|}. \tag{11}$$

Step 6. Construct the relative assessment matrix, shown as follows:

$$Ra = [h_{ik}]_{n \times m}, \tag{12}$$

$$h_{ik} = E_i - E_k + (\psi (E_i - E_k) \times (T_i - T_k)), \tag{13}$$

where $k \in \{1, 2, \dots, n\}$ and ψ denotes a threshold function to recognize the equality of the Euclidean distances of two alternatives, and is defined as follows:

$$\psi(x) = \begin{cases} 1 & \text{if } |x| \geq \tau \\ 0 & \text{if } |x| < \tau \end{cases} \tag{14}$$

where τ is the threshold parameter that can be set by decisionmaker. It is suggested to set this parameter at a value between 0.01 and 0.05. If the difference between Euclidean distances of two alternatives is less than τ , these two alternatives are also compared by the taxicab distance. In this study for the calculations was used $\tau=0.02$.

Step 7. Calculate and rank the alternatives according to the decreasing values of assessment score (H_i):

$$H_i = \sum_{k=1}^n h_{ik}. \tag{15}$$

The alternative with the highest H_i factor is the best choice among the alternatives.

3 RESULTS AND DISCUSSION

The results shown in Table 5, while Table 6 displays the calculation effects of the normalizing, weighted normalized performance values, Euclidean and taxicab distances of alternatives, assessment score factor and their ranks.

Table 5. Cutting process tests results

No	AFR	p	Vp	hc	Sku
1	250	360	50	7.48	2.57
2	250	380	150	5.09	3.01
3	250	400	250	2.93	2.63
4	350	360	150	4.99	3.72
5	350	380	250	3.06	2.65
6	350	400	50	8.70	2.46
7	450	360	250	3.31	2.66
8	450	380	50	7.59	3.83
9	450	400	150	4.89	2.65

Table 6. CODAS coefficients and rank

No	Ri(b)	Ri(nb)	Ei	Ti	H	Rank
1	0.55	0.35	0.35	0.36	1.23	2
2	0.37	0.29	0.17	0.31	-0.42	5
3	0.22	0.34	0.11	0.35	-1.20	9
4	0.37	0.24	0.15	0.25	-0.58	6
5	0.23	0.33	0.10	0.35	-1.02	8
6	0.64	0.36	0.44	0.38	2.03	1
7	0.24	0.33	0.11	0.35	-1.00	7
8	0.56	0.23	0.34	0.25	1.14	3
9	0.36	0.33	0.18	0.35	-0.36	4

The calculated H_i represents the better the status, the higher values it takes. Out of all H_i value in the frame of the reference sequence is the best combination of parameters and is thereby recommended.

For these tests, the recommended values for control parameters (highlighted row in Table 6) are as follows:

- abrasive feed rate: 350 g/min,
- pressure: 400 MPa,
- traverse speed: 50 mm/min.

Examples of the effects of machining with the control parameters optimally determined by this method are shown in Fig. 5. Numerous traces of erosion of the material by abrasive grains were observed here. They become visible in the form of parallel machining footprints. They are visible especially in Fig. 6a in the form of parallel lines located on macrograins, at an acute angle. There is no chaotic arrangement of traces on adjacent grains, which indicates good cutting conditions.

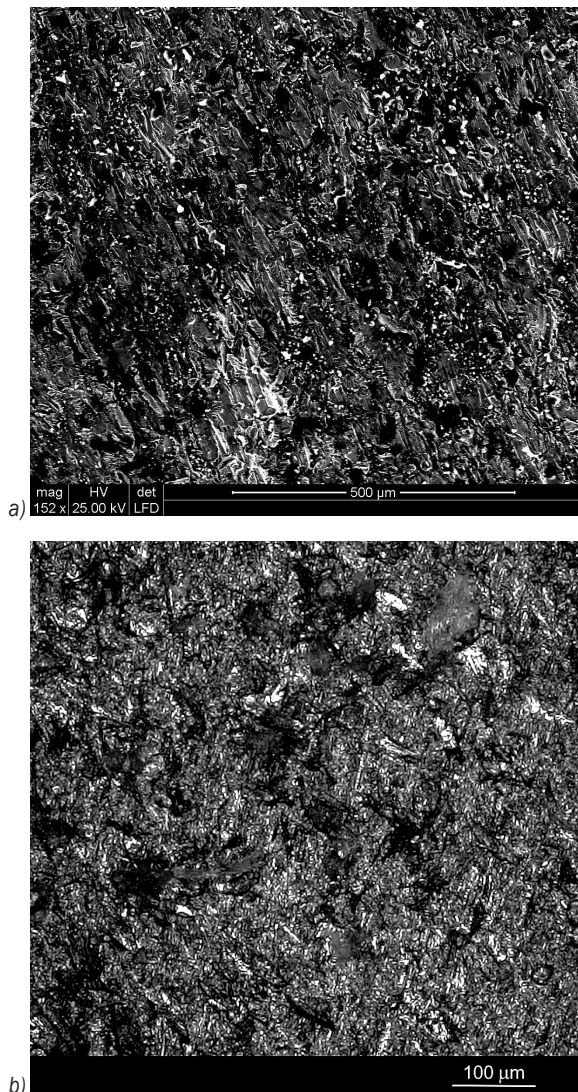


Fig. 6. Cut kerf surface at optimal conditions: a) SEM view, and b) optical microscope view

4 CONCLUSIONS

The conducted research confirmed the equity of applying the method in multi-criteria optimization

of the 18CrNiMo7-6 steel cutting process by AWJ. The CODAS method transforms the multiple characteristics of cutting process into the individual H_i coefficient, which significantly simplifies the computation. The CODAS method determines the ranks of evident from computational results by optimal machining variable combination.

Optimal condition from cutting depth and roughness surface was achieved at following control parameters:

- abrasive feed rate: 350 g/min,
- pressure: 400 MPa,
- traverse speed: 50 mm/min.

Future studies will be conducted on the impact of other control parameters.

5 NOMENCLATURES

X	decision-making matrix,
AFR	abrasive flow rate, [g/min]
p	pressure, [MPa]
Vp	traverse speed, [mm/min]
hc	depth of cut, [mm]
N_b	set of benefit criteria,
N_c	set of cost (non-beneficial) criteria,
n_{ij}	normalized decision matrix,
ns	negative solution,
Sku	surface roughness factor (curtosis), [μm]
R_a	relative assessment matrix value,
r_{ij}	weighted normalized performance value,
Ei	Euclidean distances of alternatives,
Ti	taxicab distances of alternatives,
H_i	assessment score factor,
ψ	threshold function.

6 REFERENCES

- [1] Radomska-Zalas, A. (2022). The AHP method in the optimization of the epoxidation of allylic alcohols. *Procedia Computer Science*, vol. 207, p. 456-464, DOI:10.1016/j.procs.2022.09.100.
- [2] Radomska-Zalas, A., Fajdek-Bieda, A. (2021). IT support for the optimization of the epoxidation of unsaturated compounds on the example of the TOPSIS method. I. Czarnowski; R. J. Howlett; L. C. Jain (Eds.). *Intelligent Decision Technologies* (vol. 238), Springer Singapore, p. 297-307, DOI:10.1007/978-981-16-2765-1_25.
- [3] Sabotin, I., Tristo, G., Valentinčič, J. (2020). Technical model of micro electrical discharge machining (EDM) milling suitable for bottom grooved micromixer design optimization. *Micromachines*, vol. 11, no. 6, art. ID 594, DOI:10.3390/mi11060594.
- [4] Perec, A., Radomska-Zalas, A., Fajdek-Bieda, A., Pude, F. (2022). Process optimization by applying the response

- surface methodology (RSM) to the abrasive suspension water jet cutting of phenolic composites. *Facta Universitatis, Series: Mechanical Engineering*, Online first: <http://casopisi.junis.ni.ac.rs/index.php/FUMechEng/article/view/10193>, DOI:10.22190/FUME211123010P.
- [5] Pellegrini, G., Ravasio, C. (2020). A sustainability index for the micro-EDM drilling process. *Journal of Cleaner Production*, vol. 247, art. ID 119136, DOI:10.1016/j.jclepro.2019.119136.
- [6] Pahuja, R., Ramulu, M. (2019). Abrasive water jet machining of Titanium (Ti6Al4V)-CFRP stacks - A semi-analytical modeling approach in the prediction of kerf geometry. *Journal of Manufacturing Processes*, vol. 39, p. 327-337, DOI:10.1016/j.jmapro.2019.01.041.
- [7] Lehocká, D., Klichová, D., Foldyna, J., Hloch, S., Hvizdoš, P., Fides, M., Botko, F. (2017). Comparison of the influence of acoustically enhanced pulsating water jet on selected surface integrity characteristics of CW004A copper and CW614N brass. *Measurement*, vol. 110, p. 230-238, DOI:10.1016/j.measurement.2017.07.005.
- [8] Hlavacek, P., Zlamal, T., Sitek, L. (2018). Abrasive water jet drilling of cooling holes in aeroengines: preliminary experimental study. *MM Science Journal*, vol. 2018, no. 01, p. 2218-2222, DOI:10.17973/MMSJ.2018_03_201771.
- [9] Hloch, S., Souček, K., Svobodová, J., Hromasová, M., Müller, M. (2022). Subsurface microtunneling in ductile material caused by multiple droplet impingement at subsonic speeds. *Wear*, vol. 490-491, art. ID 204176, DOI:10.1016/j.wear.2021.204176.
- [10] Valíček, J., Drzik, M., Hloch, S., Ohlidal, M., Miloslav, L., Gombar, M., Radvanska, A., Hlavacek, P., Palenikova, K. (2007). Experimental analysis of irregularities of metallic surfaces generated by abrasive waterjet. *International Journal of Machine Tools & Manufacture*, vol. 47, no. 11, p. 1786-1790, DOI:10.1016/j.ijmactools.2007.01.004.
- [11] Nag, A., Hloch, S., Dixit, A.R.; Pude, F. (2020). Utilization of ultrasonically forced pulsating water jet decaying for bone cement removal. *The International Journal of Advanced Manufacturing Technology*, vol. 110, no. 3-4, p. 829-840, DOI:10.1007/s00170-020-05892-9.
- [12] Hreha, P., Hloch, S., Magurova, D., Valicek, J., Kozak, D., Harnicarova, M., Rakin, M. (2010). Water jet technology used in medicine. *Tehnickí Vjesnik*, vol. 17, no. 2, p. 237-240.
- [13] Hloch, S., Foldyna, J., Sitek, L., Zeleňák, M., Hlaváček, P., Hvizdos, P., Kl'oc, J., Monka, P., Monkova, K., Kozak, D., Magurová, D. (2013). Disintegration of bone cement by continuous and pulsating water jet. *Tehnickí Vjesnik*, vol. 20, p. 593-598.
- [14] Stolárik, G., Nag, A., Petrů, J., Svobodová, J., Hloch, S. (2021). Ultrasonic pulsating water jet peening: Influence of pressure and pattern strategy. *Materials*, vol. 14, no. 20, art. ID 6019, DOI:10.3390/ma14206019.
- [15] Hloch, S., Srivastava, M., Nag, A., Müller, M., Hromasová, M., Svobodová, J., Kruml, T., Chlupová, A. (2020). Effect of pressure of pulsating water jet moving along stair trajectory on erosion depth, surface morphology and microhardness. *Wear*, vol. 452-453, art. ID 203278, DOI:10.1016/j.wear.2020.203278.
- [16] Perec, A. (2016). Abrasive suspension water jet cutting optimization using orthogonal array design. *Procedia Engineering*, vol. 149, p. 366-373, DOI:10.1016/j.proeng.2016.06.680.
- [17] Perec, A., Radomska-Zalas, A. (2022). WASPAS optimization in advanced manufacturing. *Procedia Computer Science*, vol. 207, p. 1193-1200, DOI:10.1016/j.procs.2022.09.175.
- [18] Radomska-Zalas, A., Perec, A., Fajdek-Bieda, A. (2019). IT support for optimisation of abrasive water cutting process using the TOPSIS method. *IOP Conference Series: Materials Science and Engineering*, vol. 710, art. ID 012008, DOI:10.1088/1757-899X/710/1/012008.
- [19] Perec, A. (2021). Research into the disintegration of abrasive materials in the abrasive water jet machining process. *Materials*, vol. 14, no. 14, art. ID 3940, DOI:10.3390/ma14143940.
- [20] Perec, A. (2017). Disintegration and recycling possibility of selected abrasives for water jet cutting. *DYNA*, vol. 84, no. 203, p. 249-256, DOI:10.15446/dyna.v84n203.62592.
- [21] Hlavacova, I., Sadilek, M., Vanova, P., Szumilo, S., Tyc, M. (2020). Influence of steel structure on machinability by abrasive water jet. *Materials*, vol. 13, no. 19, art. ID 4424, DOI:10.3390/ma13194424.
- [22] Perec, A., Musial, W. (2021). Multiple criteria optimization of abrasive water jet cutting using entropy-VIKOR approach. S. Hloch, D. Klichová, F. Pude, G. M. Krolczyk, S. Chattopadhyaya (Eds.). *Advances in Manufacturing Engineering and Materials II*, Springer International Publishing, Cham, p. 50-62, DOI:10.1007/978-3-030-71956-2_5.
- [23] Perec, A., Radomska-Zalas, A., Fajdek-Bieda, A., Kawecka, E. (2022). Efficiency of tool steel cutting by water jet with recycled abrasive materials. *Materials*, vol. 15, no. 11, art. ID 3978, DOI:10.3390/ma15113978.
- [24] Kumari, A., Acherjee, B. (2022). Selection of non-conventional machining process using CRITIC-CODAS method. *Materials Today: Proceedings*, vol. 56, p. 66-71, DOI:10.1016/j.matpr.2021.12.152.
- [25] Sivalingam, V., Poogavanam, G., Natarajan, Y., Sun, J. (2022). Optimization of atomized spray cutting fluid eco-friendly turning of Inconel 718 alloy using ARAS and CODAS methods. *The International Journal of Advanced Manufacturing Technology*, vol. 120, no. 7-8, p. 4551-4564, DOI:10.1007/s00170-022-09047-w.
- [26] Al-Tamimi, A.A., Sanjay, C. (2023). Intelligent systems to optimize and predict machining performance of Inconel 825 alloy. *Metals*, vol. 13, no. 2, art. ID 375, DOI:10.3390/met13020375.
- [27] Malaga, A.K., Agrawal, R., Wankhede, V.A. (2022). Material selection for metal additive manufacturing process. *Materials Today: Proceedings*, vol. 66, p. 1744-1749, DOI:10.1016/j.matpr.2022.05.272.
- [28] Sivalingam, V., Ganesh Kumar, P., Prabakaran, R., Sun, J., Velraj, R., Kim, S.C. (2022). An automotive radiator with multi-walled carbon-based nanofluids: A study on heat transfer optimization using MCDM techniques. *Case Studies in Thermal Engineering*, vol. 29, art. ID 101724, DOI:10.1016/j.csite.2021.101724.

- [29] Abas, M., Alkahtani, M., Khalid, Q. S., Hussain, G., Abidi, M. H., Buhl, J. (2022). Parametric study and optimization of end-milling operation of AISI 1522H steel using definitive screening design and multi-criteria decision-making approach. *Materials*, vol. 15, no. 12, art. ID 4086, DOI:10.3390/ma15124086.
- [30] Badi, I., Shetwan, A.G., Abdulshahed, A.M. (2017). Supplier selection using combinative distance-based assessment (CODAS) method for multi-criteria decision-making. *SSRN Electronic Journal*, p. 397-407, DOI:10.2139/ssrn.3177276.
- [31] Karaşan, A., Boltürk, E., Kahraman, C. (2019). A novel neutrosophic CODAS method: Selection among wind energy plant locations. *Journal of Intelligent & Fuzzy Systems*, vol. 36, no. 2, p. 1491-1504, DOI:10.3233/JIFS-181255.
- [32] Ijadi Maghsoodi, A., Ijadi Maghsoodi, A., Poursoltan, P., Antucheviciene, J., Turskis, Z. (2019). Dam construction material selection by implementing the integrated SWARA-CODAS approach with target-based attributes. *Archives of Civil and Mechanical Engineering*, vol. 19, no. 4, p. 1194-1210, DOI:10.1016/j.acme.2019.06.010.
- [33] Roy, J., Das, S., Kar, S., Pamučar, D. (2019). An extension of the CODAS approach using interval-valued intuitionistic fuzzy set for sustainable material selection in construction projects with incomplete weight information. *Symmetry*, vol. 11, no. 3, art. ID 393, DOI:10.3390/sym11030393.
- [34] Krajcarz, D., Spadlo, S. (2016). Influence of the process conditions on the diameter of cylindrical holes produced by abrasive water jet cutting. *METAL 2016: 25th Anniversary International Conference on Metallurgy and Materials*, p. 1462-1467.
- [35] Ovako Steel Navigator (2023). 18CrNiMo7-6, from <https://steelnavigator.ovako.com/steel-grades/18crnimo7-6/>, accessed 2023-03-08.
- [36] Interlloy (2023). 4317 Case Hardening Steel | Interlloy | Engineering Steels + Alloys, Interlloy Engineering Steels and Alloys, from <http://www.interlloy.com.au/our-products/case-hardening-steels/x4317-case-hardening-steel/>, accessed 2023-03-08.
- [37] Surface Roughness Measurement-Parameters | Olympus. (2023), from <https://www.olympus-ims.com/en/metrology/surface-roughness-measurement-portal/parameters/#:~:focus=areal-method>, accessed 2023-07-19.
- [38] Ghorabae, M.K., Zavadskas, E.K., Turskis, Z., Antucheviciene, J. (2016). A new combinative distance-based assessment (CODAS) method for multi-criteria decision-making. *Economic Computation and Economic Cybernetics Studies and Research*, vol. 50, no. 3, p. 25-44.

Fuzzy Logic Approach to Predict Surface Roughness in Powder Mixed Electric Discharge Machining of Titanium Alloy

Dragan Rodić* – Marin Gostimirović – Milenko Sekulić – Borislav Savković – Andjelko Aleksić

University of Novi Sad, Faculty of Technical Sciences, Serbia

This study deals with fuzzy logic based modeling and parametric analysis in powder mixed electrical discharge machining of titanium alloys. The central composition plan was used to design the experiments considering four parameters, namely discharge current, pulse duration, duty cycle as well as graphite powder concentration. All experiments were performed with different parameter combinations and the performance, i.e., surface roughness, was evaluated. The adaptive neuro-fuzzy inference system was used to understand and define the input-output relationship. The experimental results and the model results were compared and it was found that the results accurately predicted the reactions in the erosion of titanium alloys. In addition, the model was verified using data that had not participated in the training of the model, with an error of about 10 %. In addition, a fuzzy plot was used to analyze the influence of input parameters on surface roughness. It was found that the discharge current was the most important influencing parameter. Additional experiments proved the positive effect of graphite powder, which reduced the surface roughness by 27 %.

Keywords: ANFIS, discharge current, pulse duration, duty cycle, graphite powder

Highlights

- Design and development of powder mixed electrical discharge machining to reduce surface roughness.
- Creation of fuzzy model for surface roughness prediction and analysis.
- Verification of the fuzzy model based on a series of new experiments.
- The influence of the input parameters on the surface roughness.

0 INTRODUCTION

Electrical discharge machining (EDM) is an unconventional machining process widely used in the manufacturing industry. It is a material removal process that can be used to machine all electrically conductive materials, regardless of their physical and metallurgical properties [1]. However, the current application of EDM is limited due to its relatively low machining productivity and low surface quality. Possible technological improvements of EDM can be achieved by renewing existing processes. The addition of electrically conductive powder to the dielectric creates a modified material removal process known as powder mixed electrical discharge machining (PMEDM), which significantly affects the performance of the EDM process on difficult-to-machine materials.

Conductive powder added to a liquid dielectric reduces the insulating properties of the dielectric and causes an increase in the gap distance between the tool and the workpiece. An increase in the gap distance means more efficient circulation of the dielectric, i.e. cleaning of the working space between the tool and the workpiece. In this way, EDM becomes more stable, which improves the technological characteristics of the process, such as increasing productivity and reducing surface roughness, and also leads to lower

tool wear [2]. Fig. 1 shows a comparison between the classical EDM (Fig. 1a) and the modified PMEDM (Fig. 1b).

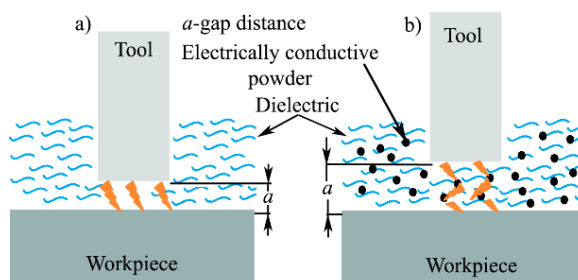


Fig. 1. Comparison of a) classical EDM, and b) modified PMEDM

Various types of electrically conductive powders can be mixed with dielectric, including aluminum, graphite, silicon, copper, silicon carbide and others [3] to [5]. In the study published by Mohri et al. [6], he mixed silicon powder with a grain size of 10 μm to 30 μm with a liquid dielectric. The processing was performed with low discharge currents (0.5 A to 1 A), short pulse duration ($\leq 3 \mu\text{s}$) and negative polarity of the tool. Analysis of the machining process showed a decrease in surface roughness to $Ra \leq 2 \mu\text{m}$. Similarly, Narumiya et al. [7] used aluminum and graphite powders with a grain size of 15 μm and concentrations of 2 g/l to 15 g/l under certain machining conditions.

Again, a decrease in surface roughness to below 2 μm was observed. By adding electrically conductive powder 4 g/l and liquid additive 4 g/l to the dielectric, Ming and Liu [8] positively influenced the technological properties of the process. There was a significant increase in machining productivity, a reduction in relative tool wear and surface roughness even up to $Ra \leq 1 \mu\text{m}$. Wong et al. used powders of different electrical conductivity, such as graphite, silicon, aluminum, crushed glass, silicon carbide, and molybdenum sulfate, and studied their influence on surface roughness [9]. They concluded that the powders: graphite (grain size 40 μm) and silicon (grain size 45 μm) gave the best results in terms of surface roughness. It is interesting to mention the research presented by Kansal et al. [10]. Here, a classification of machining parameters is made: electrical (discharge current and voltage, pulse duration, pause time), non-electrical (type of cleaning of the working area, machining time), powder parameters (type, concentration, grain size) and tool parameters (material and cross section of the tool). Through the analysis of the experiment, it was found that the discharge current, the pulse duration, the pause time and the concentration of the powder in the dielectric have the greatest influence on the surface roughness in PMEDM. Accordingly, from the point of view of surface quality, parameters such as lower discharge current and shorter pulse duration are recommended. What types of powders can be used with liquid dielectric, what particle sizes, at what concentration, and what effect they have on the performance of the PMEDM process is still a question. In order to get an answer as close as possible, researches often resort to modeling the PMEDM process.

Compared to classical EDM, the modeling of PMEDM also takes into account the parameters type, size and concentration of the powder in the dielectric, in addition to the influential input factors already mentioned. Adding another variable parameter, such as powder concentration, significantly complicates the EDM modeling process. The analysis of the change in surface roughness as a function of input parameters in PMEDM with chromium powder was processed by Ojha et al. [11]. The obtained results show that the discharge current and the concentration of the powder in the dielectric have the greatest influence on the surface roughness in carbon steel machining. A similar study, also on the machining of tool steels, was carried out by Batish et al. [12], in which a mathematical model was developed to determine the optimal PMEDM input parameters as a function of the specified objective functions. Through analysis,

he found that discharge current, pulse duration, and powder concentration had the greatest influence on productivity, relative tool wear, and machining accuracy. Increasing the powder concentration in the dielectric improves EDM performance, but only up to a certain limit because a short circuit occurs. The conclusion is that the powder concentration should not be higher than 10 g/l. Using classical mathematical modeling, researchers obtained models based on which they analyzed and predicted the results. However, when exact mathematical information is not available, soft computing techniques are useful. They differ from conventional computing in that they tolerate imprecision, uncertainty, partial truth, approximation, and heuristics.

Recently, soft computing techniques such as fuzzy logic [13], neural networks [14], and evolutionary algorithm [15] have been increasingly used in engineering and science because they provide a simple and understandable path to the final solution. Thanks to its logical mathematical concept, based on natural language and with a high tolerance to inaccurate data, fuzzy logic provides an easy way to concretize an appropriate solution. In addition to the possibility of predicting the results, fuzzy logic also offers the possibility of analyzing the results by means of their 3D diagrams, i.e. a set of all possible solutions. Therefore, various researchers have chosen the fuzzy logic method for modeling the EDM process. Shureka et al. [16] have made an attempt to find the effect of aluminum powder on the EDM of EN-19 alloy steel, using response surface modeling and application of fuzzy gray relational analysis. Kazi et al. [17] investigated a hybrid powder mixing EDM process in which several powder types are mixed. The process parameters considered are discharge current, pulse duration, and powder concentration. They used response surface methodology (RSM) and central composite design (CCD) for design of experiments and fuzzy algorithm for optimization of process parameters. Mala et al. [18] used a linear regression model and an adaptive neuro-fuzzy inference system (ANFIS) to predict outcomes such as production and surface roughness. Comparing these two methods, they concluded that more accurate prediction of outcomes was possible with an ANFIS-based model. Goyal et al. [19] studied the effect of adding nano-graphene powder in the dielectric on the surface roughness of nickel superalloys during EDM. They used a fuzzy logic and ANFIS model and obtained excellent prediction of surface roughness. Muthuramalingam et al. [20] studied the effect of EDM machining parameters on surface quality. They

also used ANFIS to predict and analyze the results. A similar application of an intelligent system was done by Mohanty et al. [21] where they predicted output parameters such as surface roughness. Bhowmick et al. [22] used response surface methodology and fuzzy logic to predict machining performance in PMEDM. The obtained model was found to be efficient for predicting the responses.

From the review of previous literature, it appears that several experimental works have been carried out on the PMEDM of titanium alloys using the ANFIS technique. However, there are very few studies on ANFIS modeling and prediction of surface roughness based on the variation of graphite powder concentration as an input parameter. Therefore, extensive research is needed to investigate the knowledge base of input parameters and their effects on machining performance such as surface roughness. For the above reasons, the main contribution of this research is to find complex relationships between the variable input parameters (discharge current, pulse duration, duty cycle, and graphite powder concentration) and the output performance (surface roughness) of titanium alloy PMEDM. Choosing the right parameters always leads to efficient machining. Since EDM is often used as a finishing process in practice, surface roughness is the most important response. The proposed study provides an answer to the question of which concentration of graphite powder has the greatest influence on surface roughness depending on certain input parameters.

Besides the introduction, the rest of the paper is organized as follows. The second chapter describes the material and methods. Here, the general processing conditions, the method of adding powder to the dielectric, the experimental plan, and the ANFIS technique are described. A special feature in the second chapter is the pilot experiments, based on which the input parameters were systematized and their range was determined. Sections 3 and 4 describes the results, analysis, discussion, and comments on future work. Finally, conclusions are drawn in Section 5.

1 MATERIAL AND METHODS

The experiments in this paper aimed to improve the machining performance of classical EDM. This is done by using methods such as PMEDM. All with the aim of improving machining performance such as surface roughness when machining titanium alloys. The flow chart used in this study to create the fuzzy model is shown in Fig. 2.

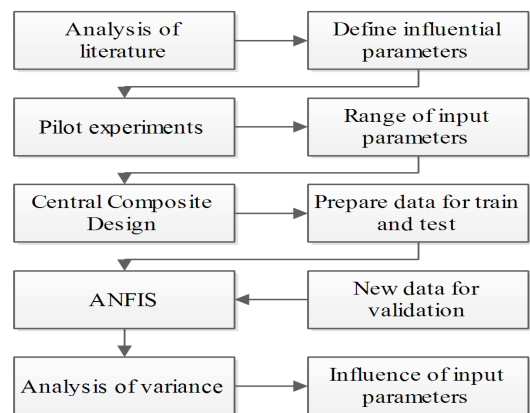


Fig. 2. Flowchart of the research methodology

In order to obtain a well-trained ANFIS model for surface roughness prediction, it was necessary to conduct the research in several steps. Based on the available literature, an analysis was performed and then the initial values of the input parameters were determined. Therefore, it was quite difficult to determine the ranges of input factors, especially the concentration of graphite powder. Due to the incoherence of the data in the literature, pilot experiments were conducted to define the range of input parameters more precisely. Accordingly, the values of the variable input parameters such as discharge current, pulse duration, and graphite powder concentration were determined.

The experiments were then performed according to the CCD. The experimental points are divided into data for training and testing the ANFIS model. The way in which the data is divided is explained in section 3. After the smallest model error was determined, the model was verified with new data. After the verification of the model, the analysis of the influence of the input parameters on the surface roughness follows.

1.1 General Conditions

A die-sinking EDM machine with a solid electrode from Agie Charmille called SP1-U was used for the material processing. The machine is equipped with a direct current (DC) pulse generator with an apparent power of 10 kVA, which generates a maximum discharge current of 50 A.

Ilocut EDM 180 dielectric manufactured by Castrol was used for the experimental studies. Asbury PM19 graphite powder was used for machining titanium alloys by PMEDM. This powder was selected for its high electrical conductivity, which, when mixed with the dielectric, increases the working

gap and washes out the working space. The purity of this graphite powder is 95.5 %, while the grain size is 19 μm (granulation).

The surfactant *Tween 20* $C_{58}H_{114}O_{26}$ is a clear liquid with high density. The rule of the surfactant is to prevent shrinkage or clumping of the graphite powder particles to ensure a homogeneous mixture of powder and dielectric.

The titanium alloy TiAl_6V_4 was selected as a difficult-to-machine material. The selected titanium alloy due to its exceptional characteristics, such as high temperature and corrosion resistance, has found application in the aviation industry, biomedicine and many other branches of technology. A Toyo Tanso TTK50 graphite tool was used for the PMEDM of the titanium alloy. The surface roughness measurements were performed using the MarSurf PS1 instrument from Mahr Metrology. The selected reference gauge length, i.e. the movement of the probe on the measuring surface, is 5.6 mm.

1.2 Powder Mixed Electrical Discharge Machining

For the needs of PMEDM, a tank with elements for fixing and positioning the closed workpiece was designed and manufactured, Fig. 3. In this way, the electroerosive machine is prevented from being contaminated with graphite powder, minimizing costs. The dimensions of the tank are 330 mm \times 330 mm \times 330 mm, with a capacity of 20 liters. With such an adapted system, it is necessary to ensure the correct distribution of the powder as well as the cleaning of the working area.

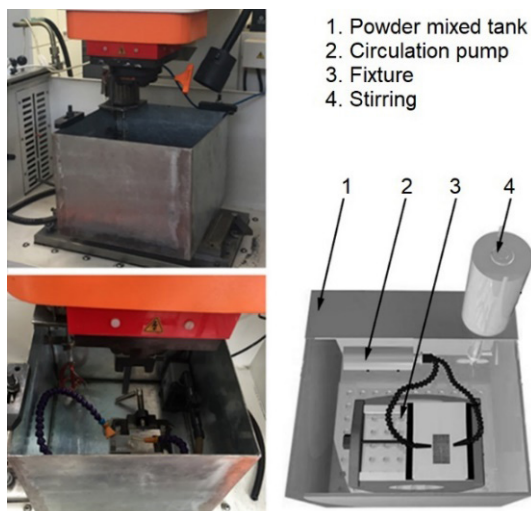


Fig. 3. Powder mixed electrical discharge machining

1.3 Pilot Experiments

Before planning experimental tests, it is necessary to determine the range of variation of appropriate input parameters for machining, as well as other factors whose values are constant during the test. Based on available literature sources and preliminary experimental studies, suitable conditions for PMEDM of TiAl_6V_4 were determined.

The magnitude of the discharge current is limited by the dimensions of the electrode's frontal surface, i.e., the current density. According to the recommendation of the electrode manufacturer Toyo Tanso and literature sources, the maximum current density for graphite TTK50 in rough machining is in the range of 10 A/cm² to 20 A/cm², depending on the type of paired materials [1] and [23]. In order to determine the upper limit of the discharge current, an experiment was performed with a current of 9.5 A. The surface of the workpiece was damaged and of very poor quality. Therefore, in this experimental study, the discharge current in the range of 1.5 A to 7.5 A was used when eroding titanium alloys without mixing graphite powder with the dielectric.

According to studies [23] and [24] the upper limit of pulse duration for machining titanium alloys is 200 μs to 500 μs . Therefore, in order to determine the range of pulse duration, preliminary experimental tests were performed for two discharge current values of 3.2 A and 7.5 A, varying the pulse duration. As can be seen from Fig. 4, the discharge current and pulse duration should be as small as possible to achieve a smaller value of surface roughness.

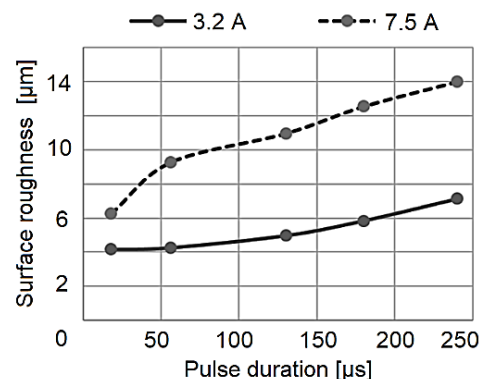


Fig. 4. Influence pulse duration and discharge current on surface roughness

According to the available literature data, a value of the impulse action coefficient higher than 50 % affects the integrity of the treated titanium alloy surface [25] to [27].

In this context, for the electroerosive machining in dielectric with mixed TiAl_6V_4 powder, the impulse action coefficient was varied within the limits of 30 % to 70 % in this study.

It is known that when EDM steel and other metallic materials, the positive polarity of the tool is usually used, but this is not the case when machining titanium alloys. The reasons for this can be found in the results of individual investigations. The authors Klocke et al. [2] conducted a comparative study of the influence of tool polarity on machining productivity when processing steel and titanium alloys. In their experiments, the negative polarity of the tool was used in PMEDM of titanium alloy.

A review of the literature revealed that the concentration of graphite powder usually ranges from 0 g/l to 20 g/l for different paired materials of the tool and the workpiece [12] and [28]. In order to determine the upper limit of graphite powder concentration, experiments with a powder concentration of 20 g/l were conducted in this study. A review of the literature revealed that the graphite powder concentration is usually between 0 g/l and 20 g/l for different paired materials of the tool and the workpiece.

In order to determine the upper limit of graphite powder concentration, experiments were conducted in this study with a powder concentration of 20 g/l. This resulted in damage to the surface of the workpiece, Fig. 5. In this context, for the PMEDM of TiAl_6V_4 in this investigation, the powder concentration was varied in the range of 0 g/l to 15 g/l.

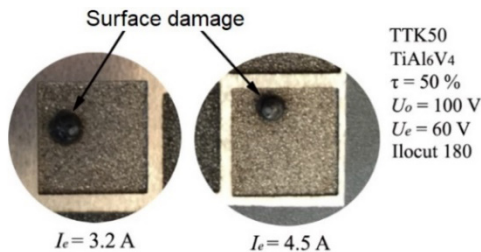


Fig. 5. Surface damage due to high concentration of graphite powder

1.4 Systematized Selected Parameters

The parameters affecting the performance of EDM of titanium alloys can be divided into two groups: electrical pulse parameters and non-electrical process parameters. The systematized conditions for machining titanium alloys are listed in Tables 1 and 2.

The experiments used a dielectric side wash with a flow rate of 20 l/min through a nozzle with

a diameter of 4 mm and another nozzle with a cross section of 2 mm × 8 mm. The tool lift-off time was 2 seconds, and this was done at a distance of 1.5 mm. The erosion time for each test point was 60 minutes.

Table 1. Electric parameters during PMEDM TiAl_6V_4

Electric parameters	Symbol	Value
Discharge current [A]	I_e	1.5 to 7.5
Pulse duration [μs]	t_i	24 to 240
Pause time [μs]	t_o	24 to 240
No load voltage [V]	U_0	100
Discharge voltage [V]	U_e	60
Polarity [-]	Pol	(-)
Duty cycle [%]	τ	30 to 70

Table 2. Non electric parameters during PMEDM TiAl_6V_4

Non electric parameters	Symbol	Value
Flow [l/min]	Q	20
Tool lift [mm]	UP	1.5
Time lift [s]	DN	2
Graphite powder [g/l]	GR	0 to 12
Surfactant [g/l]	SR	10

1.5 Central Composite Plan

There are a large number of design factors to consider as part of the PMEDM process. Among the most important steps is identifying the factors to be included in the study and determining their levels. The surface roughness is affected by several process parameters that can be varied in a variety of ways. The selection of variable and constant input parameters, as shown in Tables 1 and 2, is based on handbook values, literature research, and preliminary tests.

Since the main objective of the research is to minimize the surface roughness, the discharge current, pulse duration, pause time (duty cycle calculation) and graphite concentration were selected as variable parameters. The first two parameters directly affect the discharge energy, with an increase in which the surface roughness also increases. The pause time is expressed by the duty cycle. It is a very important parameter, because with the addition of graphite powder, the time for the generation of the electric discharge changes. The limits for the selected parameters are defined in Section 2.3 and presented in Table 1. Based on the selected parameters and the degree of variation, a spherical central composition plan was constructed, where for the case of four factors $|\alpha| = 2$, Table 3.

1.6 Adaptive Neuro Fuzzy Inference System

ANFIS is the most widely used combination of an artificial neural network and a fuzzy inference system. For a simpler description of the adaptive network with fuzzy logic, a network with two inputs x, y and one output z is considered. The variables x, y are input fuzzy variables, where the first input is determined by n and the second by m membership functions. The rule base contains k -fuzzy IF-THEN Sugeno-type rules:

Rule 1 =

IF x is A_1 and y is B_1 THEN $f_1 = p_1 \cdot x + q_2 \cdot y + r_1$,

Rule k =

IF x is A_k and y is B_k THEN $f_k = p_k \cdot x + q_k \cdot y + r_k$,

where A_1 to A_k and B_1 to B_k are membership functions of the individual inputs x, y of the causal part, while p_k, q_k, r_k are linear parameters of the consequent part. According to Fig. 6 the architecture of the adaptive network consists of five layers, where each layer consists of nodes. There are two types of nodes: square (adaptive parameters) and circular (non-adaptive parameters, fixed).

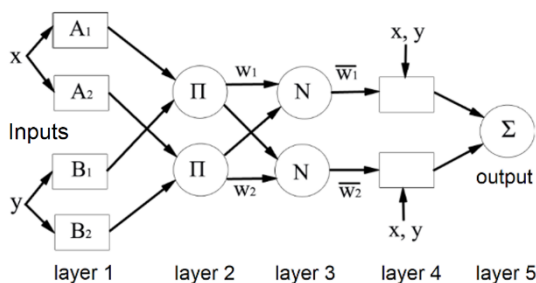


Fig. 6. Adaptive neuro-fuzzy inference system

Layer 1. The adjustable parameters of each node of the first layer contain a function of the following Eq. (1):

$$O_i^1 = \mu_{A_i}(x), \quad O_i^1 = \mu_{B_i}(y), \quad (1)$$

where x and/or y are the inputs to each node, while A_i is the linguistic label of the observed function of the node. The quantity is membership function of A_i and indicates the degree to which the input quantity x satisfies the quantifier A_i . Functions such as trapezoidal, triangular, Gaussian, etc. are also used. Most commonly, is assumed to be a bell-shaped function where the maximum of the function is equal to 1 and the minimum of the function is equal to 0. The bell function is represented by the Eq. (2).

$$O_i^1 = \mu_{A_i}(x) = \frac{1}{1 + \left[\left(\frac{x - c_1}{a_1} \right)^2 \right]^{b_1}}, \quad \text{or}$$

$$O_i^1 = \mu_{A_i}(x) = \exp \left\{ -1 + \left[\left(\frac{x - c_1}{a_1} \right)^2 \right]^{b_1} \right\}, \quad (2)$$

where a_i, b_i, c_i are parameters that define the shape of the function. The number of nodes in this layer is determined by the number of input variables. This layer defines the parameters of the conditional part of the IF-THEN rule.

Layer 2. A layer consisting of fixed nodes. The task of this circular node, denoted Π , is to multiply the input signals and pass the product to the output. The number of circular nodes is equal to the number of rules. An example of multiplication is shown in Eq. (3).

$$O_i^2 = w_i = \mu_{A_i}(x) \cdot \mu_{B_i}(y), \quad i = 1, 2, \quad (3)$$

where w_i output from layer 2.

The third layer also consists of circular layers and is labeled N . The output of this node represents the normalized intensity of execution of each rule, calculated as the ratio of the intensity of the i^{th} rule to the sum of the intensities of all rules, Eq. (4).

$$O_i^3 = \bar{w}_i = \frac{w_i}{\sum_{j=1}^k w_j}, \quad i = 1, 2, \quad (4)$$

where \bar{w}_i is output from layer 3.

Layer 4. Each quadratic node of this plane is represented by an Eq. 5.

$$O_i^4 = \bar{w}_i \cdot f_i = \bar{w}_i (p_i \cdot x + q_i \cdot y + r_i), \quad i = 1, \quad (5)$$

where p_i, q_i, r_i represent adjustable parameters of the consequent part of the rule. Moreover, the number of nodes of this layer is equal to the number of rules.

Layer 5. This plane forms a circular node marked Σ . The task of this node is to summarize all signals coming from the fourth layer. The output of the fifth layer describes the final output of the adaptive network and is expressed by Eq. (6).

$$O_i^5 = f_i(x, y) = \sum_i \bar{w}_i \cdot f_i = \bar{w}_i \cdot f_1 + \bar{w}_i \cdot f_2 = \frac{\sum_i w_i \cdot f_i}{\sum_i w_i}. \quad (6)$$

2 RESULTS

To obtain an appropriate intelligent model of the output performance of the PMEDM process for titanium alloys, an adaptive neuro fuzzy system was used. In the ANFIS model, the membership function parameters are automatically adjusted using an adaptive network based on a set of input/output data. Based on the central composition diagram – CCD, experimental data were used to build the ANFIS model. The central experimental points (25 points to 30 points, total 6 points) were taken as an average. Accordingly, a total of 25 experimental points were used to build the ANFIS model.

Table 3. Central composite plan

No.	Factor				R_a [μm]	
	I_e [A]	t_i [μs]	τ [%]	GR [g/l]	Exp.	ANFIS
1.	3.2	75	40	3	3.81	3.81
2.	6	75	40	3	8.15	8.15
3.	3.2	180	40	3	4.16	4.16
4.	6	180	40	3	11.78	11.78
5.	3.2	75	60	3	3.95	3.95
6.	6	75	60	3	8.52	8.52
7.	3.2	180	60	3	4.25	4.25
8.	6	180	60	3	11.95	11.95
9.	3.2	75	40	9	3.98	3.98
10.	6	75	40	9	7.81	7.81
11.	3.2	180	40	9	4.01	4.01
12.	6	180	40	9	11.65	11.65
13.	3.2	75	60	9	4.12	4.12
14.	6	75	60	9	7.85	7.85
15.	3.2	180	60	9	4.23	4.23
16.	6	180	60	9	8.63	8.63
17.	1.5	130	50	6	1.95	1.95
18.	7.5	130	50	6	12.56	12.56
19.	4.5	24	50	6	5.25	5.25
20.	4.5	240	50	6	7.32	7.32
21.	4.5	130	30	6	6.52	6.52
22.	4.5	130	70	6	6.85	6.85
23.	4.5	130	50	0	8.52	8.52
24.	4.5	130	50	12	6.25	6.25
25.	4.5	130	50	6	7.01	6.23
26.	4.5	130	50	6	6.85	6.23
27.	4.5	130	50	6	5.96	6.23
28.	4.5	130	50	6	6.23	6.23
29.	4.5	130	50	6	6.42	6.23
30.	4.5	130	50	6	6.59	6.23
Average error [%]					1.11	

A very important step is to determine the number of input and output data. According to the

recommendations for the successful creation of ANFIS models, 70 % to 80% of the total data is used for training the network, while 10 % to 15 % is used for testing and 10 % to 15 % for verification [29] and [30]. Therefore, the experimental data generated in this study are divided into three groups: 22 data for training, 3 data for testing, and 3 data for validating the ANFIS model.

The next step in modeling the ANFIS model is to create a fuzzy inference system in which the number and type of membership functions are defined for each input variable: discharge current, pulse duration, duty cycle and graphite powder concentration.

Three bell-type membership functions were selected for each input variable in the construction of a model to determine the arithmetic mean surface roughness. For model, the number of membership functions of the input variables is defined to be three, so the defined number of rules for model is $3^4 = 81$.

After the generation of the fuzzy inference system, the training process follows using an adaptive network. A hybrid optimization method was chosen in which after 100 epochs the shape of the membership functions changes compared to the initial state until the mean squared error (*MSE*) is reduced to a minimum.

The *MSE* represents the first type of error that is analyzed during model development. This error is defined by Eq. (7).

$$MSE = \sqrt{\frac{1}{n} \sum_{i=1}^n (EV_i - PV_i)^2}. \tag{7}$$

According to the previous equation, *n* represents the number of the measured points, *EV* is the experimental data and *PV* is the predicted data. The mean square error (*MSE*) value of $2.293 \cdot 10^{-5}$ was achieved. Since the obtained training error values are satisfactory, we proceed to testing the obtained model. The mean square error obtained when testing the model to determine *R_a* was 0.4509.

The described approach to ANFIS system modeling implies an independent choice of the number of membership functions associated with each input and the number of epochs to train the fuzzy system. These model properties are determined based on the intuition and experience of the model builder.

Before defining the final ANFIS model to determine the performance of the EDM process, models with different types of membership functions were tested. Models with a bell-shaped membership function at the inputs showed the best results. The number of membership functions of each input had the greatest impact on the accuracy of all

models. Acceptable errors were achieved with three membership functions per input. As the number of membership functions increases beyond three, the accuracy of the model increases with an exponential increase in training time. The number of model training epochs is initially set to 500. It is noticeable that after 150 epochs the mean squared error of the model does not change. Increasing the number of epochs further will produce negligible or no effects. These facts are also confirmed in the literature [31].

Besides MSE, the quantitative possibility of prediction is evaluated in terms of the percentage deviation between the obtained and expected values for R_a , in other words, via the mean absolute error MAE, Eq. (8).

$$MAE = \frac{1}{n} \sum_{i=1}^n |EV_i - PV_i| \cdot 100. \quad (8)$$

Based on the calculation of the above error for each point of the experiment, the average error of the observed model was calculated. From Table 3, it can be concluded that the ANFIS model has a satisfactory average error, that is, it has a good ability to predict the results.

For the statistical analysis of the obtained model, in addition to MSE and MAE, the comparison of experimental and model values via a linear fit can be considered. Assuming one-to-one or 100 % accuracy, the predictive ability of the model is evaluated by the coefficient of determination (R^2). The one-to-one plot of the actual and predicted values assumed by the ANFIS model for the main surface roughness was shown in Fig. 7.

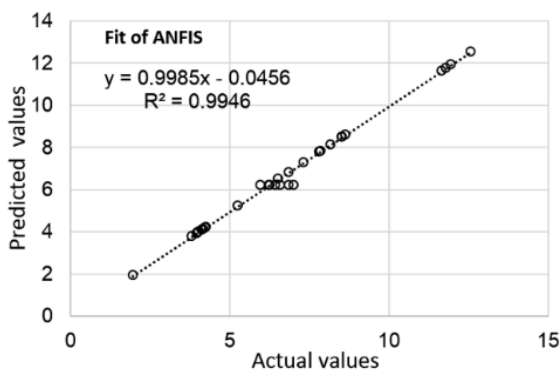


Fig. 7. One-to-one diagram actual and predicted values of surface roughness

The linear fit line, equation and R^2 are also shown in this figure. Willmott defined an index of agreement (R^2) used to measure the degree of linearity of two

variables. If it is 0, it means that there is no correlation, and if it is 1, the correlation is excellent.

Finally, the Bland-Altman method was used as the third statistical element to compare the model results. At Fig. 8, the number of trials are presented on horizontal axis while difference between actual and predicted values represented on vertical axis. The variation between actual and model values of surface roughness is within +0.64 to -0.52 relative to the media line. It can be concluded that the results of the Bland-Altman method agree well with the MAE and MSE error values.

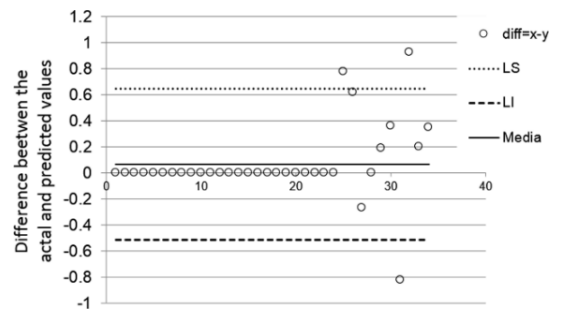


Fig. 8. Bland-Altman plot for ANFIS model of surface roughness

The mentioned methods are used for statistical evaluation of the model during its creation. However, to establish how the model behaves in real systems, it is necessary to perform validation with unknown data. The accuracy of the obtained model was verified by four other experiments that were not involved in the model generation. The presentation of the results of the confirmation test to verify the accuracy of the obtained model is given in Table 4. Based on MAE, the prediction error of the model in the real system is about 10 %.

Table 4. Verification data

No.	Factor				Ra [μm]	
	I_e [A]	t_i [μs]	τ [%]	GR [g/l]	Exp.	ANFIS
1.	3.2	130	50	0	4.97	5.79
2.	3.2	180	50	0	5.84	4.91
3.	3.2	180	30	6	4.45	4.25
4.	6	32	70	6	7.12	6.77
Average error [%]					10.46	

3 DISCUSSION

An intelligent model of the observed output of PMEDM titanium alloy was built using the ANFIS based on the CCD plan. The prediction accuracy of

the model is first tested using three data sets: training, test and verification data. According to the literature, the ratio of these data is approximately 70/15/15, i.e., out of 100 % of the total data, 70 % is used for training and 15 % is used for testing and verification of the model [32]. The error of the model after the training and testing data was 1.11 %, which was expected since the model was trained with these data. However, in the verification experiments, the average error of the obtained model is 10.46 %. According to previous studies, the model is considered predictive when the average error is about 10 % [33] and [34]. In order to increase the reliability of the obtained models, a larger number of data must be used to build the model.

In addition to predicting the results, the obtained ANFIS model can also be used for analysis through 3D diagrams. Fig. 9 shows the dependence of surface roughness on discharge current and pulse duration.

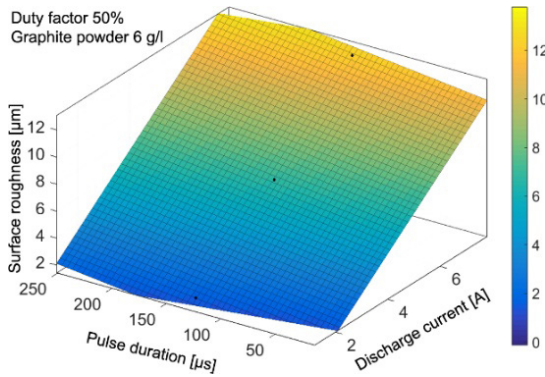


Fig. 9. Effect of discharge current and pulse duration on surface roughness

It can be clearly seen that the surface roughness increases with the increase of the discharge current. This is explained by the fact that the current is directly related to the discharge energy. The higher the discharge energy in the machining zone, the more heat is generated, which causes a greater effect of vaporisation and melting of the workpiece material. In other words, the craters on the surface of the workpiece are larger. These results have also been confirmed in other studies on PMEDM of titanium alloys [35]. Therefore, the pulse duration is also related to the discharge energy. However, Fig. 7 shows a much lower dependence than that of the discharge current. This can be explained by the fact that the pulse duration was limited to a maximum of 250 µs at the beginning of the design of the experiment and therefore did not show any major effects.

Besides to the discharge current, Fig. 10 also shows the influence of the graphite powder

concentration on the surface roughness, based on ANFIS model.

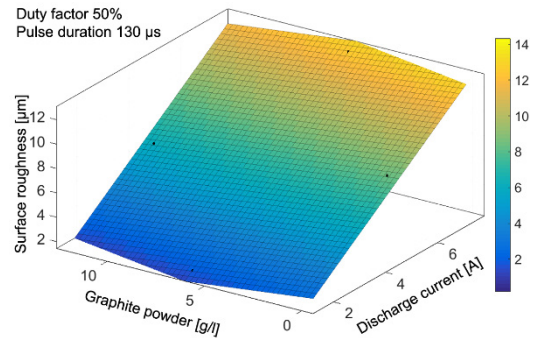


Fig. 10. Effect of discharge current and concentration graphite powder on surface roughness

The addition of graphite powder up to a certain limit has a positive effect on the quality of the surface. It can be seen that above 6 g/l, this positive influence decrease at a discharge current of 1.5 A. Similar conclusions that the concentration increases depending on the processing conditions up to a certain limit have also been drawn by other researchers [12] and [36].

When processing titanium alloys, it is recommended to keep the duty cycle at 50 %. The reason for this is to allow sufficient time for flushing the machining zone. A significant influence of the duty cycle can be expected for values of the pulse duration higher than 200 µs, since a higher discharge energy occurs. A higher discharge energy has a detrimental effect on the surface integrity of the machined titanium alloy if the pause time is too short (calculated in $\tau > 90$ %), which is reflected in [37] and [38].

In order to examine the influence of input factors on surface roughness, the main effects diagram was applied. Therefore, the greatest impact of discharge current is clearly seen, followed by graphite powder concentration, pulse duration and duty factor, Fig. 11.

Table 5. Additional tests

No.	Factor				Exp.
	I_e [A]	t_i [µs]	τ [%]	GR [g/l]	
1.	4.5	50	50	0	8.52
2.	4.5	50	50	6	7.01
3.	4.5	50	50	12	6.25

To more accurately determine the effects of adding graphite powder, additional tests were performed under the conditions listed in Table 5. An

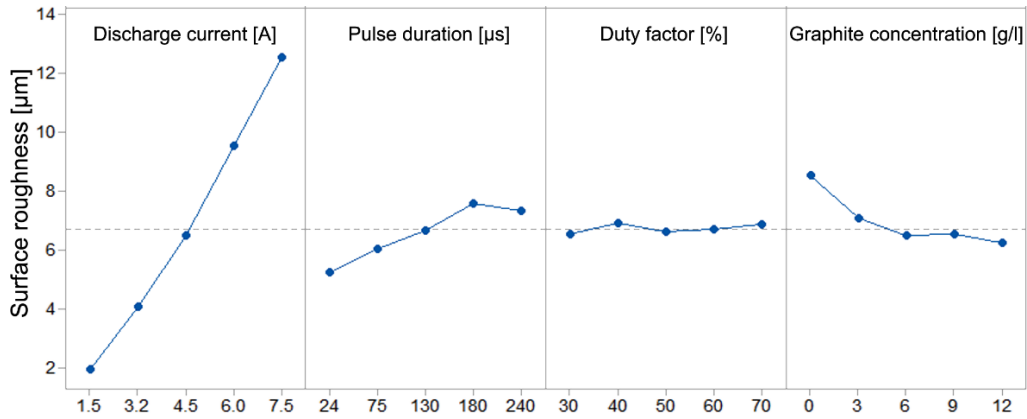


Fig. 11. Main effect plot for surface roughness

example was taken for the discharge current of 4.5 A, as this showed the greatest effect of the addition of graphite powder.

Fig. 12 clearly shows the positive effects of the addition of graphite on the surface quality. No significant decrease in the surface roughness was observed for the other values of the discharge current.

The analysis of the results proved that the process of electric discharge machining in the dielectric with mixed powder achieves more favorable output performance compared to the classical EDM of titanium alloys. The influence of graphite powder concentration was most pronounced at a discharge current of 4.5 A, where the percentage reduction in surface roughness was about 27 %.

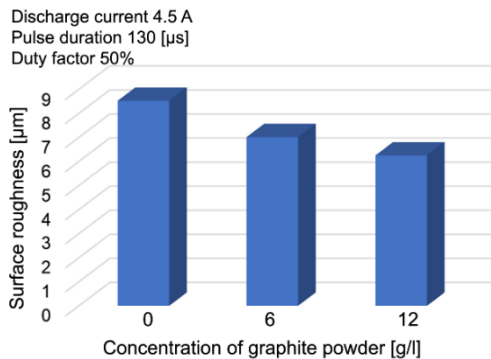


Fig. 12. Influence concentration of graphite powder on surface roughness

Through the research of this paper, some questions of new scientific knowledge were raised, which are given as directions for further development. The first is an investigation of the PMEDM process for titanium alloys considering a larger number and wider intervals of input factors, as well as investigations for different erosion depths. And secondly, the influence

of graphite powder granulation can be one of the input factors that could affect the output performance of EDM of advanced engineering materials.

In addition to granulation, the grain shape of graphite powder may also be an important factor. Since the cross-section of the tool has a great influence on the machining quality, it is necessary to investigate up to which cross-section the use of the PMEDM method is reasonable from the point of view of efficient washing of the machining zone.

Improvement of mathematical modeling by applying new or improved methods, e.g. integration of fuzzy logic and genetic algorithms, neural networks and regression analysis, etc. Additional analysis of the efficiency of experimental designs used to build a classical or intelligent model. For example, the application of the central composition or Box-Behnken plan for training the intelligent model.

4 CONCLUSIONS

This paper presents the results of an experimental investigation carried out with the aim of modeling the process PMEDM of titanium alloy. Preliminary experiments were first carried out in order to determine more precisely the limits of the input parameters. Based on the input parameters of discharge current, pulse duration, duty cycle, and graphite powder concentration, experiments were conducted according to the central composition plan. Then, the modeling of the surface roughness was started using the ANFIS. Based on statistical analysis results show that the MSE is $2.293 \cdot 10^{-5}$ for the training data and 0.4509 for the test data. MAE was also used to evaluate the model, the percentage error of the model for the training and test data was 1.11

%. In addition, the statistical analysis of the model was performed using the coefficient of determination, which is 0.9946. The Bland-Altman method also has good agreement with the error values MAE and MSE. As a final check, the accuracy of the model was verified using four additional experiments that were not involved in model generation and for which MAE was approximately 10 %. It was concluded that the discharge current had the greatest influence on the surface roughness. The powder concentration showed the greatest influence at a discharge current of 4.5 A, at which the surface roughness decreased by 27 %. Future research would include a wider range of input factors as well as other powder types with different grains, shapes, etc. In particular, it is necessary to analyze which experimental design is most suitable for training intelligent models, the amount of data and the like.

5 NOMENCLATURES

I_e	discharge current, [A]
ti	pulse duration, [μ s]
τ	duty cycle, [%]
GR	graphite powder concentration, [g/l]
MSE	mean squared error
MAE	mean absolute error, [%]
R^2	coefficient of determination.

6 ACKNOWLEDGEMENTS

This paper has been supported by the Provincial Secretariat for Higher Education and Scientific Research through the project no. 142-451-1772/2022-01/01: "Research on the innovative process of electrical discharge machining of titanium alloy".

7 REFERENCES

- [1] Gostimirovic, M., Kovac, P., Sekulic, M., Skoric, B. (2012). Influence of discharge energy on machining characteristics in EDM. *Journal of Mechanical Science and Technology*, vol. 26, p. 173-179, DOI:10.1007/s12206-011-0922-x.
- [2] Klocke, F., Lung, D., Antonoglou, G., Thomaidis, D. (2004). The effects of powder suspended dielectrics on the thermal influenced zone by electrodischarge machining with small discharge energies. *Journal of Materials Processing Technology*, vol. 149, no. 1-3, p. 191-197, DOI:10.1016/j.jmatprotec.2003.10.036.
- [3] Patel, S., Thesiya, D., Rajurkar, A. (2018). Aluminium powder mixed rotary electric discharge machining (PMEDM) on Inconel 718. *Australian Journal of Mechanical Engineering*, vol. 16, no. 1, p. 21-30, DOI:10.1080/14484846.2017.1294230.
- [4] Luzia, C.A.O., Laurindo, C.A.H., Soares, P.C., Torres, R.D., Mendes, L.A., Amorim, F.L. (2019). Recast layer mechanical properties of tool steel after electrical discharge machining with silicon powder in the dielectric. *The International Journal of Advanced Manufacturing Technology*, vol. 103, p. 15-28, DOI:10.1007/s00170-019-03549-w.
- [5] Unses, E., Cogun, C. (2015). Improvement of electric discharge machining (EDM) performance of ti-6al-4v alloy with added graphite powder to dielectric. *Strojniški vestnik - Journal of Mechanical Engineering*, vol. 61, no. 6, p. 409-418, DOI:10.5545/sv-jme.2015.2460.
- [6] Mohri, N., Tsukamoto, J., Fujino, M. (1988). Surface modification by EDM - an innovation in edm with semi-conductive electrodes. *Proceedings of Winter Annual Meeting ASME*, vol. 34, p. 21-30.
- [7] Narumiya, H., Mohri, N., Saito, N., Otake, H., Tsnekawa, Y., Takawashi, T., Kobayashi, K. (1989). EDM by powder suspended working fluid. *Proceedings of 9th ISEM*, p. 5-8.
- [8] Ming, Q.Y., Liu, Y.H. (1995). Powder-suspension dielectric fluid for EDM. *Journal of Materials Processing Technology*, vol. 52, no. 1, p. 44-54, DOI:10.1016/0924-0136(94)01442-4.
- [9] Wong, Y.S., Lim, L.C., Rahuman, I., Tee, W.M. (1998). Near-mirror-finish phenomenon in edm using powder-mixed dielectric. *Journal of Materials Processing Technology*, vol. 79, no. 1-3, p. 30-40, DOI:10.1016/S0924-0136(97)00450-0.
- [10] Kansal, H.K., Singh, S., Kumar, P. (2005). Parametric optimization of powder mixed electrical discharge machining by response surface methodology. *Journal of Materials Processing Technology*, vol. 169, no. 3, p. 427-436, DOI:10.1016/j.jmatprotec.2005.03.028.
- [11] Ojha, K., Garg, R.K., Singh, K.K. (2013). Effect of chromium powder suspended dielectric on surface roughness in PMEDM process. *Tribology - Materials, Surfaces & Interfaces*, vol. 5, no. 4, p. 165-171, DOI:10.1179/1751584X11Y.0000000021.
- [12] Batish, A., Bhattacharya, A., Kumar, N. (2014). Powder mixed dielectric: An approach for improved process performance in EDM. *Particulate Science and Technology*, vol. 33, no. 2, p. 150-158, DOI:10.1080/02726351.2014.947659.
- [13] Rodic, D., Gostimirovic, M., Madic, M., Sekulic, M., Aleksic, A. (2020). Fuzzy model-based optimal energy control during the electrical discharge machining. *Neural Computing and Applications*, vol. 32, p. 17011-17026, DOI:10.1007/s00521-020-04909-4.
- [14] Okewu, E., Adewole, P., Misra, S., Maskeliunas, R., Damasevicius, R. (2021). Artificial neural networks for educational data mining in higher education: A systematic literature review. *Applied Artificial Intelligence*, vol. 35, no. 13, p. 983-1021, DOI:10.1080/08839514.2021.1922847.
- [15] Madić, M., Gostimirović, M., Rodić, D., Radovanović, M., Coteață, M. (2022). Mathematical modelling of the CO2 laser cutting process using genetic programming. *Facta Universitatis, Series: Mechanical Engineering*, vol. 20, no. 3, p. 665-676, DOI:10.22190/FUME210810003M.
- [16] Surekha, B., Sree Lakshmi, T., Jena, H., Samal, P. (2021). Response surface modelling and application of fuzzy grey relational analysis to optimise the multi response characteristics of en-19 machined using powder mixed edm.

- Australian Journal of Mechanical Engineering*, vol. 19, no. 1, p. 19-29, DOI:10.1080/14484846.2018.1564527.
- [17] Kazi, F., Waghmare, C., Sohani, M. (2021). Multi-objective optimization of machining parameters in hybrid powder-mixed edm process by response surface methodology and normalized fuzzy logic algorithm. *International Journal on Interactive Design and Manufacturing*, vol. 15, p. 695-706, DOI:10.1007/s12008-021-00788-8.
- [18] Mala, D., Senthilkumar, N., Deepanraj, B., Tamizharasan, T. (2020). *Green Materials and Advanced Manufacturing Technology*, CRC Press, London, p. 75-94, DOI:10.1201/9781003056546.
- [19] Goyal, A., Sharma, D., Bhowmick, A., Pathak, V.K. (2022). Experimental investigation for minimizing circularity and surface roughness under nano graphene mixed dielectric edm exercising fuzzy-anfis approach. *International Journal on Interactive Design and Manufacturing*, vol. 16, no. 3, p. 1135-1154, DOI:10.1007/s12008-021-00826-5.
- [20] Muthuramalingam, T., Saravanakumar, D., Babu, L.G., Huu Phan, N., Pi, V.N. (2020). Experimental investigation of white layer thickness on edm processed silicon steel using ANFIS approach. *Silicon*, vol. 12, p. 1905-1911, DOI:10.1007/s12633-019-00287-2.
- [21] Mohanty, P.P., Mohapatra, D., Mohanty, A., Nayak, S. (2020). ANFIS-based modeling for prediction of surface roughness in powder mixed electric discharge machining. *Computational Intelligence in Data Mining: Proceedings of the International Conference on ICCIDM 2018*, p. 151-159, DOI:10.1007/978-981-13-8676-3_14.
- [22] Bhowmick, S., Mondal, R., Sarkar, S., Biswas, N., De, J., Majumdar, G. (2023). Parametric optimization and prediction of MRR and surface roughness of titanium mixed EDM for Inconel 718 using RSM and fuzzy logic. *CIRP Journal of Manufacturing Science and Technology*, vol. 40, p. 10-28, DOI:10.1016/j.cirpj.2022.11.002.
- [23] Haşçalık, A., Çaydaş, U. (2007). Electrical discharge machining of titanium alloy (Ti-6Al-4V). *Applied Surface Science*, vol. 253, no. 22, p. 9007-9016, DOI:10.1016/j.apsusc.2007.05.031.
- [24] Lin, Y.C., Yan, B.H., Chang, Y.S. (2000). Machining characteristics of titanium alloy (Ti-6Al-4V) using a combination process of EDM with USM. *Journal of Materials Processing Technology*, vol. 104, no. 3, p. 171-177, DOI:10.1016/S0924-0136(00)00539-2.
- [25] Kao, J., Tsao, C., Wang, S., Hsu, C. (2010). Optimization of the EDM parameters on machining Ti-6Al-4V with multiple quality characteristics. *The International Journal of Advanced Manufacturing Technology*, vol. 47, no. 1-4, p. 395-402, DOI:10.1007/s00170-009-2208-3.
- [26] Jabbaripour, B., Sadeghi, M., Faridvand, S., Shabgard, M. (2012). Investigating the effects of EDM parameters on surface integrity, MRR and TWR in machining of Ti-6Al-4V. *Machining Science and Technology*, vol. 16, no. 3, p. 419-444, DOI:10.1080/10910344.2012.698971.
- [27] Klocke, F., Holsten, M., Hensgen, L., Klink, A. (2014). Experimental investigations on sinking-EDM of seal slots in gamma-TiAl. *Procedia CIRP*, vol. 24, p. 92-96, DOI:10.1016/j.procir.2014.07.143.
- [28] Kolli, M., Kumar, A. (2015). Effect of dielectric fluid with surfactant and graphite powder on electrical discharge machining of titanium alloy using Taguchi method. *Engineering Science and Technology, an International Journal*, vol. 18, no. 4, p. 524-535, DOI:10.1016/j.jestch.2015.03.009.
- [29] Sada, S.O., Ikpeseni, S.C. (2021). Evaluation of ANN and ANFIS modeling ability in the prediction of AISI 1050 steel machining performance. *Heliyon*, vol. 7, no. 2, art. ID e06136, DOI:10.1016/j.heliyon.2021.e06136.
- [30] Rodić, D., Sekulić, M., Gostimirović, M., Pucovsky, V., Kramar, D. (2021). Fuzzy logic and sub-clustering approaches to predict main cutting force in high-pressure jet assisted turning. *Journal of Intelligent Manufacturing*, vol. 32, p. 21-36, DOI:10.1007/s10845-020-01555-4.
- [31] Kukolj, D., Levi, E. (2004). Identification of complex systems based on neural and takagi-sugeno fuzzy model. *IEEE Transactions on Systems, Man, and Cybernetics, Part B (Cybernetics)*, vol. 34, no. 1, p. 272-282, DOI:10.1109/TSMCB.2003.811119.
- [32] Castillo, O., Melin, P., Ross, O.M., Cruz, R.S., Pedrycz, W. (2007). *Theoretical Advances and Applications of Fuzzy Logic and Soft Computing*. Springer Science & Business Media, DOI:10.1007/978-3-540-72434-6.
- [33] Nukman, Y., Hassan, M., Harizam, M. (2013). Optimization of prediction error in CO₂ laser cutting process by Taguchi artificial neural network hybrid with genetic algorithm. *Applied Mathematics and Information Science*, vol. 7, no. 1, p. 363-370, DOI:10.12785/amis/070145.
- [34] Thanedar, A., Dongre, G.G., Joshi, S.S. (2019). Analytical modelling of temperature in cylindrical grinding to predict grinding burns. *International Journal of Precision Engineering and Manufacturing*, vol. 20, p. 13-25, DOI:10.1007/s12541-019-00037-9.
- [35] Al-Amin, M., Abdul Rani, A.M., Abdu Aliyu, A.A., Abdul Razak, M.A.H., Hastuty, S., Bryant, M.G. (2020). Powder mixed-edm for potential biomedical applications: A critical review. *Materials and Manufacturing Processes*, vol. 35, no. 16, p. 1789-1811, DOI:10.1080/10426914.2020.1779939.
- [36] Kumar, S., Mandal, A., Dixit, A.R. (2018). Investigation of powder mixed EDM process parameters for machining inconel alloy using response surface methodology. *Materials Today: Proceedings*, vol. 5, no. 2, p. 6183-6188, DOI:10.1016/j.matpr.2017.12.225.
- [37] Fonda, P., Wang, Z., Yamazaki, K., Akutsu, Y. (2008). A fundamental study on Ti-6Al-4V's thermal and electrical properties and their relation to edm productivity. *Journal of Materials Processing Technology*, vol. 202, no. 1-3, p. 583-589, DOI:10.1016/j.jmatprotec.2007.09.060.
- [38] Kumar, M., Datta, S., Kumar, R. (2018). Electro-discharge machining performance of Ti-6Al-4V alloy: Studies on parametric effect and phenomenon of electrode wear. *Arabian Journal for Science and Engineering*, vol., p. 1-16, DOI:10.1007/s13369-018-3632-1.

Mechanical and Microstructural Properties of B_4C/W Reinforced Copper Matrix Composite Using a Friction Stir-Welding Process

Jamuna Elangandhi¹ – Suresh Periyagounder² – Mahalingam Selavaraj³ – Duraisivam Saminatharaja¹

¹The Kavery Engineering College, Department of Mechanical Engineering, India

²Sona College of Technology (Autonomous), Department of Mechatronics Engineering, India

³Sona College of Technology (Autonomous), Department of Mechanical Engineering, India

Copper metal matrix composites (CMC) are broadly employed in various applications in the fields of space, aviation, automobile and electronics industries. The welding of CMC in using conventional methods is very difficult and expensive due to its crystallographic nature. Friction stir welding (FSW) is a more prominent and reliable technique for welding than conventional methods. Therefore, this work is based on work with CMC material, which is prepared with a stir-casting technique. Pure copper (Cu) is reinforced with tungsten (W) and boron carbide (B_4C) particles in different combinations and welded using the FSW process to study the mechanical and micro-structural properties. Multi-objective decision-making methods, such as the technique for order preference by similarity to ideal solution (TOPSIS) and grey relational analysis (GRA) are used to find optimal parameter combination. The experiments are planned according to the L 18 orthogonal array (OA) using the most influential parameters, such as reinforcement the percentage of B_4C , tool rotational speed, welding speed, and axial force. The performance of outcomes is measured based on the responses such as tensile strength, hardness, and impact strength of the weld joint. Based on the results 15 % of B_4C reinforcement, 900 RPM rotational speed, 15 mm/min welding speed and 6 kN axial forces are optimal for better mechanical strength in the welding with TOPSIS and GRA techniques. Additionally, scanning electron microscopic image (SEM) analyses were carried out for better understanding of weldments' microstructure changes.

Keywords: friction stir welding, copper, metal matrix composite, boron carbide

Highlights

- The CMC materials were produced by the friction stir process and contain pure copper (Cu) as matrix and tungsten (W) and boron carbide (B_4C) as reinforcing material in different concentrations.
- Based on experiments with an L-18 orthogonal array (OA), friction stir welding is used to join the CMC cast using parameters such as the percentage of boron carbide reinforcements, tool rotation speed, welding speed and axial force.
- The TOPSIS and GRA techniques are used to determine the optimum combination of parameters.
- The results of the optimisation show that the mechanical strength when welding with the FSW technique increases with the increase of the reinforcement percentage in the copper composite.

0 INTRODUCTION

Extensive research attempt has been conducted regarding the FSW process due to its enormous advantages over traditional welding techniques. The FSW process is the most significant and desirable technique in solid-state welding because it is crack-free, fume-free, has less shrinkage and excellent mechanical strength, etc. Also, FSW finds a broad range of utilization in various sectors, such as construction, marine, aircraft, trains, automobile industries and fuel tanks to obtain quality welding of various parts. Although FSW has many reliable features, due to technological growth, it creates new challenges and problems, such as micro-bores, nonhomogeneous welding surfaces, high heat-affected zones, and less mechanical strength of welding. Nevertheless, the needs for CMC in various applications are increasing day by day in the manufacturing sector. Therefore, in view of improving the welding quality of the composite materials,

various research attempts have been made in the last decade worldwide.

Zamani et al. [1] carried out experiments with the FSW process on aluminium silicon composite work material and optimized the process parameters using an RSM technique. They planned the design of experiment including the transverse speed of tool and suggested that the optimal process parameter combination was 1300 rpm rotational speed and 70 m/min transverse speed. Moreover, the effect of coupling process parameters increases the machining rate significantly. Argesi et al. [2] attempted to join a pure copper and aluminium alloy with SiC particles in the FSW process. They noted that 50 m/min of welding speed and 1000 rpm of rotational speed produced higher tensile strength. The application of SiC particle increases the hardness of welding strength from 160 HV to 320 HV. Sudhagar and Gopal [3] carried out experiments with FSW to fabricate the surface copper composite using Si_3N_4 -reinforced particles in various concentration levels. They

analysed the mechanical and microstructure properties of the weld and also observed that while rotating the tool work piece reached recrystallization temperature, which significantly hinders the micro-hardness of welding. The wear property increases with increased reinforcement particles over the surface copper composite by about 15 %. Thapliyal and Mishra [4] utilized the machine-learning concept to weld the copper work material in the FSW process. The most influential parameters (i.e., welding speed, rotational speed and axial forces) are considered for the experiment. They noted a 94 % improved welding strength using this optimal combination among 119 experiments. Harisha et al. [5] welded the copper and aluminium 6083 using the FSW process to study the optimal process parameter combination. They noted a 70 % improved tensile strength in the parameter combination, such as a rotational speed of 1000 rpm and a welding speed of 50 m/min. Nagesh et al. [6] welded dissimilar materials, such as copper and brass, using the FSW process. They compared the results of FSW, such as tensile, hardness, and the impact strength of dissimilar welding strength with parent metal welding, to explore the detailed nature of welding. Senthil et al. [7] studied the FSW process parameters for aluminium 6063 composites using the response surface methodology (RSM) method. They noted the tensile and yield strength of 167 MPa and 145 MPa, respectively, in the parameter value of 1986 rpm of tool speed. Uniform microstructure properties were also noted with the first optimal parameter combination. Karrar et al. [8] studied the effect of tools' rotational and transverse speeds on dissimilar welding in the FSW process. They welded the aluminium alloy 5083 and copper as work material and observed intricate microstructure in the heat-affected zone. Many intermetallic mixers were seen in the welding zone, which leads to nonhomogeneous micro-hardness. The maximum tensile strength was obtained in 1400 rpm tool speed and 120 mm/min. Kolnes et al. [9] prepared a tool for machining materials such as aluminium, copper, and stainless steel, using TiC, and WC-Co-based ceramic composite in the FSW process. The composites are fabricated with a powder metallurgy technique, which prevents the damage caused by the temperature developed through friction. They noted that 80 % of the TiC-mixed composite electrode produces a fine machining surface in the aluminium work material. Sahu et al. [10] investigated the FSW welding characteristics for magnesium work materials. During the welding process, Zn materials are added to improve the welding quality. Also, the addition of Zn with work

materials forms an MgZn alloy, which produces high wear strength. Jimenez-Mena et al. [11] attempted a dissimilar weld with materials (e.g., aluminium, steel) using the FSW process. They reported that interlayering of the work material increases when increasing the load application on the work material. Also, the presence of Co in steel increased the toughness of weld and propagated cracks in the aluminium plate. Garg and Bhattacharya [12] carried the welding on aluminium alloys such as 6061 and 7075 using the FSW process. They investigated the mechanical characteristics such as tensile, flexural, and fracture strength of the welding. Copper particles are used during the welding as interference, and 2 mm tool pin is employed in the tool shoulder. Souza et al. [13] carried out experiments in Al-Ce-Si-Mg aluminium alloy using the FSW process. The maximum tensile stress (102 MPa) noted with lesser tool rotational speed using a triangular pin profile surface and higher micro-hardness found at higher rotational speed. Shettigar et al. [14] conducted the experiments in rutile-reinforced aluminium alloy 6061 composite using the FSW process. They planned the experiments with tool, welding speed, and various tool profiles shapes in order to obtain better machining quality. They conducted the experiment so that rotational, transverse speed contributed more to welding accuracy and homogeneous reinforcement distribution among the welding surface. Khojastehnezhad and Pourasl [15] welded the aluminium alloy 6061 with copper through FSW process along with copper particles. They noted defect-less welding in the rotational speed of 950 rpm and 50 mm/min welding speed. The observation shows the welded composite at the edge has higher hardness due to the aluminum and copper bonding. Babu et al. [16] investigated the optimal process parameter for aluminium alloy 2219 with the FSW process to obtain a defect-free machining surface. They used a genetic algorithm to find the possible parameter combination and suggested that a 1005 rpm tool speed at 3° tool angle produces excellent machining performance. This optimization technique diminishes the machining cost significantly due the shorter machining time. Peddavarapu et al. [17] prepared the composite using Al-4.5Cu based alloy and reinforced it with TiB₂ particles; this was employed as a work material to study the performance of the FSW process. Normal treaded profile tool was used as tool. They mentioned that uneven material flow, which produces an uneven circumference in the welding. Herbert et al. [18] conducted the experiments in a Cu- and SiC-reinforced aluminium metal matrix

composite, prepared with the stir-casting method and employed in the FSW process to find the optimal welding range of parameters. They used the combined tool profiles (e.g. square and treaded) on the welding and analysed the mechanical and microstructure properties of welding. The hardness of the welding is higher than that of the base metal. Sahu et al. [19] optimized the process parameters of FSW using a fuzzy logic grey analysis method for aluminium and copper welding. They considered the major process parameters, such as tool, welding speed, depth of weld and shape of tool pin. The microstructures of both sides of the metals have fewer defects due to the optimal solution of welding. Ahmadvani et al. [20] carried out the experiments in the FSW process with pure magnesium to find the optimal process parameter combination. They applied the L9 OA and analysed the effect of all parameter combination using the Taguchi method. The hardness of magnesium increases with increased tool speed. Shirazi et al. [21] examined the influences of tool and welding speed on the welding strength of aluminium alloy 5456 via the through FSW process. They reported the findings, which showed that, in addition to the optimum parameter, the remaining combinations have a substantial impact on the welding quality. Kumar et al. [22] experimented with aluminium and copper-based composite on the FSW process under various machining speeds and welding speeds. They noted fewer defects with the welding speed in the range of 70 mm/min to 100 mm/min. They also suggest that the microstructure of welding was significantly influenced by the welding and rotational speeds. Suresh et al. [23] studied the influences of various process parameters on the mechanical and microstructure properties of FSW on aluminium alloy 2219 work material using an RSM technique, which was employed to obtain maximum mechanical strength. They found the optimal process parameter combination of 1627 rpm rotation speed, 083 mm/s welding speed, and 12.2 kN axial force.

The aforementioned sources were used to explore the optimal solution of FSW process parameters for various aspects, such as aluminium-based composites, copper-reinforced work surfaces, varying concentrations reinforcing particles, and the joining of copper to other metals, such as aluminium, stainless steel, titanium, etc. However, experiments with the copper-based composites and their optimization in the literature are rare [24] to [26] and there is no evidence of hybrid CMC in FSW process. The optimization of the process parameters for every machine is done carefully to achieve the right output without

taking major effort. Additionally, optimised values generate high accuracy and reduce unneeded time and cost for quality. In line with that, the TOPSIS and GRA methods are very prominent techniques that are successfully employed in other manufacturing sectors to reveal the optimal solution [27] to [30]. The reinforcement materials, such as W and B₄C particles, provides excellent mechanical strength, thermal stability, and high affinity nature with other materials. Therefore, in this experiment work, material is fabricated with the stir-casting method using commercially available pure copper (Cu) as the matrix and W and B₄C particles as reinforcements in various concentration levels. Based on L18 OA and major influencing parameters, such as the percentage of reinforcements, rotational speed, welding speed, and axial force are used to conduct experiments. The process parameters of FSW are also optimized using simple and prominent techniques, such as TOPSIS and GRA. Furthermore, SEM analyses are carried out on the welding surface to give better understanding of microstructure.

1 EXPERIMENTAL WORK

Commercially available pure copper is considered as the base material, W (30µm), B₄C (50 µm) are employed as reinforcements, and three different CMC materials are fabricated using a stir-casting furnace as shown in Fig. 1. An indigenously created bottom-pouring and electric-stir casting furnace is employed to develop the composite. The Cu rods (25 mm diameter) are cleaned thoroughly and cut into small pieces 10 mm thick. The rods are loaded into a crucible cylinder that is coated with stainless steel and the temperature is maintained at 1200 °C during the melting process. The molten Cu is stirred well using a stir setup that enhances the distribution of reinforcements uniformly throughout the composite. Stainless steel coating is carried out in the stirrer and crucible, which protects the unwanted material amalgamation with CMC. The preset volume of preheated W and B₄C particles is mixed with the molten copper to enhance the wet ability and mechanical strength with copper material. The weight percentages of reinforcement and composition of composite are displayed in Table 1. The well-mixed molten metal is poured into a die (100 mm × 100 mm × 6 mm) to obtain the hybrid composite.

The fabricated CMC plates are employed to study the weldability using the FSW process. The CMC work material in the plate is fastened with a customized vertical milling machine for the FSW

process. The work plates are arranged in a butt joint design, and the tool is fixed with the tool holder against the workpiece, as shown in Fig. 1.

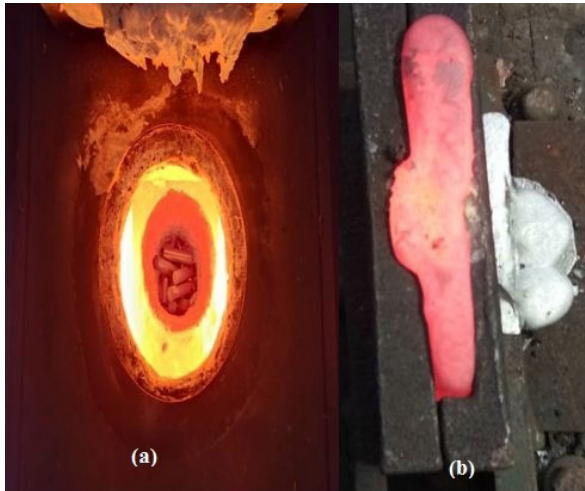


Fig. 1. Friction stir process; a) casting furnace, and b) casting die with molten CMC

The non-consumable tool used in the experiment is made of Tungsten carbide with a shoulder diameter of 18 mm. The tool is designed with a hexagon-shape pin with length and diameter of 6 mm and 4 mm, respectively, for the purpose of stirring the work material, as presented in Fig. 2. The rotating tool is plunged over the work material and allowed to rest for 20 seconds to retain its normal temperature. Afterwards, the tool moves over the work material along its length to the weld. Due to the high friction between the tool and electrode, heat is induced, which makes the work materials soften. The shoulder pin of the tool blends the softened work material by moving it from retreating portion to other side which produces a sound weld joint. In this technique, work materials welded using both heat and mechanical energy but in traditional fusion welding only heat energy is employed to weld the metals. The percentage of reinforcements, tool rotational speed, welding speed and axial forces influence the welding nature of FSW process. Therefore, these parameters are considered to be input controlling factors. L 18 OA is employed to investigate the process parameter over the output responses. The excellence of welding is evaluated by performing different mechanical and micro-structural testing, including for tensile, impact and hardness. The work materials are sliced into the standard dimensions according to ASTM standard through wire cut EDM. Based on the ASTM E8 standard, test samples are fabricated. Two specimens are cut from every welding

specimen and two output responses obtained, which are averaged and considered in order to assess the welding quality. Tables 2 and 3 present the initial parameter levels and design of experiments with output responses respectively, which are considered based on the literature [3]. The micro-hardness of welding is measured using a Vickers hardness testing machine (TE-JINANWDW100, Jinan Test Machine Co. Ltd., China) at different places of welding cross-sections, and average hardness values are considered for evolution. ASTM E23-16a standards are followed to evaluate the impact strength of welding, and a V-notch has been created in welding specimen at right angles to the welding joint.

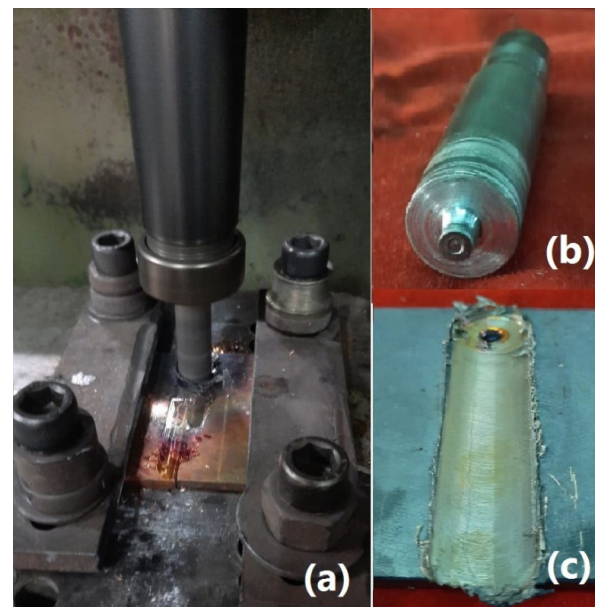


Fig. 2. Friction stir welding; a) experimental setup, b) tool, and c) work piece

Table 1. Composition of CMC

Plate No.	Symbol	Copper (Cu)	Tungsten (W)	Boron carbide (B ₄ C)
1	90 % CMC	90	5	5
2	85 % CMC	85	5	10
3	80 % CMC	80	5	15

Table 2. Input parameter and its levels

Specimen No.	Parameter	Units	Levels		
			L 1	L 2	L 3
1	Weight % of B ₄ C	%	5	10	15
2	Rotational speed	rpm	900	1200	1500
3	Welding speed	mm/min	9	12	15
4	Axial force	kN	3	6	9

Table 3. Design of experiment and output responses

Experiment No.	Weight % of B ₄ C	Rotational speed	Welding speed	Axial force	Hardness [HV10]	Tensile strength [N/mm ²]	Impact toughness [J]
1	5	900	9	3	83	19.25	3.3
2	5	1200	12	6	91	0.03	3.1
3	5	1500	15	9	45	21.45	3.5
4	10	900	12	9	128	75.455	4.1
5	10	1200	15	3	112	77.75	4.0
6	10	1500	9	6	119	63.821	4.2
7	15	900	15	6	157	22.444	3.9
8	15	1200	9	9	85	136.02	4.0
9	15	1500	12	3	100	153.93	3.8
10	5	900	15	9	82	23.25	2.9
11	5	1200	12	3	89	32.51	3.7
12	5	1500	9	6	59	38.24	3.2
13	10	900	9	9	119	68.25	3.9
14	10	1200	15	3	101	82.57	4.5
15	10	1500	12	6	117	38.14	4.2
16	15	900	15	6	148	120.48	4.5
17	15	1200	12	9	95	125.65	4.2
18	15	1500	9	3	113	148.37	4.9

1.1 Multi Objective Optimization Techniques TOPSIS:

TOPSIS is a popular and very powerful technique to separate the correct parametric mixture from the restricted investigated combination. The steps for this technique are scheduled below. [27]

Step 1: The conclusion matrix having ‘n’ characteristics and ‘m’ option and it is characterized in Eq. (1).

$$A_m = \begin{bmatrix} J_{11} & J_{12} & \dots & J_{1n} \\ J_{21} & J_{22} & \dots & J_{2n} \\ \vdots & \vdots & \ddots & \vdots \\ J_{m1} & J_{m2} & \dots & J_{mn} \end{bmatrix}, \quad (1)$$

where J_{ij} is the output of i^{th} option with relevance to the j^{th} characteristic.

Step 2: The normalization of the matrix is carried out with Eq. (2).

$$p_{ij} = \frac{J_{ij}}{\sqrt{\sum_{i=1}^m J_{ij}^2}}, \quad j = 1, 2, \dots, n. \quad (2)$$

Step 3: For each output, responses have been assigned with equal weights to be Wt_j ($j=1, 2, \dots, n$). The standardized weighted choice matrix $M=[m_{ij}]$ attained using the Eq. (3).

$$M = Wt_j p_{ij}, \quad (3)$$

where $\sum_{j=1}^n Wt_j = 1$.

Step 4: The suitable best solution is assessed using Eq. (4) and the worst solution is attained using Eq. (5).

$$M^+ = \left\{ \left(\sum_i^{\max} m_{ij} \mid j \in J \right), \left(\sum_i^{\min} m_{ij} \mid j \in J \mid j = 1, \dots, m \right) \right\} \\ = \{m_1^+, m_2^+, \dots, m_n^+\}, \quad (4)$$

$$M^- = \left\{ \left(\sum_i^{\min} m_{ij} \mid j \in J \right), \left(\sum_i^{\max} m_{ij} \mid j \in J \mid j = 1, \dots, m \right) \right\} \\ = \{m_1^-, m_2^-, \dots, m_n^-\}. \quad (5)$$

Step 5: The distributions among every option are intended from the best solutions are obtained using Eq. (6).

$$T_i^+ = \sqrt{\sum_{j=1}^n (M_{ij} - m_j^+)^2}, \quad i = 1, 2, \dots, m. \quad (6)$$

The division of option from the worst solution is attained using Eq. (7).

$$T_i^- = \sqrt{\sum_{j=1}^n (M_{ij} - m_j^-)^2}, \quad i = 1, 2, \dots, m. \quad (7)$$

Step 6: The relations closeness of the dissimilar options for the solutions are obtained using Eq. (8).

$$k_i = \frac{k_i^-}{k_i^+ + k_i^-}, \quad i = 1, 2, \dots, m. \quad (8)$$

Step 7: The k_i standards values are graded in downward order to discover the optimal parameters mixture.

1.2 Grey Relational Analysis Technique

In GRA, output reactions of different elements should be reformed into the dimensionless values. Therefore, those values are standardized to the variety of zero to one using Eqs. (9) to (12) [28]. The tensile, impact, and micro-hardness values must be higher, which considered better and intended using the Eq. (9); for lower, the superior is desirable, which is intended using Eq. (10).

$$R_i^*(s) = \frac{r_i(s) - \min r_i(s)}{\max r_i(s) - \min r_i(s)}, \tag{9}$$

$$r_i^*(s) = \frac{\max r_i(s) - r_i(s)}{\max r_i(s) - \min r_i(s)}, \tag{10}$$

where $i = 1, 2, \dots, m, s = 1, 2, \dots, n$, where m is the sum of experiment, n is the sum of the observed data. $R_i^*(s)$ is denoted as minimum - larger than better and $r_i^*(s)$ as maximum - smaller the better. The standardized values are added in Eq. (11), which is employed to compute the grey relational coefficient (GRC).

$$\lambda_i(S) = \frac{\Delta_{\min} + \xi \Delta_{\max}}{\Delta_{oi}(P) + \xi \Delta_{\max}}. \tag{11}$$

Here, $\Delta_{oi}(S)$ divergence series is attained from the orientation series $\lambda_0^*(S)$ and comparability series $\lambda_i^*(S)$. The variety $0 \leq \xi \leq 1$ comprised for the distinctive coefficient:

$$\xi = \frac{1}{n} \sum_{p=1}^n \xi_i(S). \tag{12}$$

Grey relational grade (Ψ_i) is added, summing up of grey relational coefficients which corresponds in Eq. (12). is assisted to discover the connection of situation and comparability ideals.

2 RESULTS AND DISCUSSION

2.1 Effect of Reinforcements on the Microstructure of Welding

SEM is employed to investigate the microstructural properties of the welding joints. The macro-size welding images of various reinforced specimens under different machining conditions are analysed. The microstructure of the welding zone and the parent

metal of the welding using various reinforced work materials (e.g., 90 % CMC, 85 % CMC and 80 % CMC) are presented in Figs. 3 to 5. The consistency of welding joint on all sides of the parent metal is found to be better in 80 % CMC materials than other reinforced work materials and lesser regularity found in 90 % CMC material. The microstructures of welding zone for all type of reinforced materials are analysed using SEM images. The SEM analysis shows that the dissemination of grains due to high temperatures enlarges the welding zone on the work material, which could be observed as a bright exterior next to the parent metal. The microstructures of various welding surfaces show that associated coarse grains with consistent grain outlines in a welding zone is attained by means of the elevated heat of the FSW process [20]. Fig. 3 presents the microstructure of welding zone and its field emission scanning electron microscopy (FESEM) image for 90 % CMC work material. In this, 90 % CMC material creates minor non-homogeneous welding on the parent metal; a small number of micro-voids were produced by over welding. Also, the distribution of welding is found to be higher on this CMC work material than others. Welding through 85 % CMC work material creates micro-cracks in the welds and a few granular fractures were observed, which is presented in Fig. 4. The effective diffusion of B₄C, W. and Cu produces extended dendrites in the welding zone which lead to micro-crack structures on the welding. Fig. 5 shows 80 % CMC work material, which provides superior consistent welding zone and a very minor amount of slip microstructure obtained across the welding surface [16]. White impulsive particles are found above the welding surface, which is due to the dispersion of Cu and W materials into the matrix exterior layer of work material. The elevated carbide content in the reinforcement material indicates the prominent oxidation at elevated temperature, which is leads to the development of molten metal on welding zone.

2.2 Micro-hardness

A Vickers micro-hardness test was conducted for various reinforced copper work materials on welding regions; the results of the welding presented in Fig. 6. The graph reveals that the hardness of the 90 % CMC work material is the lowest. The micro-hardness of welding is generally based on the microstructure variations. It is clear from Fig. 6 that the standard hardness of welding formed by 80 % CMC work material is 3.42 % higher than that of welding by 90 % CMC work material. Also, the hardness for 80 %

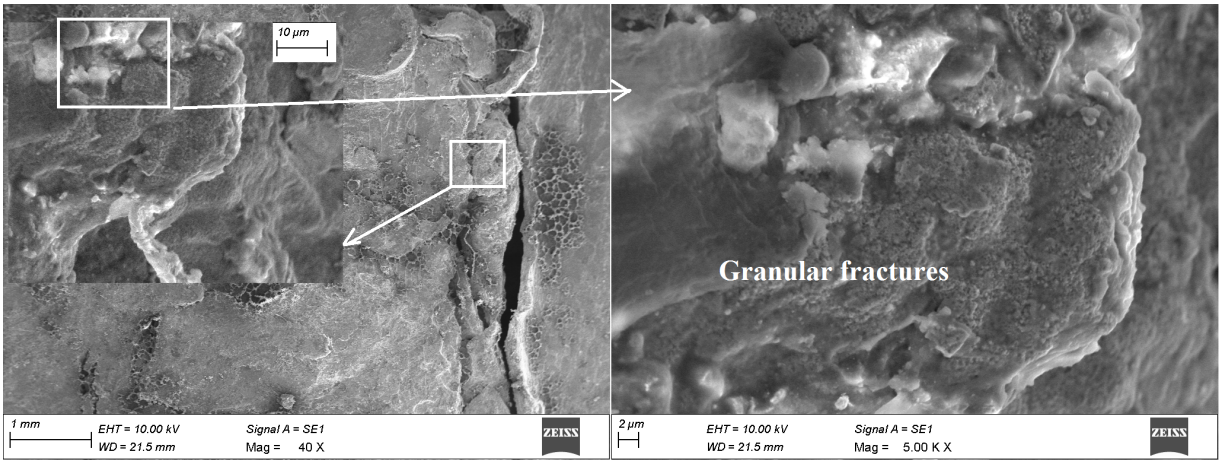


Fig. 3. SEM image of 90 % CMC welding zone

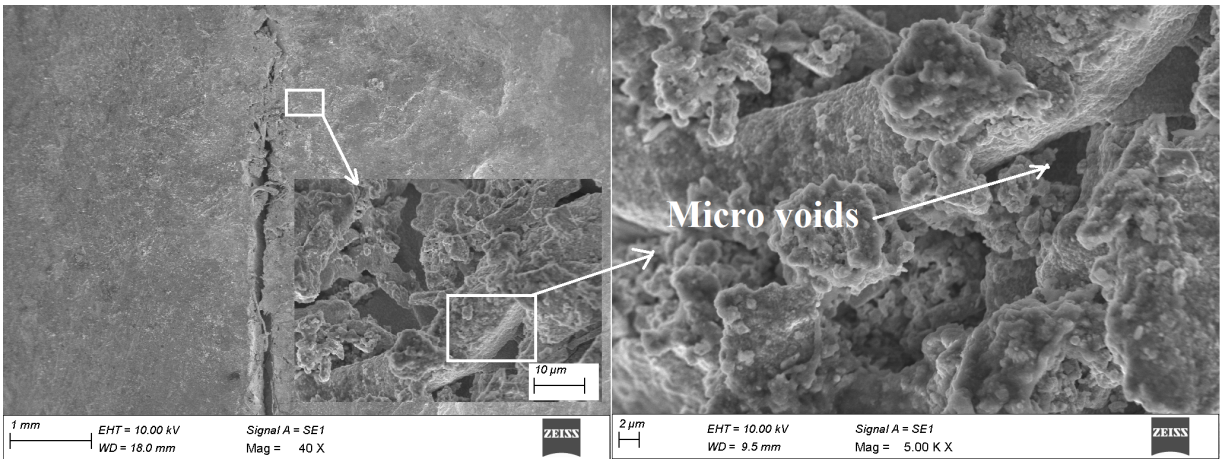


Fig. 4. SEM image of 85 % CMC welding zone

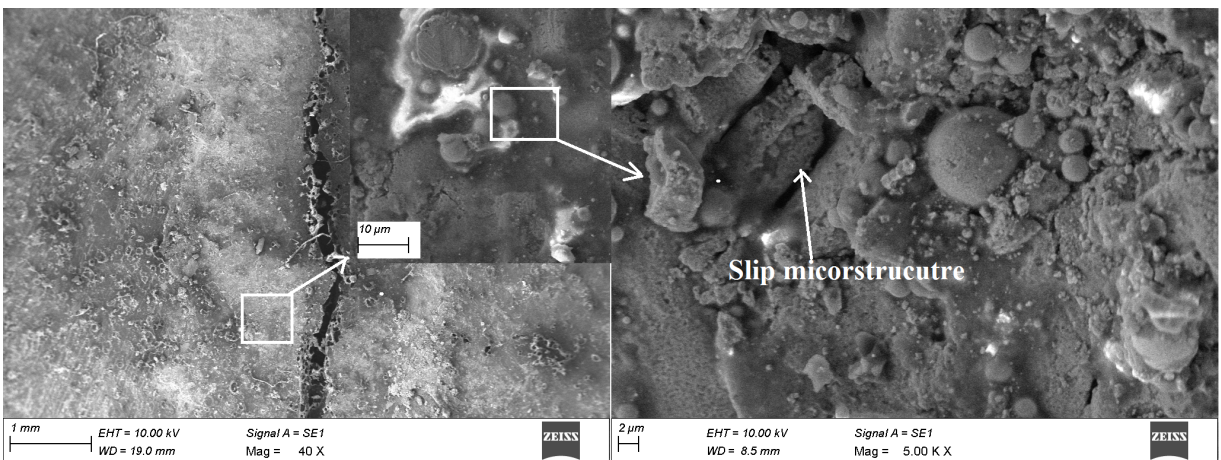


Fig. 5. SEM image of 80 % CMC welding zone

CMC work material at parent material is shown to be higher compared to the welding using 90 % CMC work material, due to the enhancement of carbide and W in the parent metal [20]. The standard hardness of

80 % CMC work material is 2.8 % more than that of 90 % CMC work material work material. The welding and parent metal hardness are 108 HV and 113 HV, respectively, when 80 % CMC work material. The

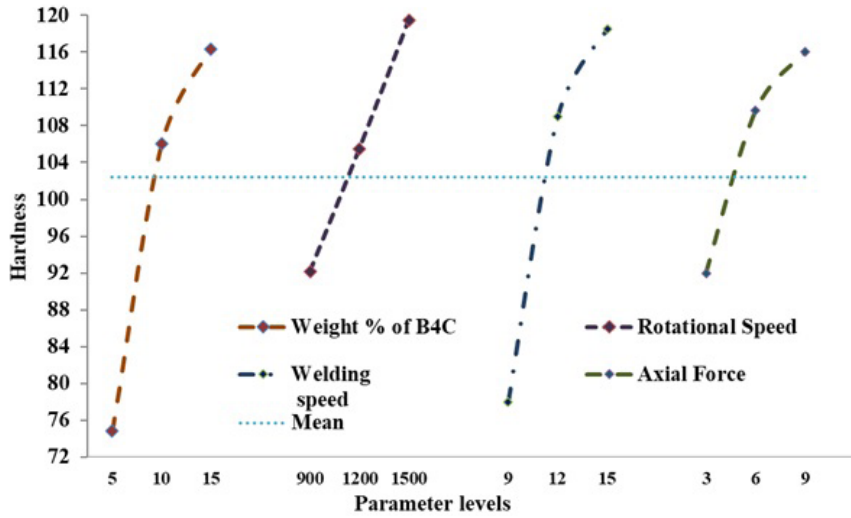


Fig. 6. Micro-hardness representation

addition of 15 % B₄C reinforcements on 90 % CMC metal requires more time to melt than 85 % CMC metals that make the microstructure alteration. It is implicit that standard hardness when using of 85 % CMC creates 2.56 % higher hardness compared to 80 % CMC materials. The alteration of cooling rate in welding zone modifies the crystal metal microstructure headed for an austenitic structure [21]. Also, the crystal microstructure is inflated with the increase in temperature, which becomes softer when welding. Hence, the standard hardness of welding was found to be less important than the welding and parent metal excluding 90 % CMC metals welding.

2.3 Tensile Properties

The average tensile strength of welding by different CMC materials is shown in Fig. 7. It is observed that the 90 % CMC materials creates 20 N/mm² tensile strength. The tensile strength of 85 % CMC and 80 % CMC materials welding produce 68 N/mm² and 119.2 N/mm² respectively, which is superior to the 90 % CMC materials. It is observed that all wedding samples create the higher tensile strength than 90 % CMC in all factors of welding parameters due to the increasing of reinforcements [31]. The cross-sections of welding for different CMC materials are presented in Fig. 8.

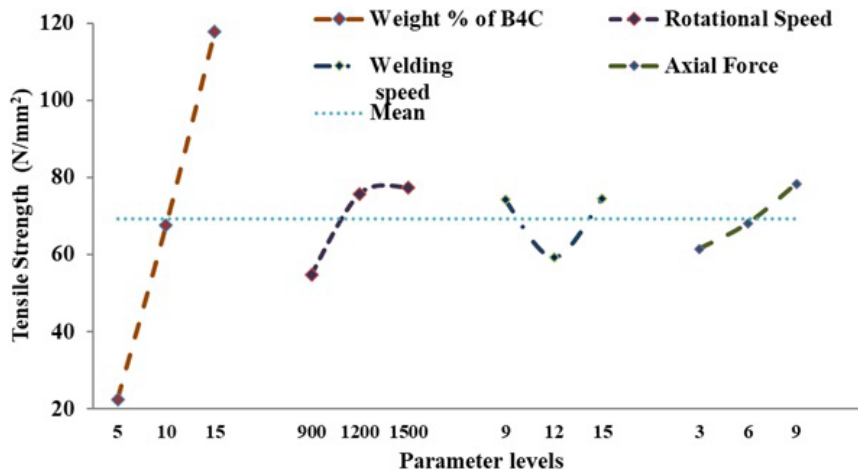


Fig. 7. Tensile strength representation

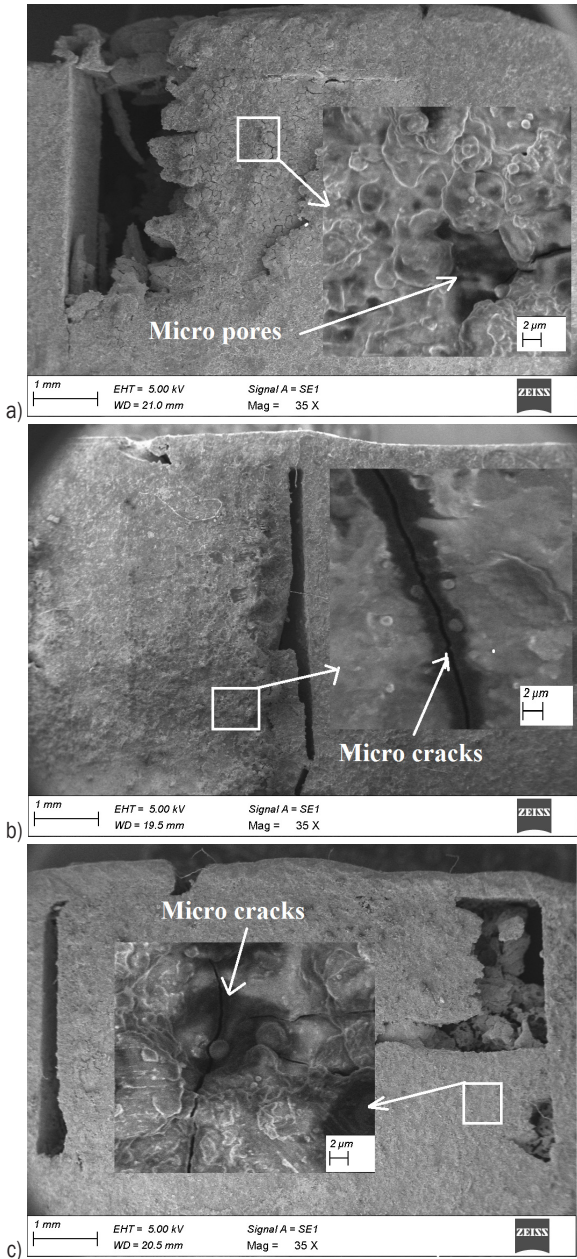


Fig. 8. SEM image of welding cross-sections; a) 90 % CMC, b) 85 % CMC, and c) 80 % CMC

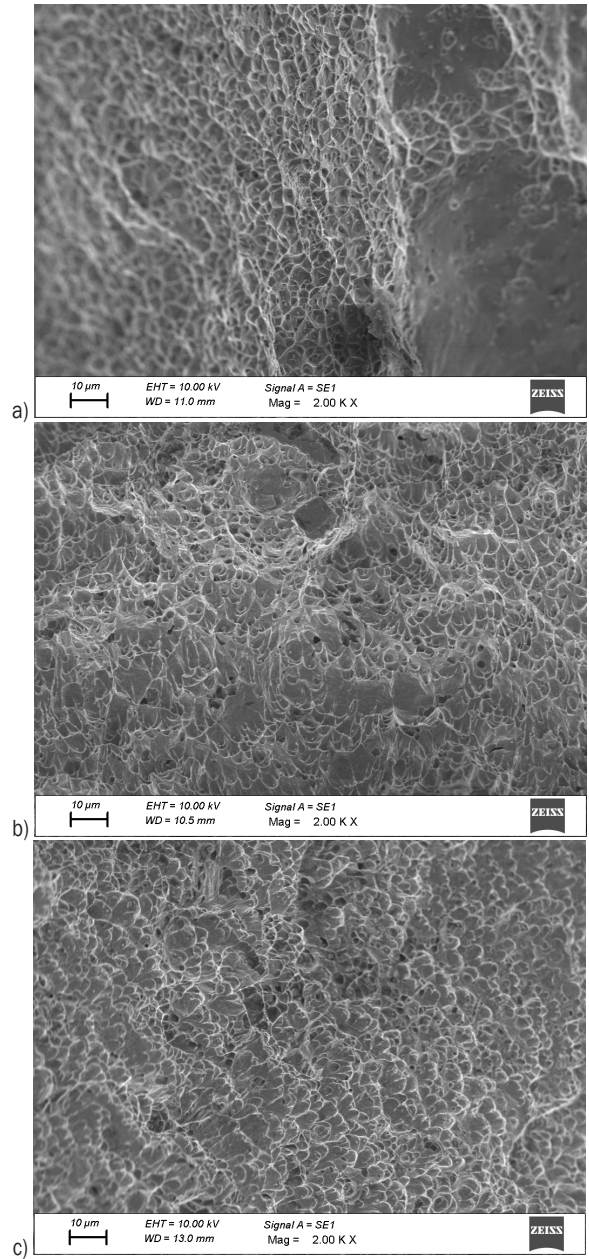
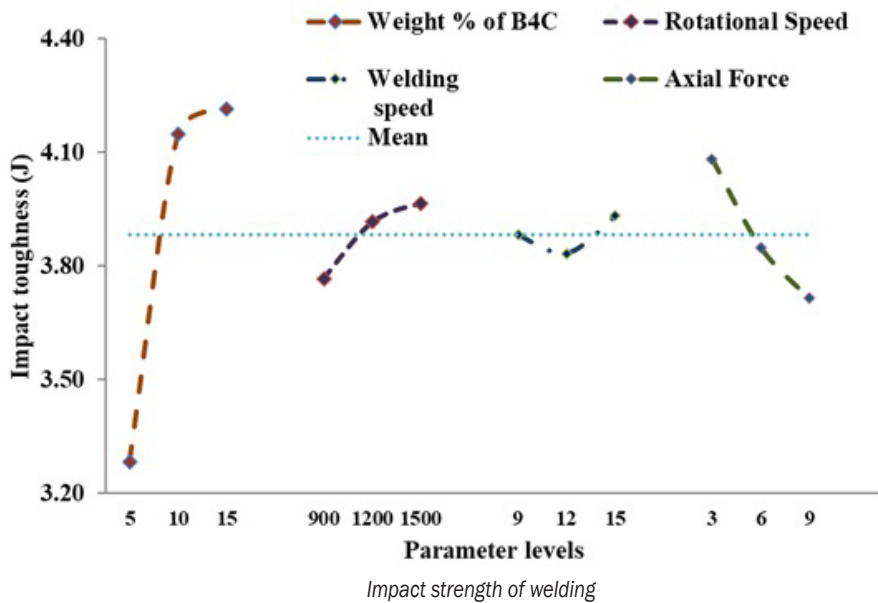


Fig. 9. SEM image of fractured cross section; a) 90 % CMC, b) 85 % CMC, and c) 80 % CMC

2.4 Impact Strength

Fig. 10 presents the impact strength for the different CMC welding samples under different parameter levels. It is apparent that addition of B₄C with CMC excites the creep strength in work material, which led to the elevated toughness. Of the various CMCs used as work material, the 80 % CMC work metal produces the maximum toughness of 4.39 J, and its cracked surface is shown in Fig. 9c. 80 % CMC work

metal produces 68 % upper toughness than that using of welding on 90 % CMC work metal. The SEM image in Fig. 9a shows the broken surfaces with 80 % CMC work metal welding specimen. It is apparent from the image that the sample shows the cleavage surface and mild micro-dimples as seen through white marks [22]. The 85 % CMC work metal produces the second-highest impact toughness of 4.6 J among



others. Hence, 10 % B₄C added CMC work metal produces 53 % higher impact toughness compared to the 90 % CMC. Fig. 9b presents the broken surface of welding with 90 % CMC work metal. According to the Fig. 9, 90 % CMC work metal produces a stringy microstructure and micro-voids over the broken surface. This is due to the easy movement of B₄C from one side to another side by the tool revolutions.

2.5 TOPSIS

The outcome responses of FSW process (e.g., hardness, tensile and impact strength) for different CMC work materials are optimized through the TOPSIS method. The preference values of outcome responses are calculated using Eq. (1) to (8). The weights for the responses are assigned equally under ideal conditions. The ranking of experimentation is presented in Table 4. The outcome responses of the experimentation are transformed from multi-attribute optimization to single objective optimization using Taguchi’s and TOPSIS method combination. The uppermost preference value (k_i) is considered the optimal parameter combination, and the highest rank is termed “first optimal solution”. Consequently, it is observed that the 7th experimental run (0.8376 k_i value) is selected as the optimal parameter combination for the finest performance of FSW process. The experimental runs 2nd and 15th presents the next suitable optimal parameter solution. Therefore, the suitable optimal parameter combination is found to be

that 15 % B₄C, 1200 rpm rotational speed, 9 mm/min welding speed and 9 kN axial force using TOPSIS.

Table 4. TOPSIS ranking

Experiment No.	T_i^+	T_i^-	Preference value, k_i	Rank
1	0.1749	0.3981	0.6948	4
2	0.1473	0.4558	0.7557	2
3	0.2588	0.3803	0.5950	7
4	0.2323	0.2910	0.5561	11
5	0.2484	0.2657	0.5168	12
6	0.2125	0.3041	0.5887	8
7	0.0869	0.4485	0.8376	1
8	0.4182	0.1156	0.2166	18
9	0.4523	0.1391	0.2352	17
10	0.1791	0.3938	0.6874	5
11	0.1829	0.3610	0.6636	6
12	0.2435	0.3410	0.5834	9
13	0.2173	0.2970	0.5775	10
14	0.2796	0.2366	0.4584	13
15	0.1594	0.3640	0.6954	3
16	0.3512	0.2487	0.4146	14
17	0.3857	0.1429	0.2703	15
18	0.4432	0.1521	0.2555	16

2.6 Table of ANOVA for TOPSIS

Analysis of variance (ANOVA) is the most suitable technique to find the significant and nonsignificant parameter from the experiments. The k_i values of various CMC work material under different machining

conditions are mathematically studied using ANOVA method, and all individual parameter solution over the outcome responses are investigated. Furthermore, the *F*-test results are employed to find the most significant parameter to obtain the good performance measure. Table 5 makes apparent that composite work materials, i.e., the percentage of reinforcements with copper material contributes more impact on welding characteristics by around 43.89 %. Subsequently, the significant factor is axial force that produces 32.68 % contribution on the FSW process.

Table 5. ANOVA for TOPSIS

Symbol	Machining parameter	df	SS	MS	F	% contribution
A	Rc	2	0.2645	0.1322	37.54	43.89
B	Rs	2	0.0808	0.0404	11.48	13.42
C	Ws	2	0.0285	0.0143	4.05	4.73
D	Af	2	0.1969	0.0985	27.95	32.68
E	Error	9	0.0317	0.0035		5.28
	Total	17	0.6024	0.0354		100

2.7 GRA Method

The GRA method is a prominent technique employed to optimize the process parameters of the FSW process, such as micro-hardness, and tensile and impact strength. The GRC and GRG values are derived from Eqs. (11) and (12) for all experiments. The weights for the outcome responses are assigned equally (i.e., 1) and GRG values are presented in Table 6. The highest GRG value is selected as optimal parameter solution. Hence, the table suggest that the 7th experimental run (0.8465) holds the first rank and is termed as the optimal solution for better performance. The experimental combinations 2nd (0.8461) and 10th (0.8226) have the next best optimal parameter combination using the GRA method. Therefore, the suitable and optimal parameter combination found to be that 15 % B₄C, 1200 rpm rotational speed, 9 mm/min welding speed and 9 KN axial force using GRA.

2.8 ANOVA for GRG

The results obtained from the GRG for the various parameter combinations are analysed mathematically using ANOVA, which is presented in Table 7. The GRA approach is used to optimize the obtained results for different CMC materials. According to this, the percentage of reinforcements in work materials affects the welding performances significantly at about 37.85

%. The axial force of welding tool creates impact on the welding performance around 33.22 %, which is the next significant factor in the FSW process.

Table 6. GRG ranking

Experiment No.	GRC			GRG	Rank
	Hardness	Tensile strength	Impact toughness		
1	0.6022	0.8890	0.8333	0.7748	4
2	0.6292	1.0000	0.9091	0.8461	2
3	0.5000	0.8778	0.7692	0.7157	7
4	0.7943	0.6711	0.6250	0.6968	10
5	0.7134	0.6645	0.6452	0.6743	13
6	0.7467	0.7070	0.6061	0.6866	11
7	1.0000	0.8729	0.6667	0.8465	1
8	0.6087	0.5309	0.6452	0.5949	17
9	0.6627	0.5000	0.6897	0.6175	15
10	0.5989	0.8689	1.0000	0.8226	3
11	0.6222	0.8257	0.7143	0.7207	6
12	0.5333	0.8011	0.8696	0.7347	5
13	0.7467	0.6929	0.6667	0.7021	9
14	0.6667	0.6509	0.5556	0.6244	14
15	0.7368	0.8015	0.6061	0.7148	8
16	0.9256	0.5610	0.5556	0.6807	12
17	0.6437	0.5506	0.6061	0.6001	16
18	0.7179	0.5092	0.5000	0.5757	18

Table 7. ANOVA table for GRG

Sym-bol	Machining parameter	df	SS	MS	F	% contribution
A	Ce	2	0.0438	0.0219	0.00825191	37.85
B	Vm	2	0.0246	0.0123	68.1870725	21.30
C	Cd	2	0.0072	0.0036	19.9226318	6.22
D	Te	2	0.0384	0.0192	106.335841	33.22
E	Error	9	0.0016	0.0002		1.41
	Total	17	0.1157	0.0068		100

3 CONCLUSIONS

This paper attempted to express the advantages and performance study of FSW process with copper composite material in reinforcement addition. Three CMC materials are prepared using pure copper (Cu) as the matrix; tungsten (W) and boron carbide (B₄C) particles are reinforcements for various concentrations. The multi-objective decision-making methods, such as TOPSIS and GRA methods are used to find the optimal parameter combination, and experiments are planned according to the L 18 orthogonal array (OA), using the most influential parameters, such as the percentage of boron carbide

reinforcements, tool rotational speed, welding speed, and axial force.

- Based on the optimization results, 15 % of B₄C, 900 rpm rotational speed, 15 mm/min welding speed and 6 kN axial forces produces the better mechanical strength on the welding using both TOPSIS and GRA techniques.
- The microstructure of welding reveals that consistency of welding joint on all sides of the parent metal is found to be better in 15 % B₄C reinforced CMC materials than other reinforced work materials, and lesser regularity found in 5 % B₄C reinforced CMC material.
- 80 % CMC and 85 % CMC reinforced copper work metal produces 68 % and 10 % higher impact toughness respectively than that using of welding on 90%CMC work metal.
- Based on the ANOVA table of TOPSIS, composite work materials, the percentage of reinforcements with copper material contributes more impact on welding characteristics of around 43.89 %. Subsequently, the next significant factor is axial force, which produces a 32.68 % contribution on the FSW process.
- Therefore, the mechanical strength of welding with FSW process increases with an increase of the percentage of reinforcement in the copper composite material. Also, these types of materials could be used for the applications for which high mechanical strength is required.
- Furthermore, experiments with hybrid composite with pure copper can be conducted, and assistance with FSW process such as heat energy can be experimentally tested with the FSW process to enhance the welding quality.

4 REFERENCES

- [1] Zamani, S.M.M., Behdinin, K., Razfar, M.R., Fatmehsari, D.H., Mohandesi, J. A. (2021). Studying the effects of process parameters on the mechanical properties in friction stir welding of Al-SiC composite sheets. *The International Journal of Advanced Manufacturing Technology*, vol. 113, p. 3629-3641, DOI:10.1007/s00170-021-06852-7.
- [2] Bakhtiar Argesi, F., Shamsipur, A., Mirsalehi, S.E. (2021). Preparation of bimetallic nano-composite by dissimilar friction stir welding of copper to aluminum alloy. *Transactions of Nonferrous Metals Society of China*, vol. 31, no. 5, p. 1363-1380, DOI:10.1016/S1003-6326(21)65583-8.
- [3] Sudhagar, S., Gopal, P.M. (2022). Investigation on mechanical and tribological characteristics Cu/Si₃N₄ surface composite developed through friction stir processing. *Silicon*, vol. 14, p. 4207-4216, DOI:10.1007/s12633-021-01206-0.
- [4] Thapliyal, S., Mishra, A. (2021). Machine learning classification-based approach for mechanical properties of friction stir welding of copper. *Manufacturing Letters*, vol. 29, p. 52-55, DOI:10.1016/j.mfglet.2021.05.010.
- [5] Harisha, P., Nanjundaswamy, H.M., Divakar, H.N., Krishnan, D. (2022). Tensile properties of aluminium and copper alloys friction stir welded joints. *Materials Today: Proceedings*, vol. 54, p. 223-227, DOI:10.1016/j.matpr.2021.08.297.
- [6] Nagesh, G., Rao, K.N., Anurag, K.M., Abhinav, N. (2021). Investigation of mechanical properties on non-ferrous alloys of copper and brass joints made by friction stir welding. *IOP Conference Series: Materials Science and Engineering*, vol. 1057, no. 1, art. ID 012062, DOI:10.1088/1757-899X/1057/1/012062.
- [7] Senthil, S.M., Parameshwaran, R., Nathan, S.R., Kumar, M.B., Deepandurai, K. (2020). A multi-objective optimization of the friction stir welding process using RSM-based-desirability function approach for joining aluminum alloy 6063-T6 pipes. *Structural and Multidisciplinary Optimization*, vol. 62, p. 1117-1133, DOI:10.1007/s00158-020-02542-2.
- [8] Karrar, G., Galloway, A., Toumpis, A., Li, H., Al-Badour, F. (2020). Microstructural characterisation and mechanical properties of dissimilar AA5083-copper joints produced by friction stir welding. *Journal of Materials Research and Technology*, vol. 9, no. 5, p. 11968-11979, DOI:10.1016/j.jmrt.2020.08.073.
- [9] Kolnes, M., Kübarsepp, J., Sergejev, F., Kolnes, M., Tarraste, M., Viljus, M. (2020). Performance of ceramic-metal composites as potential tool materials for friction stir welding of aluminium, copper and stainless steel. *Materials*, vol. 13, no. 8, art. ID 1994, DOI:10.3390/ma13081994.
- [10] Sahu, P.K., Pal, S., Das, B., Shi, Q. (2020). Fabrication and effect of Mg-Zn solid solution via Zn foil interlayer alloying in FSW process of magnesium alloy. *Archives of Civil and Mechanical Engineering*, vol. 20, art. ID 137, DOI:10.1007/s43452-020-00141-y.
- [11] Jimenez-Mena, N., Jacques, P. J., Ding, L., Gauquelin, N., Schryvers, D., Idrissi, H., Simar, A. (2019). Enhancement of toughness of Al-to-steel friction melt bonded welds via metallic interlayers. *Materials Science and Engineering: A*, vol. 740-741, p. 274-284, DOI:10.1016/j.msea.2018.10.101.
- [12] Garg, A., Bhattacharya, A. (2019). Influence of Cu powder on strength, failure and metallurgical characterization of single, double pass friction stir welded AA6061-AA7075 joints. *Materials Science and Engineering: A*, vol. 759, 661-679, DOI:10.1016/j.msea.2019.05.067.
- [13] D'Souza, A., Rao, S.S., Herbert, M.A. (2019). Assessment of influence of process parameters on properties of friction stir welded Al-Ce-Si-Mg aluminium alloy. *Materials Research Express*, vol. 6, no. 8, art. ID 086504, DOI:10.1088/2053-1591/ab1aec.
- [14] Shettigar, A.K., Herbert, M.A., Rao, S. S. (2019). Microstructure evolution and mechanical properties of friction stir welded AA6061/rutile composite. *Materials Research Express*, vol. 6, art. ID 0865i7, DOI:10.1088/2053-1591/ab0f4e.
- [15] Khojastehnezhad, V.M., Pourasl, H.H. (2018). Microstructural characterization and mechanical properties of aluminum 6061-T6 plates welded with copper insert plate (Al/Cu/Al) using friction stir welding. *Transactions of Nonferrous Metals*

- Society of China*, vol. 28, no. 3, p. 415-426, DOI:10.1016/S1003-6326(18)64675-8.
- [16] Babu, K.K., Panneerselvam, K., Sathiya, P., Haq, A.N., Sundararajan, S., Mastanaiah, P., Murthy, C.S. (2018). Parameter optimization of friction stir welding of cryorolled AA2219 alloy using artificial neural network modeling with genetic algorithm. *The International Journal of Advanced Manufacturing Technology*, vol. 94, p. 3117-3129, DOI:10.1007/s00170-017-0897-6.
- [17] Peddavarapu, S., Raghuraman, S., Bharathi, R.J., Sunil, G.V.S., Manikanta, D.B.N.S. (2017). Micro structural investigation on friction stir welded Al-4.5Cu-5TiB2 Composite. *Transactions of the Indian Institute of Metals*, vol. 70, p. 703-708, DOI:10.1007/s12666-017-1072-3.
- [18] Herbert, M.A., Shettigar, A.K., Nigalye, A.V., Rao, S.S. (2016). Investigation on microstructure and mechanical properties of friction stir welded AA6061-4.5Cu-10SiC composite. *IOP Conference Series: Materials Science and Engineering*, vol. 114, no. 1, art. ID. 012125, DOI:10.1088/1757-899X/114/1/012125.
- [19] Sahu, P.K., Kumari, K., Pal, S., Pal, S.K. (2016). Hybrid fuzzy-grey-Taguchi based multi weld quality optimization of Al/Cu dissimilar friction stir welded joints. *Advances in Manufacturing*, vol. 4, p. 237-247, DOI:10.1007/s40436-016-0151-8.
- [20] Ahmadkhaniha, D., Heydarzadeh Sohi, M., Zarei-Hanzaki, A., Bayazid, S.M., Saba, M. (2015). Taguchi optimization of process parameters in friction stir processing of pure Mg. *Journal of Magnesium and Alloys*, vol. 3, no. 2, p. 168-172, DOI:10.1016/j.jma.2015.04.002.
- [21] Shirazi, H., Kheirandish, S., Safarkhanian, M.A. (2015). Effect of process parameters on the macrostructure and defect formation in friction stir lap welding of AA5456 aluminum alloy. *Measurement*, vol. 76 p. 62-69, DOI:10.1016/j.measurement.2015.08.001.
- [22] Kumar, A., Veeresh Nayak, C., Herbert, M.A., Rao, S.S. (2014). Microstructure and hardness of friction stir welded aluminium-copper matrix-based composite reinforced with 10 wt-% SiCp. *Materials Research Innovations*, vol. 18, S6-84-S6-89, DOI:10.1179/1432891714Z.0000000001016.
- [23] Suresh, S., Natarajan, E., Franz, G., Rajesh, S. (2022). Differentiation in the SiC filler size effect in the mechanical and tribological properties of friction-spot-welded AA5083-H116 alloy. *Fibers*, vol. 10, no. 12, art. ID 109, DOI:10.3390/fib10120109.
- [24] Suresh, S., Elango, N., Venkatesan, K., Lim, W.H., Palanikumar, K., Rajesh, S. (2020). Sustainable friction stir spot welding of 6061-T6 aluminium alloy using improved non-dominated sorting teaching learning algorithm. *Journal of Materials Research and Technology*, vol. 9, no. 5, p. 11650-11674, DOI:10.1016/j.jmrt.2020.08.043.
- [25] Suresh, S., Venkatesan, K., Natarajan, E., Rajesh, S. (2020). Performance analysis of nano silicon carbide reinforced swept friction stir spot weld joint in AA6061-T6 alloy. *Silicon*, vol. 13, p. 3399-3412, DOI:10.1007/s12633-020-00751-4.
- [26] Suresh, S., Natarajan, E., Shanmugam, R., Venkatesan, K., Saravanakumar, N., Anto Dilip, A. (2022). Strategized friction stir welded AA6061-T6/SiC composite lap joint suitable for sheet metal applications. *Journal of Materials Research and Technology*, vol. 21, p. 30-39, DOI:10.1016/j.jmrt.2022.09.022.
- [27] Soundararajan, M., Thanigaivelan, R. (2018). Investigation on electrochemical micromachining (ECMM) of copper inorganic material using UV heated electrolyte. *Russian Journal of Applied Chemistry*, vol. 91, p. 1805-1813, DOI:10.1134/S1070427218110101.
- [28] Soundararajan, M., Thanigaivelan, R. (2019). Investigation of electrochemical micromachining process using ultrasonic heated electrolyte. *Advances in Micro and Nano Manufacturing and Surface Engineering*, p. 423-434. Springer, Singapore, DOI:10.1007/978-981-32-9425-7_38.
- [29] Saravanan, K.G., Thanigaivelan, R., Soundararajan, M. (2021). Comparison of Electrochemical Micromachining Performance using TOPSIS, VIKOR and GRA for Magnetic field and UV rays heated Electrolyte. *Bulletin of the Polish Academy of Sciences, Technical Sciences*, vol. 69, no. 5, DOI:10.24425/bpasts.2021.138816.
- [30] Soundararajan, M., Thanigaivelan, R. (2017). Intervening variables in electrochemical micro machining for copper. *International Conference on Precision, Meso, Micro and Nano Engineering*, p. 263-266.

Fuzzy and Matlab/Simulink Modelling of the Air Compression Refrigeration Cycle

Amjad Alsakarneh^{1,*} – Lina Momani² – Taha Tabaza³

¹ Yarmouk University, Hijjawi Faculty for Engineering Technology, Department of Mechanical Engineering, Jordan

² Higher Colleges of Technology, Fujairah Men's College, Engineering Division, UAE

³ AL-Zaytoonah University of Jordan, Department of Mechanical Engineering, Jordan

The coefficient of performance (COP) for a gas refrigeration cycle was estimated using Matlab/Simulink and fuzzy logic. A Matlab/Simulink model of the gas refrigeration cycle was developed, and the output was compared to theoretical data. Additionally, fuzzy logic was used to estimate the COP for arbitrary low- and high-pressure levels. Simulation results were used to develop a multi-input-multi-output (MIMO) fuzzy Takagi-Sugeno-Kang (TSK)-based model. Both the Matlab/Simulink and the MIMO fuzzy model were found to be very well correlated with theoretical results, with an error of less than 2%. These results demonstrate the effectiveness of using fuzzy logic to analyse gas refrigeration cycles and suggest that this approach can be extended to analyse other thermodynamic cycles.

Keywords: coefficient of performance, Matlab/Simulink, Takagi-Sugeno-Kang, refrigeration cycles

Highlights

- The coefficient of performance (COP) for a gas refrigeration cycle was assessed using a modern intelligent tool, specifically fuzzy logic.
- To verify the results obtained by fuzzy logic, a simulation study was conducted over a wide range of low and high pressures in the cycle.
- The fuzzy logic approach was found to produce results very similar to the simulated COP, with a root mean square error of less than 2%.
- Fuzzy logic was found to be a fast approach for estimating the COP with limited knowledge of gas refrigeration cycles.

0 INTRODUCTION

Thermodynamics has a wide range of applications, including refrigeration, which involves the transfer of heat from a lower temperature region to a higher temperature one [1] and [2]. The air compression refrigeration cycle is a well-known example of this process, utilizing air as a working fluid instead of chlorofluorocarbon (CFC). This type of refrigeration is commonly used in airplane air conditioning systems, where pressurized air from the engine compressors is utilized. In recent years, researchers have shown more interest in this type of refrigeration due to its environmental advantages, as it has a positive impact on the ozoneosphere. Additionally, the working fluid for this refrigeration cycle is readily available at no cost, making it economically attractive. However, due to the low efficiencies of the compressor and expander [3] and [4], the coefficient of performance (COP) of this refrigeration cycle is relatively low.

The closed-air refrigeration cycle is typically comprised of four components: the air cooler, refrigerator, compressor, expander, and motor. Fig. 1 displays the four components of the refrigeration cycle, where the refrigerator holds air at a low pressure and the air cooler holds air at a high pressure.

Many studies, such as [5] and [6], have investigated the simulation and thermodynamic analysis of this cycle. Gigiel et al. [7] compared the air cycle and the CFC conventional freezing cycle. Further research regarding the optimization of the air refrigeration cycle using finite time thermodynamics and entropy generation minimization has been discussed in [8] and [9].

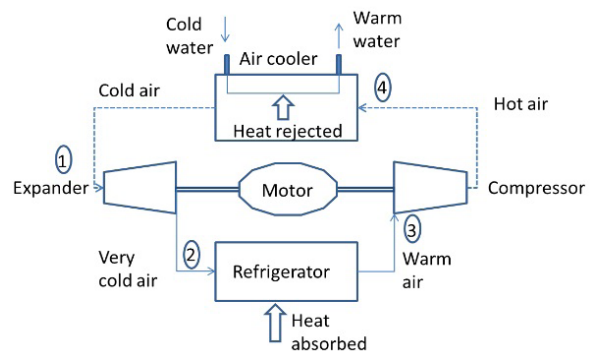


Fig. 1. Air refrigeration cycle (dashed and solid lines stand for high and low pressures, respectively)

Refrigeration system designers aim to maximize efficiency while minimizing energy consumption and production costs. Several variables have an

effective role in determining which combination of properties can be used to increase the coefficient of performance (COP) of the system. Kizilkan [10] conducted a performance analysis of a variable-speed refrigeration system using artificial neural networks. The objective of the study and the learning procedure was to identify the optimal set of weights that would produce the correct output for any input. The output of the network was compared to a desired response to generate an error, and the performance of the network was evaluated in terms of the desired signal and the convergence criterion. Fuzzy logic and artificial neural networks (ANNs) have been widely used in the literature to model complex mechanical systems [11] and [12]. Sahin [13], for example, used ANNs and adaptive neuro-fuzzy (ANFIS) to analyse the performance of a single-stage vapour compression refrigeration system with an internal heat exchanger using refrigerants R134a, R404a, and R407c. A comprehensive review of the applications of artificial neural networks for refrigeration cycles was presented in [14].

This research work proposes an alternative method for estimating the coefficient of performance (COP) using fuzzy logic as a tool, eliminating the need for analytical modelling of the refrigeration cycle. The researchers developed two models to estimate the COP of gas refrigeration cycles: the first model utilized a Matlab/Simulink model and direct mathematical relations and models, while the second model employed fuzzy logic. Both models utilized the low and high pressures of the cycle as inputs and the COP as an output. These results can be applied to modelling and simulating other refrigeration cycles, specifically, and thermodynamic cycles, generally.

1 METHODS

In this section, the gas refrigeration cycle model development using Matlab/Simulink is described. Matlab/Simulink has been extensively used by researchers for modelling and simulating mechanical systems. Milecki and Rybarczyk [15], for instance, employed Matlab/Simulink to simulate the behaviour of an electrohydraulic proportional valve. The development process starts with the calibration of the thermodynamic properties of air, as described below:

$$h = f(P_r), \quad (1)$$

$$h = f(T), \quad (2)$$

where h is the enthalpy (kJ/kg), P_r is the relative pressure, and T is the temperature in Kelvin.

To obtain the enthalpy fitted model, a power function in the form of ($h = ax^b + c$) is suggested. By utilizing the curve-fitting toolbox (CFT) in Matlab, the following results are obtained:

$$h(P_r) = 333.70 \times P_r^{0.2539} - 65.14, \quad (3)$$

$$h(T) = 0.391 \times T^{1.136} + 43.91. \quad (4)$$

To evaluate the accuracy of this model, the root mean square error (RMSE) is utilized, which is less than 1 % for the enthalpy for both Eqs. (3) and (4). Figs. 2a and b depict the original data, obtained from the thermodynamics tables, and the fitted data generated through this model.

In addition to the enthalpy data, the relative pressure as a function of temperature and temperature as a function of relative pressure are also required. These relationships are generated using the curve fitting toolbox, and the resulting equations are as follows:

$$P_r(T) = 1025 \times 10^{-11} \times T^{4.333} + 5.586, \quad (5)$$

$$T(P_r) = 395 \times P_r^{0.221} - 125.4. \quad (6)$$

To assess the performance of the developed model, the root mean square error (RMSE) is used as an evaluation metric. The RMSE is determined to be less than 1.5 % for both Eqs. (5) and (6), indicating good agreement between the fitted data and the original data obtained from the thermodynamics tables. This is further supported by Figs. 2c and d, which show the fitted data closely overlapping with the original data.

Using the fitted functions described earlier, the researchers developed a complete Simulink model of the gas refrigeration cycle. This model takes the low and high pressures of the cycle as input and produces the COP as output. A block diagram of the Simulink model is depicted in Fig. 3.

In the compressor subsystem, it is assumed that the air enters the compressor with a temperature of 285 K and a pressure of one atmospheric pressure. Using Eqs. (4) and (5), the enthalpy and relative pressure can be calculated. The thermodynamic properties of the air at the exit can be determined by applying the conservation of mass and energy principles.

$$P_{r2} = \frac{P_2}{P_1} P_{r1}.$$

The exit enthalpy and temperature can be determined using the computed value of the P_r from Eqs. (3) and (6).

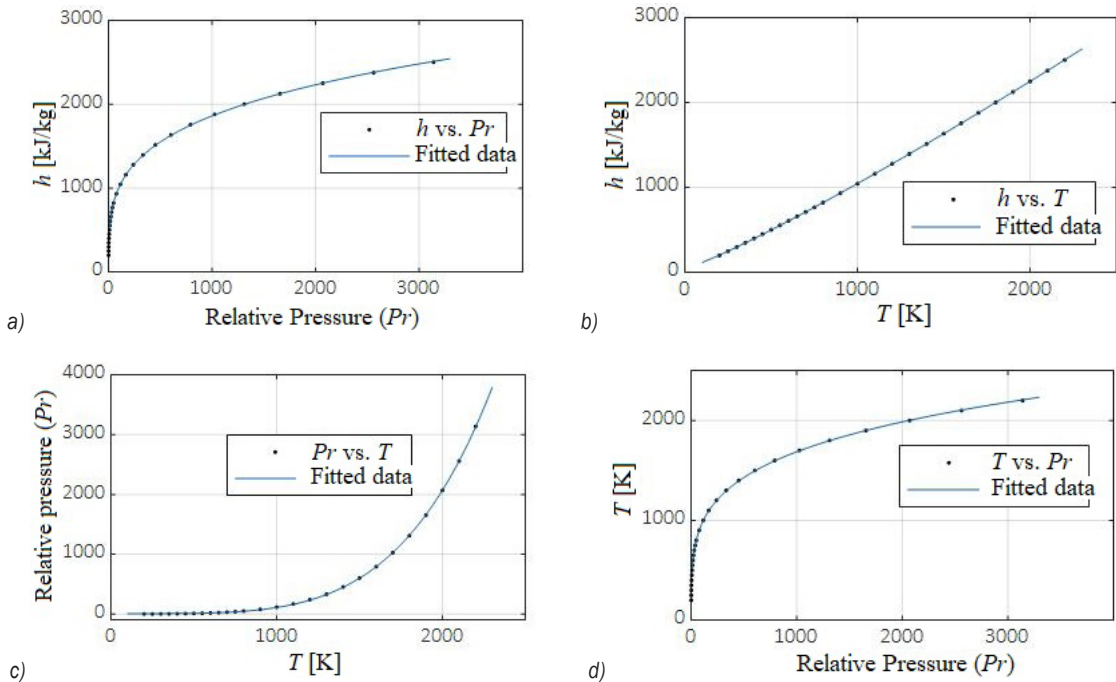


Fig. 2. Displays a comparison between the simulated data obtained from the developed models and the data obtained from thermodynamics tables; a) the enthalpy as a function of relative pressure, b) the enthalpy as a function of temperature, c) the relative pressure as a function of temperature, and d) the temperature as a function of relative pressure

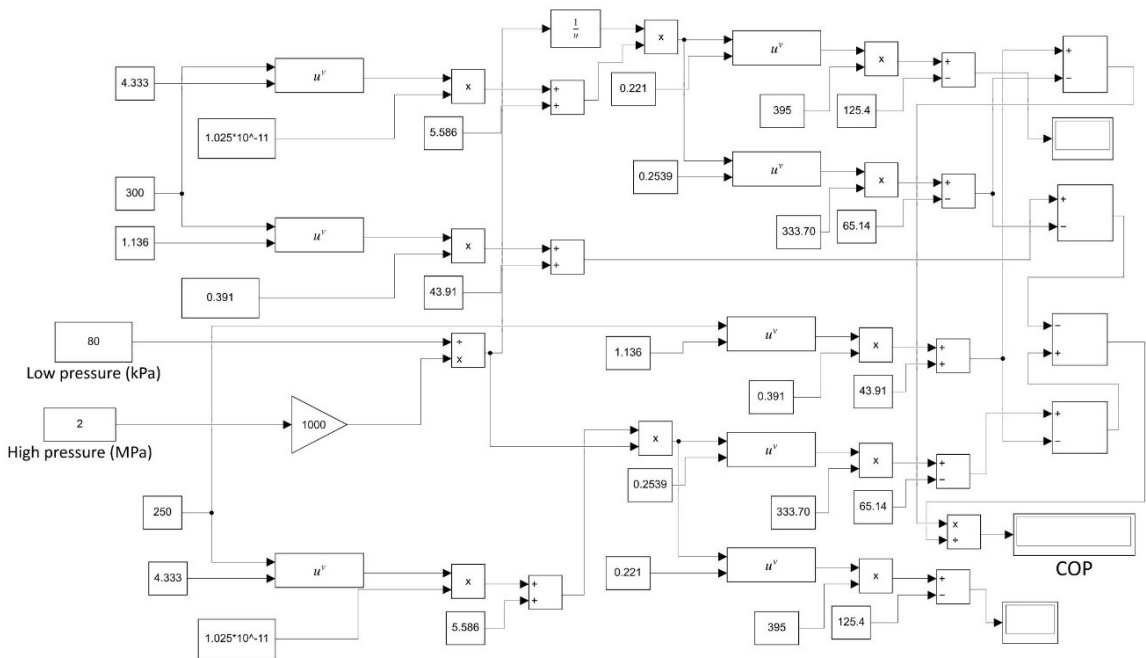


Fig. 3. The gas refrigeration cycles model

In the Turbine subsystem, the air enters the turbine with the third state, which is the exit of the condenser and exits the turbine with the fourth state. The enthalpy and relative pressure of the third state

obtained from the condenser subsystem are used to calculate the enthalpy and relative pressure of the fourth state, using Eqs. (4) and (5), respectively.

$$P_{r4} = \frac{P_4}{P_3} P_{r3}$$

Using the relative pressure, the enthalpy and temperature can be determined using Eqs. (3) and (6).

In the evaporator model, the absorbed energy in the condenser (q_L) can be calculated as the difference between the enthalpies of the first and fourth states, which is given by the following equation:

$$q_L = h_1 - h_4 \tag{7}$$

2 EXPERIMENTAL

The components of a fuzzy expert system include fuzzification, a knowledge base, a fuzzy inference engine, and defuzzification. A summary of how these components operate is provided below:

1. Fuzzification: To perform fuzzification in a fuzzy expert system, input values are transformed into fuzzy values according to a specific membership function. In this case, the proposed method uses a Gaussian function for input membership.
2. Knowledge Base: In the knowledge base component of a fuzzy expert system, rules are created based on the expertise and experience of the system's designer. Typically, each rule is given equal weight, though some rules may be given more weight based on expert judgement. This component establishes the connections and regulations between input and output values. The proposed method for this system uses nine rules that encompass all possible combinations of the input membership functions.
3. Fuzzy inference engine: The fuzzy inference engine component of a fuzzy expert system utilizes expert knowledge-based rules to make inferences from the available information. One popular method of inference is Takagi-Sugeno-Kang (TSK) inference. In TSK inference, the

existing rules are combined using the Max-Min operation.

4. Defuzzification: Defuzzification is the process of converting fuzzy information into a specific value. One common technique for defuzzification is the weighted average method, which is simple and widely used. The method of defuzzification that uses weighted averages is also known as the Sugeno defuzzification method. It is suitable for fuzzy sets with symmetrical output membership functions and produces results that are similar to the centroid of area (COA) method.

The proposed method involves the development of a fuzzy logic model that is based on the input-output data of the COP obtained from the mathematical models and relations of the gas refrigeration cycle. The data set that is generated is then used to structure the fuzzy model, including the input and output membership functions, as well as the if-then rules. We attempted to optimize the membership functions used for the input variables by trying two and four functions. However, the accuracy of the two-function approach was only about 95 %, while the four-function approach was very close to the three-function approach, with an error of about 1 %. Therefore, we decided to adopt the three-function approach, as it provided a better correlation compared to the two-function approach and faster computation time compared to the four-function approach.

The refrigeration cycle includes four sub-systems: the evaporator, compressor, turbine, and condenser. However, the proposed fuzzy model only considers the input variables, which are the low and high pressures, and the output variable, which is the COP. For the low and high pressures, three membership functions are assumed, using Gaussian functions as follows:

$$LPIMF_i = e^{-\frac{(x-A_i)^2}{B_i^2}}, \text{ where } i = 1, 2, 3, \tag{8}$$

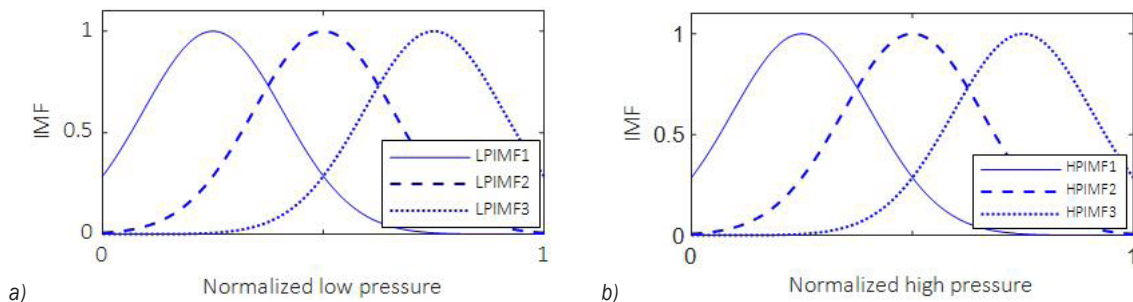


Fig. 4. The input membership functions before tuning of a) low pressure, and b) high pressure

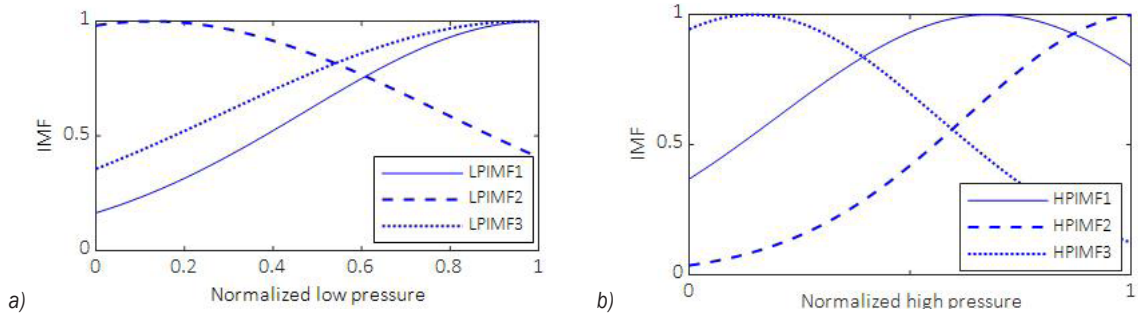


Fig. 5. The input membership functions after tuning of a) low pressure; and b) high pressure

$$HPIMF_i = e^{-\frac{(x-C_i)^2}{D_i^2}}, \text{ where } i = 1, 2, 3, \quad (9)$$

where L_i and H_i are the i^{th} membership function of low and high pressures, respectively, A_i , B_i , C_i and D_i are the design parameters of i^{th} input membership functions. Fig. 4 shows the input and output membership functions.

For the if-then rules, Table 1 lists the if-then rules together with the output membership functions.

Where COP were calculated as follows:

$$COP = \sum_{i=1}^9 (a_i \times L_i + b_i \times H_i + c_i). \quad (10)$$

The authors previously presented a method to estimate the coefficients a , b , and c of the TSK model using the available experimental or simulation data. This was achieved by generating an optimized TSK model through the application of a nonlinear least square method, as described in reference [16].

3 NUMERICAL EXAMPLES RESULTS

After performing simulations using the Matlab/Simulink model with various input pressures, a dataset

was generated with the COP as the output. The range of low pressures considered was from 100 kPa to 200 kPa, while the range of high pressures was from 1.0 MPa to 3.0 MPa. The MATLAB code used the COP data generated from the Simulink model and applied the least square method to estimate the optimal values of the membership function coefficients.

The accuracy of the results is demonstrated by the RMSE value of 0.01953, which means that the expected COP error based on the model is less than 2 % on each occasion. Table 2 provides all the If-Then rules and output membership functions (OMF). Increasing the order of the OMF could be a potential area for future work, but it may require high-speed computers.

Fig. 5a depicts the relationship between the input variables of low and high pressures and the output variable of COP, as predicted by the developed model. The accuracy of the model is evident from the plot, with the error being negligible. Furthermore, Fig. 5b displays the residuals of the developed surface with a maximum error of less than 0.02, indicating the accuracy of the model's predictions.

Table 1. The if-then rules and output membership functions

No.	If low pressure is		If high pressure is		The COP is
1.	$LPIMF_1$	and	$HPIMF_1$	then	$a_1 \times L + b_1 \times H + c_1$
2.	$LPIMF_2$		$HPIMF_1$		$a_2 \times L + b_2 \times H + c_2$
3.	$LPIMF_3$		$HPIMF_1$		$a_3 \times L + b_3 \times H + c_3$
4.	$LPIMF_1$		$HPIMF_2$		$a_4 \times L + b_4 \times H + c_4$
5.	$LPIMF_2$		$HPIMF_2$		$a_5 \times L + b_5 \times H + c_5$
6.	$LPIMF_3$		$HPIMF_2$		$a_6 \times L + b_6 \times H + c_6$
7.	$LPIMF_1$		$HPIMF_3$		$a_7 \times L + b_7 \times H + c_7$
8.	$LPIMF_2$		$HPIMF_3$		$a_8 \times L + b_8 \times H + c_8$
9.	$LPIMF_3$		$HPIMF_3$		$a_9 \times L + b_9 \times H + c_9$

Table 2. The if-then rules and output membership functions

No.	If low pressure is		If high pressure is		The COP is
1.	$LPIMF_1$	and	$HPIMF_1$	then	$0.09796 \times L + 0.08642 \times H - 0.02512$
2.	$LPIMF_2$		$HPIMF_1$		$-0.7031 \times L + 0.3672 \times H + 0.2381$
3.	$LPIMF_3$		$HPIMF_1$		$0.1053 \times L + 0.3493 \times H - 0.2462$
4.	$LPIMF_1$		$HPIMF_2$		$0.06101 \times L - 0.6759 \times H + 0.2887$
5.	$LPIMF_2$		$HPIMF_2$		$-0.4113 \times L + 0.2595 \times H - 0.3855$
6.	$LPIMF_3$		$HPIMF_2$		$-0.09852 \times L + 0.63 \times H - 0.1404$
7.	$LPIMF_1$		$HPIMF_3$		$-0.1456 \times L - 0.03702 \times H - 0.3712$
8.	$LPIMF_2$		$HPIMF_3$		$0.1469 \times L + 0.1681 \times H - 0.3202$
9.	$LPIMF_3$		$HPIMF_3$		$0.6347 \times L + 0.4321 \times H + 0.4061$

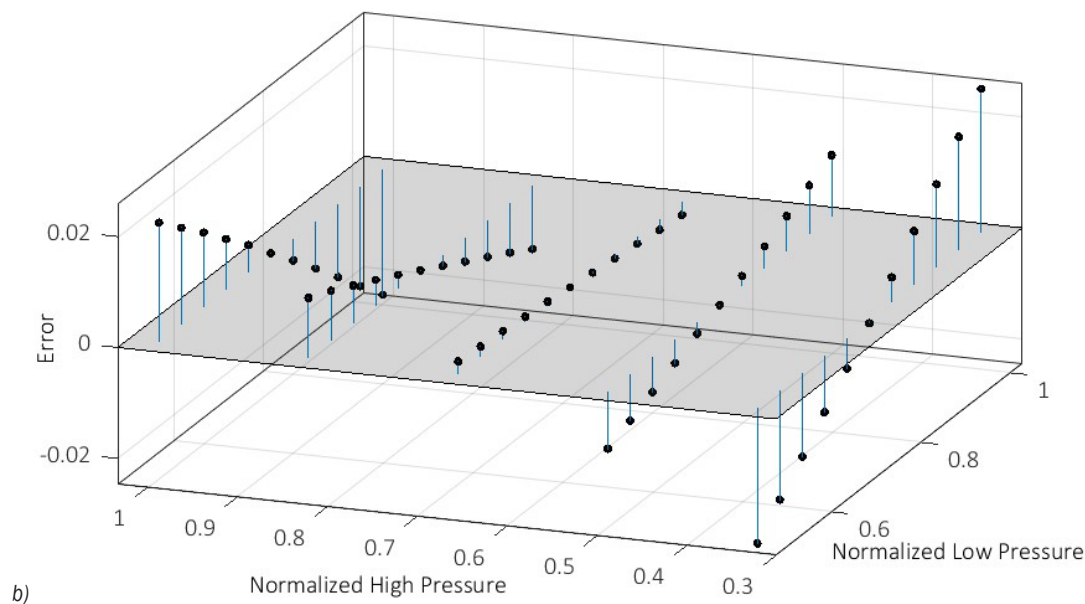
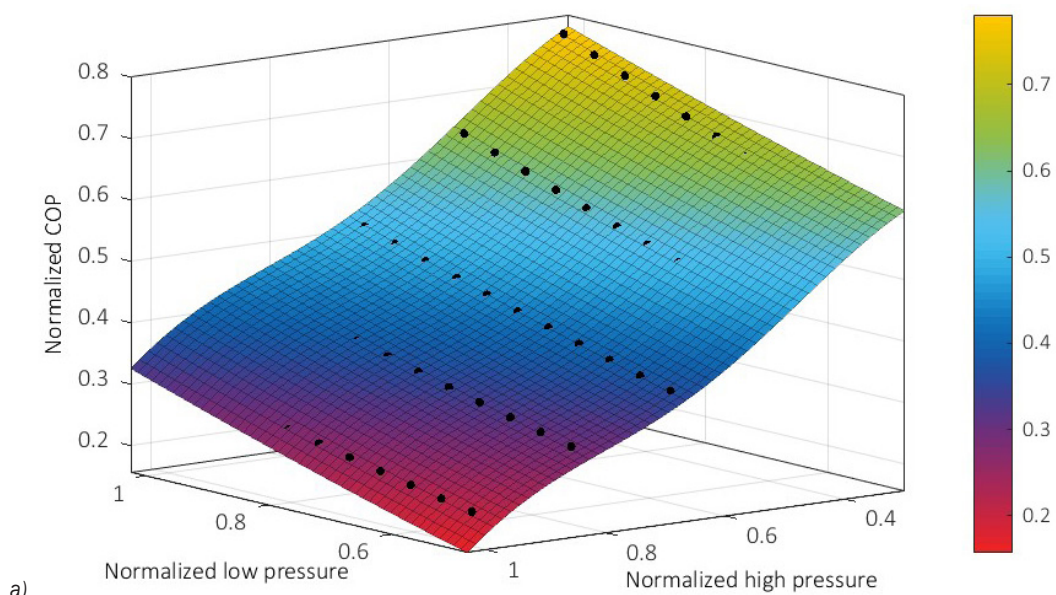


Fig. 6. a) the normalized COP as a function of the normalized input pressures, and b) the residual between the calculated COP and the predicted COP using fuzzy logic

4 COMPARISONS BETWEEN SIMULINK AND FUZZY MODELING RESULTS

Although the proposed approach does not inherently require a dynamic model, the Matlab/Simulink is employed to facilitate the utilization of the developed model for future research endeavours, e.g., implementing control strategies for refrigeration

cycles and to make the developed model easily accessible to other researchers, enabling them to further investigate and contribute to the field of refrigeration systems.

Table 3 presents a comparison between the methods used by Matlab/Simulink and Fuzzy logic modelling to estimate the COP of refrigeration cycles.

Table 3. A simple comparison of the Matlab/Simulink and Fuzzy logic modelling

Matlab/Simulink	Fuzzy logic
Mathematical modelling is employed to express the equations governing the gas refrigeration cycle through block diagrams.	The model is built using the raw data available from the gas refrigeration cycle.
To estimate the COP, complete mathematical models and equations for all sub-domains of a refrigeration system are necessary.	The detailed interaction between sub-systems of a refrigeration system is not necessary for fuzzy modelling. Instead of requiring expertise, a data set can be used to develop the Fuzzy model of the COP.
Classical mathematical programming models rely on well-defined coefficients for all refrigeration cycle components. However, in some cases, model parameters can only be roughly estimated. Additionally, to obtain the COP, all tables must be used.	After developing the fuzzy model of the gas refrigeration cycle, a tuning process is typically carried out to optimize it. Once optimized, the fuzzy model can estimate the COP independently without the need for tables or physical components.
With its graphical user interface (GUI) environment, Matlab/Simulink provides an easier way to simulate gas refrigeration cycles, as well as other engineering systems.	To use fuzzy logic in refrigeration systems, an expert in the field is needed to provide an initial guess of the input/output membership functions and to construct the If-Then rules.

5 CONCLUSIONS

In this research, the COP of gas refrigeration cycles was estimated using both Matlab/Simulink and fuzzy logic approaches. Matlab/Simulink used mathematical equations and relations to estimate the COP, while fuzzy logic used available data sets for the same purpose. The performance of the fuzzy logic approach was evaluated across a wide range of low and high pressures in the cycle. The results showed that fuzzy logic provided a quick way to estimate the COP with less knowledge of gas refrigeration cycles. The fuzzy logic found to be comparable in accuracy to Matlab/Simulink and mathematical modelling with a RMSE of less than 2 %, highlighting the effectiveness of fuzzy logic as a tool to model refrigeration cycles, in particular, and thermodynamics cycles in general.

6 ACKNOWLEDGEMENTS

This paper's research was supported by Yarmouk University, Jordan and Al-Zaytoonah University of Jordan, Jordan.

7 REFERENCE

- [1] Cengel, Y., Boles, M. (2014). *Loose Leaf for Thermodynamics: An Engineering Approach*. McGraw-Hill Education, New York.
- [2] Mohamed, H., Camdali, U., Biyikoglu, A., Aktas, M. (2022). Enhancing the performance of a vapour compression refrigerator system using R134a with a CuO/CeO₂ nano-refrigerant. *Strojniški vestnik - Journal of Mechanical Engineering*, vol. 68, no. 6, p. 395-410, DOI:10.5545/sv-jme.2021.7454.
- [3] Hou, S., Li, H., Zhang, H. (2007). Open air-vapor compression refrigeration system for air conditioning and hot water cooled by cool water. *Energy Conversion and Management*, vol. 48, no. 8, p. 2255-2260, DOI:10.1016/j.enconman.2007.05.005.
- [4] Alamayreh, M.I., Alahmer, A., Bazlamit, S.M., Younes, M.B. (2021). Energy analysis and refrigerant replacement in pre-cooling concrete system in massive concrete structures. *EPPM Conference Proceedings*, p. 14.
- [5] AlAsfar, J., AlShwawra, A., Shaban, N.A., Alrbai, M., Qawasmeh, B.R., Sakhrieh, A., Odeh, O. (2020). Thermodynamic analysis of a biomass-fired lab-scale power plant. *Energy*, vol. 194, p. 116843, DOI:10.1016/j.energy.2019.116843.
- [6] Giannetti, N., Milazzo, A. (2014). Thermodynamic analysis of regenerated air-cycle refrigeration in high and low pressure configuration. *International Journal of Refrigeration*, vol. 40, p. 97-110, DOI:10.1016/j.ijrefrig.2013.11.017.
- [7] Gigiel, A.J., Russell, S.L. (2001). A comparison between air cycle and conventional freezing. *International Institute of Refrigeration Conference Proceedings*, p. 139-144.
- [8] Chen, L., Wu, C., Sun, F. (1999). Finite time thermodynamic optimization or entropy generation minimization of energy systems. *Journal of Non-Equilibrium Thermodynamics*, vol. 24, no. 4, p. 327-359, DOI:10.1515/JNETDY.1999.020.
- [9] Berry, S.R. (1999). *Thermodynamic Optimization of Finite Time Processes*. John Wiley & Sons, Hoboken.

- [10] Kizilkan, Ö. (2011). Thermodynamic analysis of variable speed refrigeration system using artificial neural networks. *Expert Systems with Applications*, vol. 38, no. 9, p. 11686-11692, DOI:10.1016/j.eswa.2011.03.052.
- [11] Balli, S., Sen, F. (2015). Failure prediction of cross-ply laminated double-serial mechanically fastened composites using fuzzy expert system. *Strojniški vestnik - Journal of Mechanical Engineering*, vol. 61, no. 2, p. 123-130, DOI:10.5545/sv-jme.2014.1909.
- [12] Devedžić, G., Manić, M., Tanikić, D., Ivanović, L., Mirić, N. (2010). Conceptual framework for NPN logic based decision analysis. *Strojniški vestnik - Journal of Mechanical Engineering*, vol. 56, no. 6, p. 402-408.
- [13] Sahin, A.S. (2011). Performance analysis of single-stage refrigeration system with internal heat exchanger using neural network and neuro-fuzzy. *Renewable Energy*, vol. 36, no. 10, p. 2747-2752, DOI:10.1016/j.renene.2011.03.009.
- [14] Kalogirou, S.A. (2001). Artificial neural networks in renewable energy systems applications: a review. *Renewable and Sustainable Energy Reviews*, vol. 5, no. 4, p. 373-401, DOI:10.1016/S1364-0321(01)00006-5.
- [15] Milecki, A., Rybarczyk, D. (2015). Modelling of an electrohydraulic proportional valve with a synchronous motor. *Strojniški vestnik - Journal of Mechanical Engineering*, vol. 61, no. 9, p. 517-522, DOI:10.5545/sv-jme.2015.2553.
- [16] AlSakarneh, A. (2011). Optimum fuzzy model for single input single output data system. *Control and Intelligent Systems*, vol. 39, p. 41.

Research on an Analytical Method for the Forming Force of External Spline Cold Roll-Beating

Qun Ma* – Xiangwei Zhang

Xi'an Technological University, School of Ordnance Science and Technology, China

To determine the force and energy parameters of cold roll-beating of external splines, the characteristics of the deformation zone in cold roll-beating are analysed. The geometric dimensions and position of the deformation zone change with the movement of the roller, the contact arc, and the reduction are very small, and there is an incomplete deformation zone in the initial stage of cold roll-beating. A discrete analytical method for calculating the unit pressure and deformation force is proposed, and the cold roll-beating process is discretized into an infinite number of cold-rolling processes with complex sections. The discrete analytical model of unit pressure and deformation force is established, and the unit pressure value and its distribution characteristics are determined. To verify the discrete analytical model, a finite element model of cold roll-beating is established, and the forming force is calculated. A horizontal milling machine is modified to carry out the cold roll-beating experiment, and the forming force is measured. The predicted results of the discrete analytical model are compared with the simulation and experiment results. The results show that the maximum error of radial force compared with the simulation and experiment results is about 7 % and 4 % respectively, and the variation curve of radial force is basically consistent, but the time of a cold roll-beating process is slightly shorter. The discrete analytical model correctly predicts the magnitude and change process of cold roll-beating forming force.

Keywords: discrete analytical method, cold roll-beating, forming force, deformation zone, radial force

Highlights

- The changing characteristics of the metal deformation zone of external spline cold roll-beating are defined.
- A discrete analytical model for calculating the forming force of cold roll-beating is established by using the principal stress method.
- The finite element simulation of the cold roll-beating is carried out, the deformation of the workpiece is presented, and the forming force of the cold roll-beating is calculated.
- The cold roll-beating forming force is measured via experiment, and the discrete analytical model is verified. The results show that the discrete analytical model correctly predicts the magnitude and the change process of cold roll-beating forming force.

0 INTRODUCTION

The cold roll-beating of external splines is a non-cutting manufacturing technology in which a pair of rollers with the same profile and the tooth space shape of the workpiece continuously strike the workpiece to produce plastic deformation to form a defined tooth shape. This kind of processing technology aiming at net or near net forming has been rapidly developed and plays an important role in industry. The processing efficiency of cold-rolling splines is very high, and it is widely used in the automobile and agricultural machinery industries.

The cold roll-beating process of splines is a discontinuous and progressive local deformation process, so the deformation mechanism is complex, and the theoretical analysis and parameter calculation are difficult. The research on this kind of problem is mainly carried out by experiments or finite element simulations.

Wu et al. [1] and Liu et al. [2] analysed the gear cold-rolling process with the finite element method and carried out experimental verification. Ma et al. [3]

analysed the gear roll-forming process with the finite element method and calculated the forming force. Fu et al. [4] used DEFORM-3D software to study the local induction heating rolling method, which is used to manufacture large gears. Zhang et al. [5] Quan et al. [6] and Wang et al. [7] used ABAQUS and ANSYS to conduct numerical simulations of the spline cold roll-beating process and calculate the deformation force of cold rolling. Wang et al. [8] established the finite element model for deformation prediction of the split straight bevel gear, and the results of finite element calculation were in good agreement with the experimental results. Yuan et al. [9] used ABAQUS to conduct finite element simulations of racks' cold roll-beating deformation force and then analysed the influence of materials, cold roll-beating speed, and cold roll-beating mode on the deformation force through experiments. However, the finite element analyses (FEA) of the complex profile rolling required a long central processing unit (CPU) time and large storage space. For example, a typical CPU time for the 3D FEA of gear rolling with a flat die was about one week, using DEFORM code in 2007 [10].

The analytical model (e.g., modelled by the principal stress method or slip-line field method (SLFM)) has a clear physical interpretation and with shorter computation time. Zhang et al. [11] developed and improved the slip line field (SLF) and the analytical models of rolling force. Li et al. [12] and Li et al. [13] established the slip line field of external spline rolling forming and calculated the unit pressure and rolling pressure. Zhang et al. [14] developed an SLFM model with different friction models to analyse the spline cold-rolling process. Quagliato and Berti [15] established a slip line model for force estimation in the radial-axial ring rolling process. Then, the SLFM model was perfected to include axial force, by which experimental and numerical verifications were carried out [16]. Ma et al. [17] proposed an analytical model for predicting the pitch error of gear rolling with consideration of geometric relations and process parameters.

Although the above research has greatly improved the efficiency, the analytical model for the special forming process of external spline cold roll-beating has not been studied. At present, there is no analytical model, empirical formula, or chart for calculating the unit pressure and deformation force of external spline cold roll-beating.

In this paper, the characteristics of the cold roll-beating deformation zone are analysed, and the discrete analytical method for calculating the forming force is given. A cold roll-beating process is discretized into an infinite number of cold-rolling processes, and the unit pressure and deformation force of each cold-rolling process are calculated to determine the deformation force variation curve of a cold roll-beating process. Finally, the correctness of the discrete analytical method is verified via finite element simulation and cold roll-beating experiment.

1 FORMING PRINCIPLE OF EXTERNAL SPLINE COLD ROLL-BEATING

The tooth shape of an external spline is distinct, as is the cold roll-beating process. The involute spline is generally formed by continuous indexing, while the rectangular spline and triangle spline are formed by intermittent indexing.

Fig. 1 shows the principle of involute spline cold roll-beating. The cold roll-beating of an involute spline is carried out by continuous indexing at normal temperature. Two rollers rotate synchronously and reversely at high speed, and the angular velocity is ω_g . The rollers beat the workpiece once every revolution. The workpiece rotates continuously with the angular

velocity ω_p and feeds along the axis with the velocity v . During the contact time with the workpiece, two rollers rotate along their own rotation axis under the action of friction, and the angular velocity is ω_r . The transmission system of the machine tool strictly ensures that the ratio of ω_g to ω_p is the number of spline teeth so as to process the involute keyway, which is consistent with the profile of the roller section.

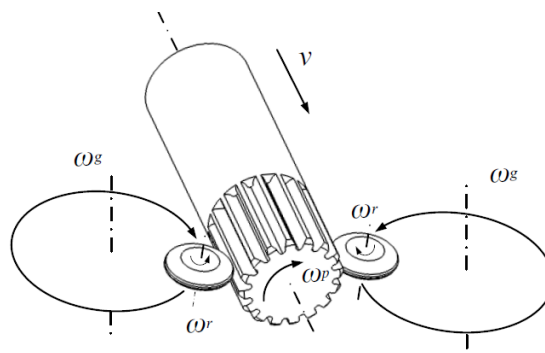


Fig. 1. Schematic diagram of cold roll-beating of involute spline

2 CHARACTERISTICS OF THE METAL DEFORMATION ZONE OF COLD ROLL-BEATING

In this paper, a cold roll-beating process is defined as the process of the roller from contacting the workpiece to leaving the workpiece in a rotation cycle. In a cold roll-beating process, the rotation speed and feed speed of the workpiece are far less than the rotation speed of the rollers, and the contact time between the rollers and the workpiece is very short (several milliseconds); it can be approximately considered that the workpiece is stationary when the rollers beat it.

The cold roll-beating is similar to a metal rolling process, and the research on metal rolling theory is more developed, which can provide theoretical guidance for the calculation of the forming force of cold roll-beating. However, the cold roll-beating is different from the general metal rolling process, as the location and parameters of the metal deformation zone are changing constantly.

Fig. 2 shows the variation of the metal deformation zone. O is the rotation centre of the roller. R is the radius of rotation of the roller axis. r is the radius of the roller. h_f is the rolling depth. Arc DE and $D'E'$ are the profile curves of the section formed by two cold roll-beating processes on the same tooth space. P is the axial feed rate of the workpiece per revolution.

It can be seen from Fig. 2a that the position of the deformation zone is not fixed but moves continuously with the roller. When the roller is at B_1 , the contact arc, bite angle and reduction are arc A_1B_1 , α_1 and Δh_1 . When the roller moves to B_i , the contact arc, bite angle and reduction change to arc A_iB_i , α_i and Δh_i . When the roller moves to the other position on the arc $D'E'$, all of the above deformation zone parameters are different. Considering the profile shape of the roller, the average width of the deformation zone at different positions on the arc $D'E'$ is also different. According to the geometric relationship in Fig. 2a, when the spline modulus is small, the contact arc length and the reduction are also small relative to the workpiece thickness.

It can be seen from Fig. 2b that D' is not the starting point of the cold-rolling process. When the roller is at B on the extension line of arc $D'E'$, the cold-rolling process begins, but the deformation zone is not complete at this time. The theoretical contact arc, bite angle and reduction are arc AB , α and Δh . Due to the missing part, the actual deformation zone parameters are arc AB' , α' and $\Delta h'$. However, the duration of the incomplete deformation zone is very short. The length of the contact arc, the bite angle and the reduction increase rapidly and reach the maximum when the roller moves to D' , then decrease slowly and decrease to 0 at E' .

Therefore, there are three main characteristics of a cold roll-beating metal deformation zone. First, the location and parameters of the deformation zone are constantly changing; Second, there is an incomplete

deformation zone in the initial stage of cold rolling; Third, the contact arc and the reduction are both small.

In the process of metal deformation, it is impossible to calculate the forming force directly by the principal stress method with the change in the geometric size of the deformation zone.

3 ESTABLISHMENT OF THE DISCRETE ANALYTICAL MODEL

A cold roll-beating process is different from a metal rolling process, but it is similar when the rollers only rotate along their own rotation axis ($\omega_g = 0$). The periodic rotation of the roller only changes the position and geometric parameters of the deformation zone.

As shown in Fig. 2a, when the roller is located at B_1 , assuming that $\omega_g = 0$ and $\omega_r > 0$, the cold roll-beating process can be approximately regarded as the cold-rolling process of the workpiece along the direction of $C'C$ in the following time, in which the workpiece is rolled in at A_1 and rolled out at B_1 , and the rolling speed is expressed as

$$V_1 = r \omega_{r1}, \tag{1}$$

When the roller moves to point B_i , the cold roll-beating process can also be approximately regarded as a cold-rolling process from A_i to B_i , and the rolling speed is expressed as

$$V_i = r \omega_{ri}, \tag{2}$$

Because the rotation angular velocity of the roller is constant at any time, $V_1 = V_i$.

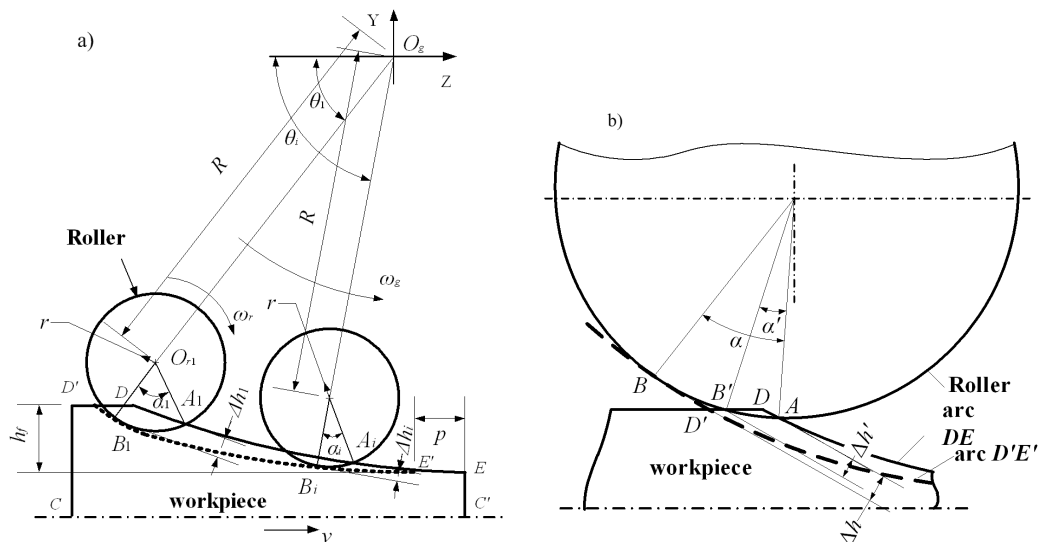


Fig. 2. The change of metal deformation zone in cold rolling; a) complete deformation zone; and b) incomplete deformation zone

Since there is no other external force in the cold-rolling process, a cold roll-beating process can be discretized into an infinite number of tension-free cold-rolling processes of a complex cross-section with the same rolling speed.

Fig. 3 shows the force condition of any differential unit in the metal deformation zone. Firstly, it is very important to determine the direction of friction t_z , which determines the type of deformation zone. The 3D solid model of the workpiece and the roller was established by using the Solidworks 3D design software, and it was imported into the pre-processing program of the finite element software DEFORM-3D. The rotation speed of the roller is set to 209 rad/s, and the radius of rotation is 90 mm. To simulate the forming force in a cold roll-beating process, the contour formed by the last cold roll-beating is directly established on the workpiece, as shown in Fig. 4.

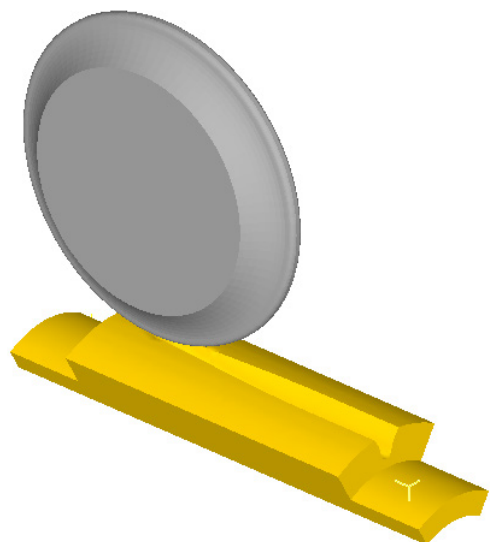


Fig. 4. The finite element model of cold rolling

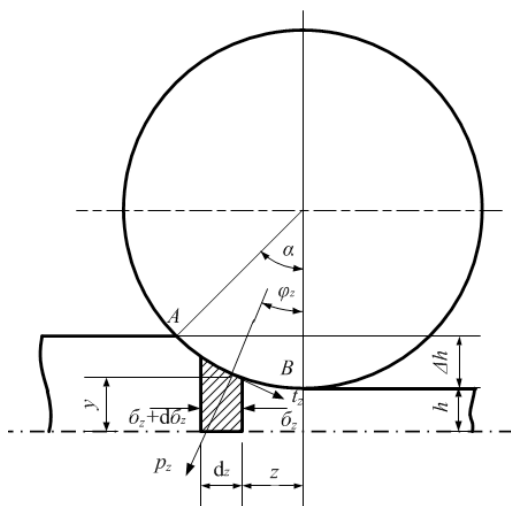


Fig. 3. Force condition of any differential unit in deformation zone of workpiece

Observe the velocity nephogram of metal particles, as shown in Fig. 5. The finite element analysis shows that at any time of cold roll-beating, the metal flow velocity in the deformation area is less than the linear velocity of the roller, so the whole deformation area belongs to the backward slip zone, and the direction of friction on the contact arc is opposite to the linear velocity of the roller.

As shown in Fig. 3, if the elastic deformation of the roller and the workpiece is neglected, the sum of the components of the force acting on the differential unit along the Z direction is expressed as

$$p_z \sin \varphi_z \frac{dz}{\cos \varphi_z} + \sigma_z y - t_z \cos \frac{dz}{\cos \varphi_z} - (\sigma_z - d\sigma_z)(y + dy), \tag{3}$$

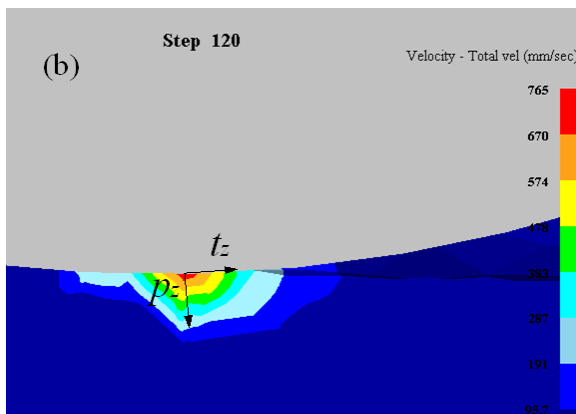
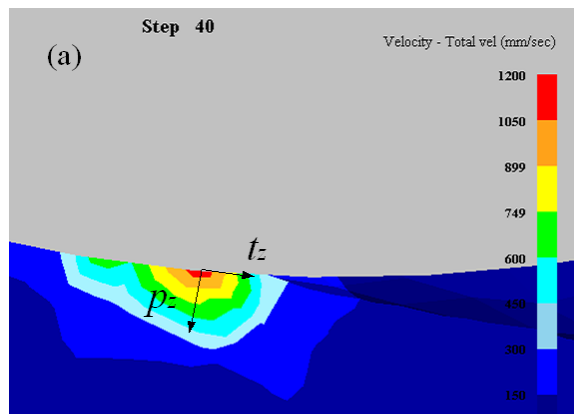


Fig. 5. Velocity nephogram of metal particles at a) step 40, and b) steep 120; in [mm/s]

where p_z is the unit pressure of the roller on the workpiece, and T_z is the unit friction force between the roller and workpiece. If z and y are the coordinates of the contact arc, then $\tan(\varphi_z) = dy/dz$, which can be substituted into Eq. (3), and the Kalman differential equation for calculating the average unit pressure is obtained, expressed as

$$\frac{dp_z}{dz} - \frac{K}{y} \frac{dy}{dz} - \frac{t_z}{y} = 0, \quad (4)$$

where K is determined by the plastic equation under plane deformation, expressed as

$$K = \sigma_1 - \sigma_3 = \frac{2}{\sqrt{3}} \sigma, \quad (5)$$

where σ_ϕ is the actual deformation resistance of the metal.

Assuming that the contact friction condition in the deformation zone obeys the dry friction law, i.e., $t_z = fp_z$, where f is the friction coefficient on the contact arc, the solution of the differential Eq. (4) is as follows

$$p_z = e^{\int \frac{f}{y} dz} \left(C + \int \frac{K}{y} e^{-\int \frac{f}{y} dz} dy \right), \quad (6)$$

where C is integral constant determined by boundary conditions.

Since the difference between the contact arc and the chord connecting the roll-in point and the roll-out point is very small, the contact arc can be approximated to a chord as

$$dz = \frac{l_a}{\Delta h} dy, \quad (7)$$

where l_a is the length of chord AB .

Substitute Eq. (7) into Eq. (6) and integrate them, and determine the integral constant according to the tension-free boundary condition. Finally, the distribution formula of unit pressure is obtained as

$$p_z = \frac{K}{\delta} \left[(\delta - 1) \left(\frac{h + \Delta h}{y} \right)^\delta + 1 \right]. \quad (8)$$

Here, $\delta = \frac{l_a f}{\Delta h}$, and h is half of the thickness of the workpiece at the rolling point.

If the workpiece is an involute spline with $Z=20$ and $m=2$ mm, the cold roll-beating parameters are $p=1$ mm, $r=20$ mm, $R=90$ mm, and the friction coefficient on the contact arc is $f=0.17$. After the deformation zone parameters such as h and l_a are determined from Fig. 2, the unit pressure on the contact arc and its distribution along the Y direction can be determined by Eq. (8).

Fig. 6 shows the distribution of unit pressure along Y direction on the contact arc in a single cold-rolling process. It can be seen that the distribution of unit pressure is not uniform. As the roller moves towards point E' (Δh becomes smaller), the unit pressure on the contact arc decreases, which is due to the decrease of the reduction and the length of the contact arc. The unit pressure on the contact arc is small in the whole cold roll-beating process because the length and reduction of the contact arc are very small.

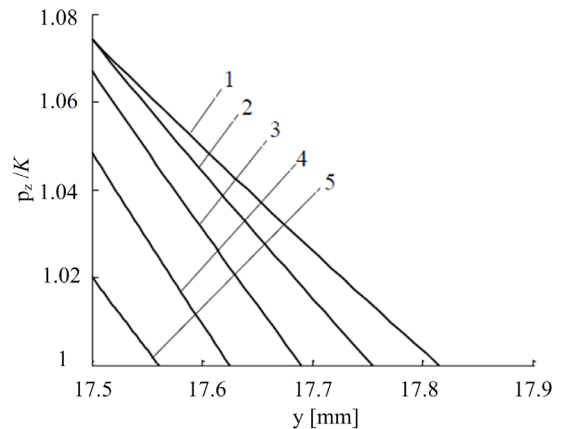


Fig. 6. Distribution of unit pressure on contact arc: 1 $\Delta h = 0.31$ mm; 2 $\Delta h = 0.25$ mm; 3 $\Delta h = 0.19$ mm; 4 $\Delta h = 0.12$ mm; 5 $\Delta h = 0.06$ mm

The unit pressure in the incomplete deformation zone should be calculated according to the parameters of the theoretical deformation zone. Although incomplete, the force condition of any differential unit in the deformation area is still as shown in Fig. 3.

According to the unit pressure obtained with Eq. (8), the deformation force of each cold-rolling process is calculated, so as to determine the deformation force and its changes during one cold roll-beating process.

The deformation force in each cold-rolling process can be decomposed into radial force and tangential force (i.e., the component of the deformation force along Y and Z directions).

It can be seen from Fig. 3 that the radial force can be determined by the following equation as

$$F_y = \bar{b} \cos \alpha \cdot n_\sigma \int_{Z_B}^{Z_A} p_z \frac{dz}{\cos \varphi_z} \cos \varphi_z + \bar{b} \sin \alpha \cdot n_\sigma \int_{Z_B}^{Z_A} t_z \frac{dz}{\cos \varphi_z} \sin \varphi_z, \quad (9)$$

where, \bar{b} is the average width of the deformation zone, n_σ is the stress state coefficient, Z_A and Z_B are the Z-axis coordinates of points A and B in Fig. 3.

Since $\tan(\varphi_z) = dy/dz$ and $t_z = fp_z$, then

$$F_y = \bar{b}n_\sigma \int_{Z_B}^{Z_A} (p_z \cos \alpha \cdot dz + fp_z \sin \alpha \cdot dy). \quad (10)$$

Substitute Eqs. (5), (7) and (8) into Eq. (10), and the radial force can be expressed as

$$F_y = \bar{b}n_\sigma \cdot \frac{2\sigma_\varphi}{\sqrt{3}\delta} \left\{ \int_h^{h+\Delta h} \left(\frac{l_a}{\Delta h} \cdot \cos \alpha + f \sin \alpha \right) \cdot \left[(\delta - 1) \left(\frac{h + \Delta h}{y} \right)^\delta + 1 \right] dy \right\}. \quad (11)$$

After the integration, we can obtain the following equation as

$$F_y = \bar{b}n_\sigma \cdot \frac{2\sigma_\varphi}{\sqrt{3}\delta} \left(\frac{l_a}{\Delta h} \cdot \cos \alpha + f \sin \alpha \right) \cdot \left[h \left(\frac{h + \Delta h}{y} \right)^\delta - h \right]. \quad (12)$$

The analytical formula of tangential force can also be deduced as

$$F_z = \bar{b}n_\sigma \cdot \frac{2\sigma_\varphi}{\sqrt{3}\delta} \left(\cos \alpha - \frac{l_a}{\Delta h} \cdot f \sin \alpha \right) \cdot \left[h \left(\frac{h + \Delta h}{y} \right)^\delta - h \right]. \quad (13)$$

Therefore, the parameters of \bar{b} , n_σ and σ_φ must be determined when calculating the deformation forces.

4 DETERMINATION OF THE PARAMETERS

4.1 Determination of Average Width of the Deformation Zone

Considering the symmetry of the profile of the roller, the total pressure on the roller should point to the axis of the roller. Therefore, in the calculation, the width of the deformation zone \bar{b} is taken as the width of the projection area along the total pressure direction of the actual deformation zone, so it is determined by the geometric relationship shown in Fig. 2a and the profile curve of the roller.

4.2 Determination of Stress State Coefficient n_σ

The stress state coefficient is affected by the size of the roller, external friction, external zone metal and tension, and can be expressed as

$$n_\sigma = n_\beta n'_\sigma n''_\sigma n'''_\sigma, \quad (14)$$

where n_β is the stress state coefficient considering the influence of workpiece width, n'_σ is the influence coefficient of external friction, n''_σ is the external zone influence coefficient, n'''_σ is the tension influence coefficient.

A cold roll-beating process is regarded as an infinite number of cold-rolling processes, while for small module spline, if the friction coefficient on contact arc is constant, the influence of n_β , n'_σ and n''_σ can be ignored.

Since the length of contact arc and the reduction are very small, which is similar to thick workpiece rolling, considering the influence of the external zone on the average unit pressure, the external zone influence coefficient can be expressed as

$$n'''_\sigma = \left(\frac{l_a}{h} \right)^{0.4}. \quad (15)$$

4.3 Determination of Actual Deformation Resistance of Metal

The actual deformation resistance is affected by the nature of metal, temperature, deformation degree and deformation speed. Several scholars [18] to [21] have studied the mathematical models of deformation resistance of various alloys in accordance with the characteristics of Chinese materials, which can be used to calculate the deformation force of cold roll-beating.

Studies show that the effect of strain rate on deformation resistance is relatively small at low temperature [18] and [19], so the effect of deformation rate is not considered in the calculation.

5 VERIFICATION OF THE DISCRETE ANALYTICAL MODEL

The accuracy of the discrete analytical method is verified by the finite element method and the experimental results. Because the effect of workpiece indexing is very small, the cold roll-beating forming force of rack is measured in the experiment.

5.1 Design of the Roller

It is more complicated to make the roller strictly according to the involute tooth profile, and the tooth shape does not affect the verification. To reduce the experimental cost, the roller with the tooth profile size as shown in Fig. 7 is made, and the maximum outer circle radius is $R = 24$ mm. To conform to the cold roll-beating process of rack, the roller is designed with three tooth profiles. After cold roll-beating, two complete teeth and three tooth spaces are formed on the workpiece.

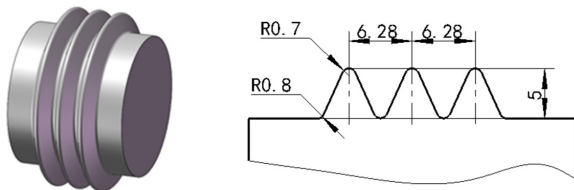


Fig. 7. a) 3D model of the roller, and b) its profile size

5.2 Establishment of Finite Element Model

In this paper, the discrete analytical model is used to calculate the forming force of a single tooth roller. Although the roller shown in Fig. 7 has three teeth, the parameters of the three deformation regions are the same, so the results of the discrete analytical model can be expanded three times to compare with the experimental results.

Consistent with the discrete analytical model, the roller is also modelled according to the shape of a single tooth, but the tooth shape is modified to the size shown in Fig. 7, and the tooth groove size on the workpiece is also modified accordingly. Import the 3D models into DEFORM-3D preprocessor, and the symmetry plane of the tooth groove is $X = 0$, as shown in Fig. 8.

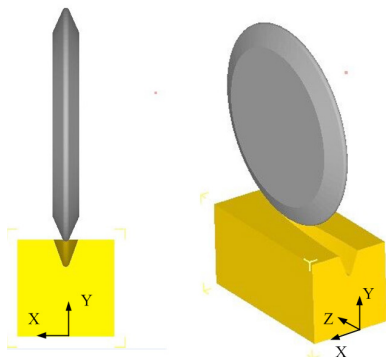


Fig. 8. The finite element models of the roller and workpiece

5.3 Reformation of Experimental Equipment

In this paper, a horizontal milling machine is reformed, and the roller is installed on the spindle, as shown in Fig. 9. The spindle motor power is 7.5 kW, the spindle speed is 30 r/min to 1500 r/min, and the feed motor power is 1.5 kW. The radial and tangential forces of cold roll-beating are measured with a PCB261A03 tri-axial forces sensor, which is produced by PCB Piezotronics INC in the United States.

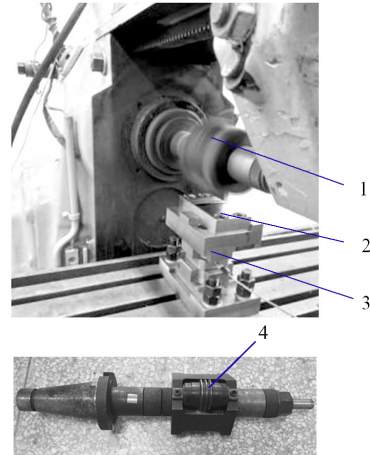


Fig. 9. Cold roll-beating experimental equipment; 1 machine tool spindle, 2 workpiece, 3 triaxial forces sensor, and 4 the roller

5.4 Selection of Workpiece Material

The difference of materials only affects the actual deformation resistance of metals but does not affect the verification of the discrete analytical model. Because the horizontal milling machine is not specifically defined as cold roll-beating equipment, the stability and the power are insufficient, so the workpiece material is selected as copper with good ductility and small deformation resistance.

6 RESULTS AND DISCUSSION

6.1 Measurement of Cold Roll-Beating Forming Force

If the cold roll-beating process with the feed of 2 mm/r is tested, the nearest speed should be selected according to the speed ratio of the horizontal milling machine gearbox, and it should also meet the load requirements of the motor. The experimental parameters are as follows: the cold roll-beating depth is 2.5 mm, the roller rotation speed is 25.13 rad/s (240 r/min), and the workpiece feed speed is

476 mm/min (feed rate 1.983 mm/r). Samples formed by cold roll-beating are shown in Fig. 10.

Change curves of radial and tangential forces measured in the experiment are shown in Fig. 11. As shown in Fig. 11a, the radial force increases continuously in the beat-in stage and remains constant in the stable stage (about 31.8 kN) and decreases continuously in the beat-out stage. As shown in Fig. 11b, the maximum tangential force is only about 2 kN, which is about 6.3 % of the maximum radial force.

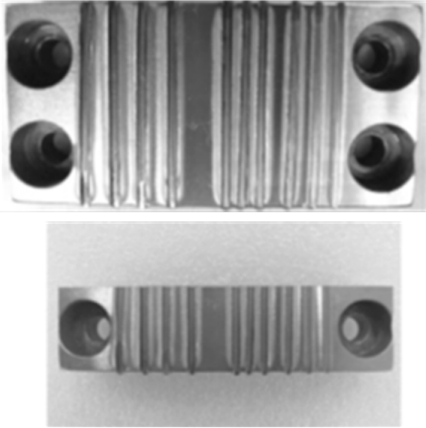


Fig. 10. Samples formed by cold roll-beating

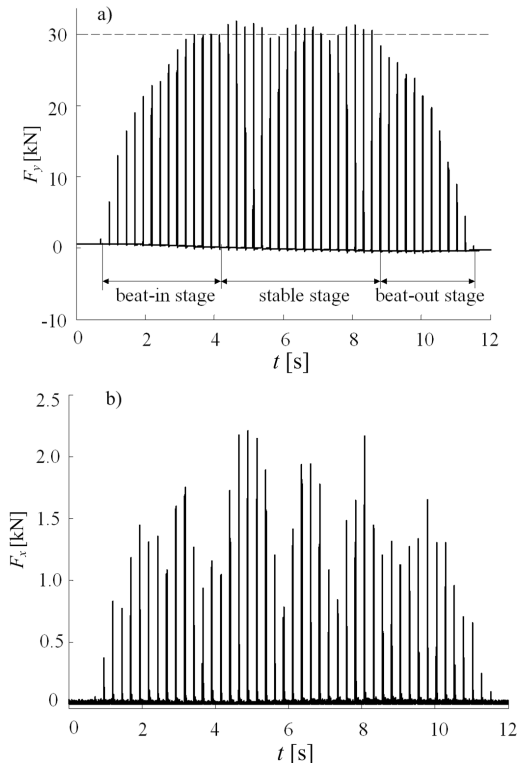


Fig. 11. Cold roll-beating forming forces measured in the experiment; a) the radial force; b) the tangential force

6.2 Finite Element Simulation of Cold Roll-Beating

6.2.1 Preprocessing of Finite Element Models

The parameters in the DEFORM-3D preprocessor are set as follows:

1. Without considering the influence of deformation of the roller, the roller is considered as a rigid body, the workpiece is considered as a plastic body. The material of workpiece is set to BRASS-CDA-110 in the DEFORM-3D material library, and is considered with a constant property in room temperature (20 °C);
2. A ring region with thickness of 5 mm of workpiece is refined with density ratio of 2, as shown in Fig. 12;

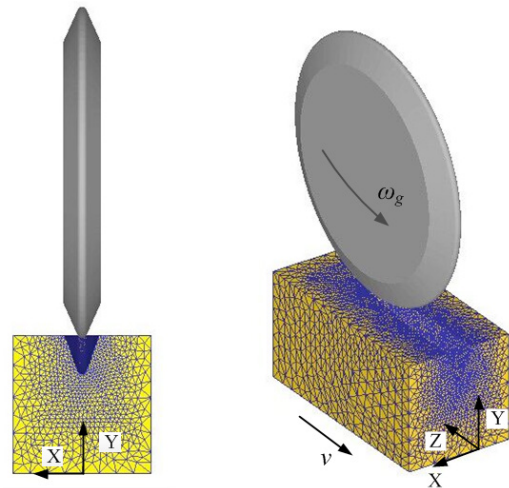


Fig. 12. Preprocessing of finite element models

3. The element number is 39192, and minimum element size is about 0.6574 mm;
4. Without considering the rotation of the roller, the roller rotates around the spindle with an angular velocity of 25.13 rad/s, and the feed speed of the workpiece is 476 mm/min (feed rate 1.983 mm/r);
5. In the process of cold roll-beating, it can be considered as pure rolling between the roller and the workpiece. To simplify the calculation, the friction coefficient between the roller and the workpiece is set to 0;
6. The target volume option is set to active in FEM + meshing.

6.2.2 Finite Element Simulation Results

In the DEFORM-3D postprocessor, the distribution of the effective stress and the contact state are

given, as shown in Fig. 13, where the green nodes represent the contact nodes. The distribution area of the effective stress and contact nodes moves with the roller, indicating that the position of the deformation zone is also moving constantly. The distribution area of contact nodes and the variation of stress are increasing and then decreasing, which indicates that the parameters of metal deformation zone are also changing. The results in Fig. 13 validate the analysis of the characteristics of the deformation zone of cold roll-beating in this paper.

Fig. 14a shows the deformation of the tooth groove. Compared with previous deformation, the width of the tooth groove significantly increases, and the increments along the workpiece feed direction (Z direction) also show a trend of increasing and then decreasing, which indicates the trend of variation in the width of the deformation zone. Fig. 14b shows the variation curves of forming force; it can be seen that the maximum radial force is about 10.9 kN, while the maximum tangential force is about 0.8 kN, which is about 7.3 % of the maximum radial force,

which is basically consistent with the experimental measurement results. The reason that the tangential force is very small is that the deformation on both sides of the tooth groove is distributed symmetrically along the centre of the tooth groove, as shown in Fig. 14a. Therefore, the tangential force on both sides of the tooth groove is equal in magnitude and opposite in direction.

6.3 Comparison of Cold Roll-Beating Forming Force

Since the radial force of cold roll-beating is much larger than the tangential force, only the radial force is considered when calculating the forming force with the discrete analytical model. At the stable stage in Fig. 11, the radial force variation curve of a cold roll-beating process is obtained and compared with the discrete analytical model calculation results and the finite element simulation results, as shown in Fig. 15. In the experiment, the roller contains three teeth, so the calculation results and simulation results are expanded by three times for comparison.

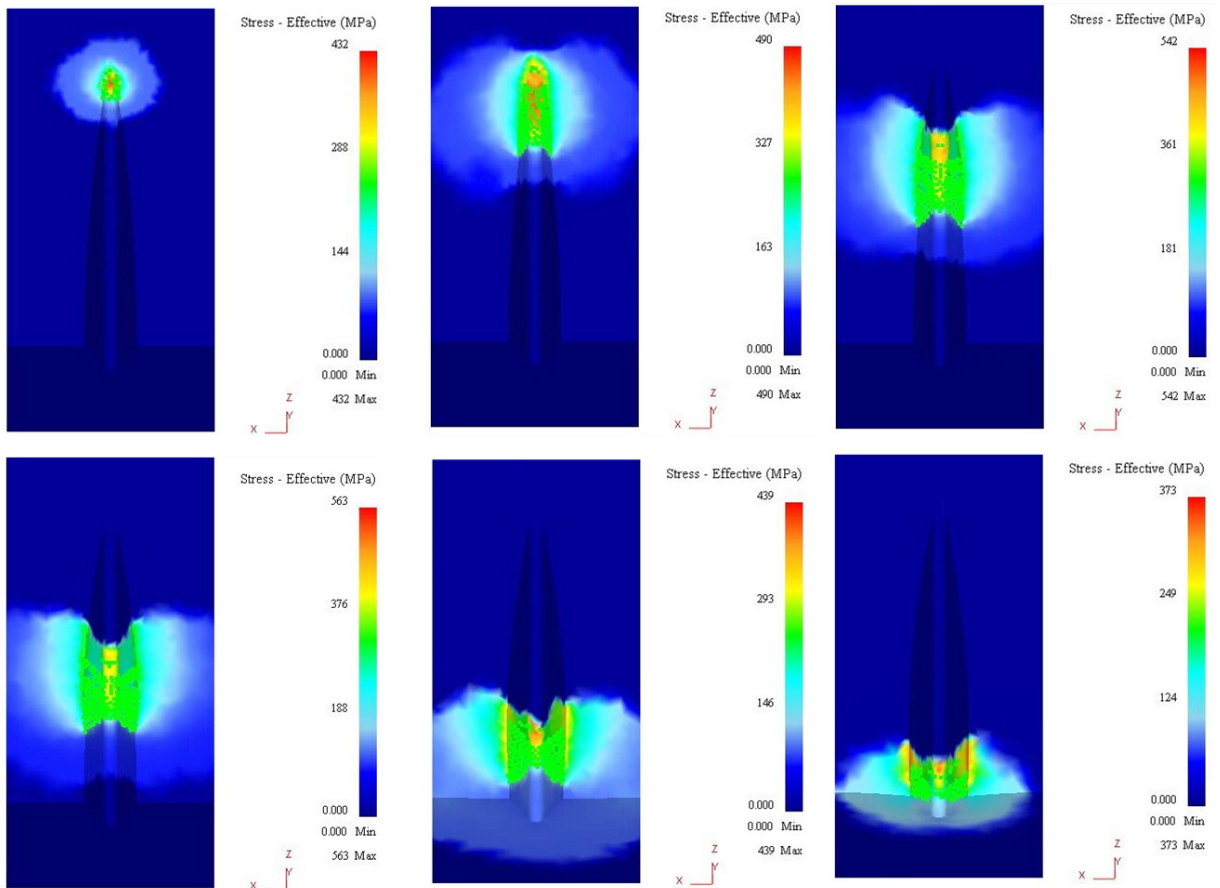


Fig. 13. Effective stress distribution and contact state on the workpiece

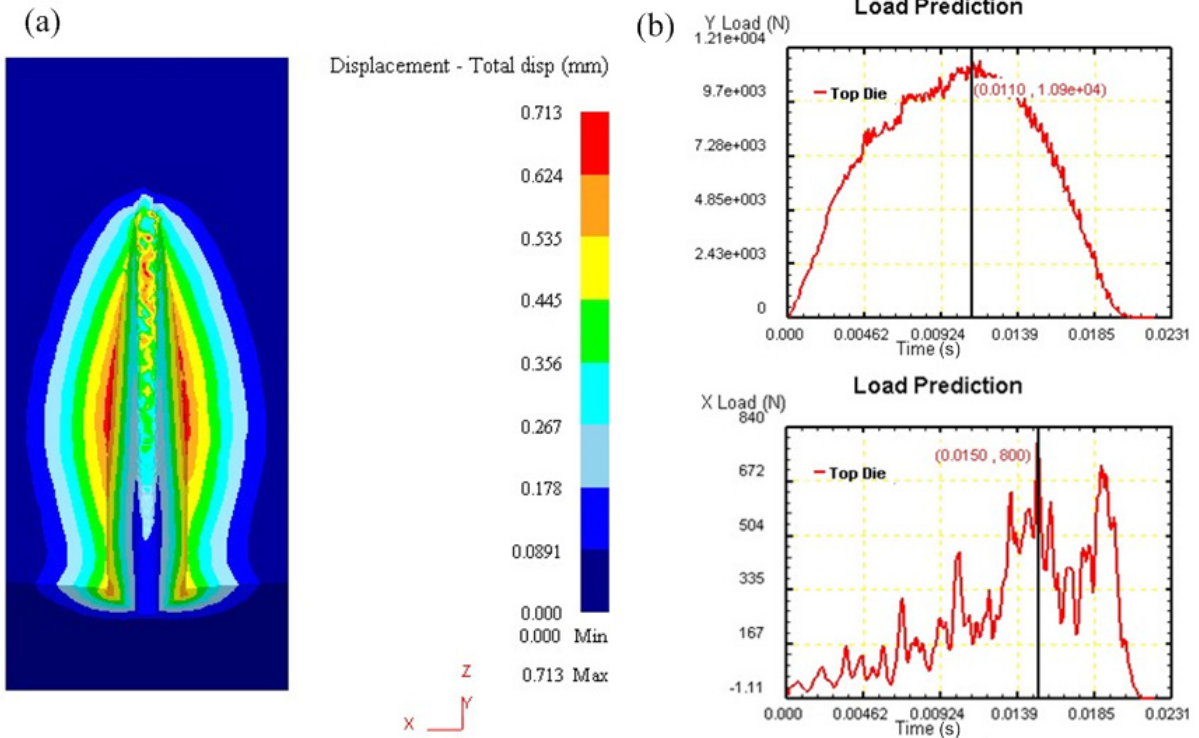


Fig. 14. Deformation of the tooth groove and the forming force

It can be seen from Fig. 15 that the maximum value of radial force predicted by the discrete analytical model is 30.5 kN, which is about 2.2 kN different from the simulation results (about 32.7 kN) with an error of 7 %, and only about 1.3 kN different from the experimental measurement results at the stable stage (about 31.8 kN) with an error of 4 %.

The change trend of radial force predicted by the discrete analytical model is approximately the same as that of simulation and experimental results, but there is an error when the maximum radial force is reached.

The duration of cold roll-beating process predicted by the discrete analytical model is in good agreement with the simulation results but significantly less than the experimental results.

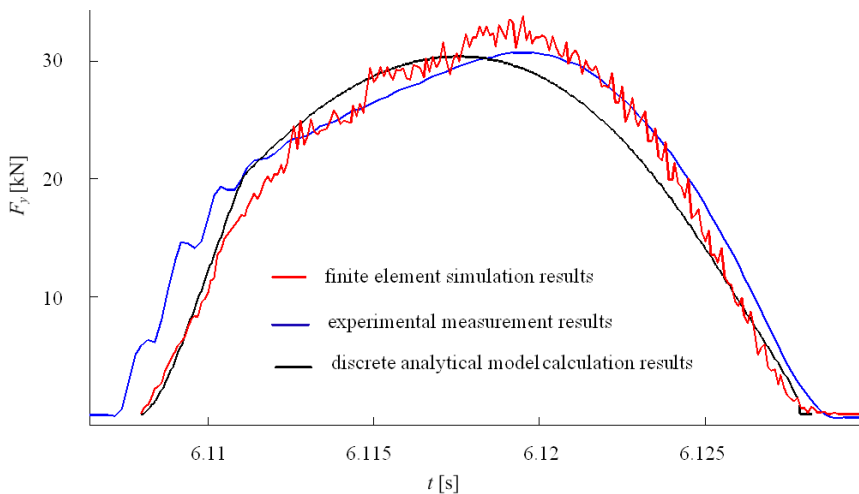


Fig. 15. Comparison of cold roll-beating radial force calculated by different methods

6.4 Reasons for the Longer Duration of Cold Roll-Beating Measured in Experiment

The action process of the roller on the workpiece is similar to the plastic problem of the wedge or cylinder sliding over the smooth surface. Research on this kind of problem has shown that the slip line field in the metal deformation zone should be as shown in Fig. 16 (V_r is the instantaneous linear velocity of the roller) [22] to [24]. As the cold roll-beating progresses, the friction coefficient increases [25], and the metal bulge in front of the roller, so the time of cold roll-beating is longer.

Similar results can be seen in the finite element simulation. The workpiece is cut by $X = 0$ plane, and the deformation of the metal at the bottom of the groove is obtained, as shown in Fig. 17. The metal bulge in front of the roller is obvious, and a protrusion is formed on the beat-out face, and a collapse is formed on the surface. Since the tooth groove formed by the last cold roll-beating has been established on the 3D model of the workpiece, the protrusion and the collapse are not obvious after simulation, and the duration of cold roll-beating process is not increased.

However, in the experiment, the tooth groove is formed after multiple cold roll-beating, so the protrusion is more obvious, and the duration is longer.

At the same time, the elastic recovery of metal, the insufficient stiffness and the lack of power of machine tools will also increase the time of cold roll-beating.

Although there is some error in the time of cold roll-beating process calculated by the discrete analytical method, it does not affect the determination of cold roll-beating force and energy parameters. Cutting fluid is used in cold roll-beating, and the adhesion of metal can be controlled, and the stability and power of the special cold roll-beating machine tools are more appropriate, so the theoretical value will be closer to the true value.

6.5 Prospects for Future Research

Although the discrete analytical model can predict the cold roll-beating forming force quickly and accurately, it cannot do so with some factors, such as the elastic deformation of the roller, the bulge and collapse of the metal material. The finite element simulation

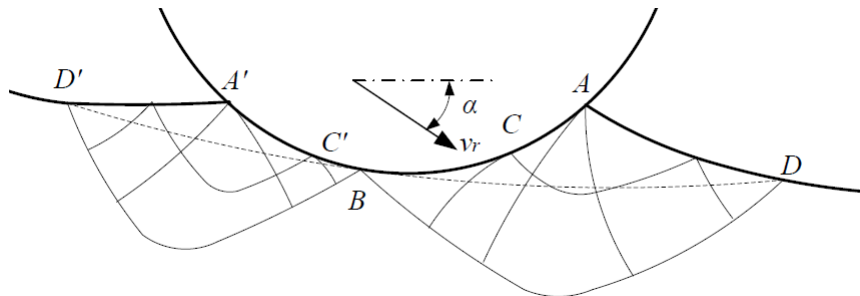


Fig. 16. Slip line field in the metal deformation zone of cold roll-beating

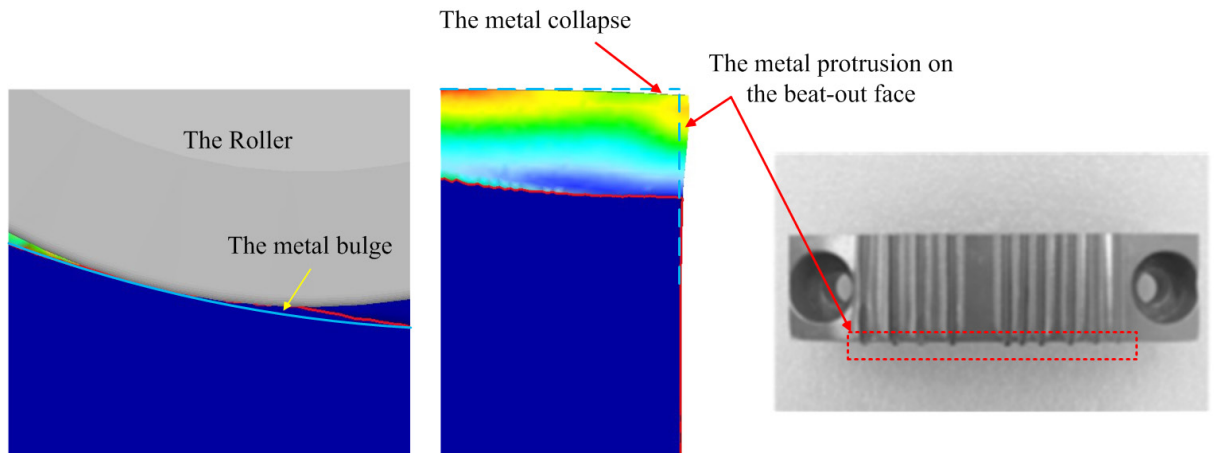


Fig. 17. The bulge, collapse, and protrusion of metal

consumes significant simulation time, but it provides the movement process of the metal deformation zone more intuitively, and shows the shape of the metal during and after deformation more completely.

In the future, the research work on the forming force of cold roll-beating should be combined with the finite element simulation method to simulate the whole cold roll-beating process to form a complete tooth groove, study the influence of the metal shape after deformation on the forming force, study the influence of elastic deformation of roller, and further improve the discrete analytical model.

7 CONCLUSIONS

1. The characteristics of deformation zone in cold roll-beating are analysed. The position and parameters of the deformation zone are constantly changing. The contact arc length and reduction are very small, and there is an incomplete deformation zone in the initial stage of cold roll-beating.
2. The discrete analytical model of unit pressure and deformation force in cold roll-beating is established. A cold roll-beating process is discretized into an infinite number of cold-rolling processes. The unit pressure of each cold-rolling process is calculated. The deformation force of cold roll-beating is calculated.
3. The change curves of cold roll-beating forming force are obtained by finite element simulation and experimental measurement. The results show that the change trend of cold roll-beating forming force predicted by the discrete analytical model is basically consistent with that of finite element simulation and experimental measurement. The maximum calculation error compared with the simulation and experiment results is about 7 % and 4 % respectively. The discrete analytical method is accurate in predicting the cold roll-beating forming force.

8 REFERENCES

- [1] Wu, T., Wang, G., Li, J., Yan, K. (2018). Investigation on gear rolling process using conical gear rollers and design method of the conical gear roller. *Journal of Materials Processing Technology*, vol. 259, p. 141-149, DOI:10.1016/j.jmatprotec.2018.04.034.
- [2] Liu, Z., Song, J., Li, Y., Li, X. (2011). Analysis and experimental study on cold-rolling precision forming process of involute spline. *Journal of Mechanical Engineering*, vol. 47, no. 14, p. 32-38. DOI:10.3901/JME.2011.14.032 (in Chinese).
- [3] Ma, Z., Luo, Y., Wang, Y., Mao, J. (2018). Geometric design of the rolling tool for gear roll-forming process with axial-infeed. *Journal of Materials Processing Technology*, vol. 258, p. 67-79, DOI:10.1016/j.jmatprotec.2018.03.006.
- [4] Fu, X., Wang, B., Zhu, X., Tang, X., Ji, H. (2016). Numerical and experimental investigations on large-diameter gear rolling with local induction heating process. *The International Journal of Advanced Manufacturing Technology*, vol. 91, p. 1-11, DOI:10.1007/s00170-016-9713-y.
- [5] Zhang, L., Li, Y., Yang, M., Yuan, Q. (2012). Finite element numerical simulation of high speed cold roll forming process. *Materials for Mechanical Engineering*, vol. 36, no. 8, p. 86-88, DOI:10.1007/s11783-011-0280-z (in Chinese).
- [6] Quan, J., Cui, F., Yang, J. (2008). Numerical simulation of involute spline shaft's cold-rolling forming based on ANSYS / LS-DYNA. *China Mechanical Engineering*, vol. 19, no. 4, p. 419-422 (in Chinese).
- [7] Wang, X., Xu, H., Cui, F. (2007). Finite element simulation of spline cold rolling forming. *Mining Machinery*, vol. 35, no. 9, p. 139-141 (in Chinese).
- [8] Wang, B., Yan, C., Li, J., Feng, P., Wang, S., Chen, S., & Su, J. (2021). Residual Stress and Deformation Analysis in Machining Split Straight Bevel Gears. *Strojniški vestnik - Journal of Mechanical Engineering*, vol. 67, no. 3, p. 114-122, DOI: 10.5545/sv-jme.2020.7064.
- [9] Yuan, Q., Li, Y., Yang, M. (2014). Research on deformation force of block material in cold roll forming. *China Mechanical Engineering*, vol. 25, no. 2, p. 251-256, DOI:10.3969/j.issn.1004-132X.2014.02.022 (in Chinese).
- [10] Kamouneh, A.A., Ni, J., Stephenson, D., Vriesen, R., DeGrace, G. (2007). Diagnosis of involutometric issues in flat rolling of external helical gears through the use of finite-element models. *International Journal of Machine Tools and Manufacture*, vol. 47, no. 7-8, p. 1257-1262, DOI:10.1016/j.ijmachtools.2006.08.015.
- [11] Zhang, D., Zhao, S., Ou, H. (2016). Analysis of motion between rolling die and workpiece in thread rolling process with round dies. *Mechanism and Machine Theory*, vol. 105, p. 471-494, DOI:10.1016/j.mechmachtheory.2016.07.008.
- [12] Li, Y., Zhang, D., Fu, J. (2007). Unit average pressure in cold rolling forming process of external spline. *China Mechanical Engineering*, vol. 18, no. 24, p. 2977-2980, DOI:10.3321/j.issn.1004-132x.2007.24.018 (in Chinese).
- [13] Li, R., Song, J., Li, Y. (2007). Calculation of rolling force in cold rolling forming of external spline. *Shanxi Metallurgy*, vol. 30, no. 6, p. 10-15, DOI:10.3969/j.issn.1672-1152.2007.06.004 (in Chinese).
- [14] Zhang, D., Xu, F., Yu, Z., Lu, K., Zheng, Z., Zhao, S. (2021). Coulomb, Tresca and Coulomb-Tresca friction models used in analytical analysis for rolling process of external spline. *Journal of Materials Processing Technology*, vol. 292, DOI:10.1016/j.jmatprotec.2021.117059.
- [15] Quagliato, L., Berti, G.A. (2017). Temperature estimation and slip-line force analytical models for the estimation of the radial forming force in the RARR process of flat rings. *International Journal of Mechanical Sciences*, vol. 123, p. 311-323, DOI:10.1016/j.ijmecsci.2017.02.008.

- [16] Quagliato, L., Berti, G.A., Kim, D., Kim, N. (2018). Slip line model for forces estimation in the radial-axial ring rolling process. *International Journal of Mechanical Sciences*, vol. 138-139, p. 17-33, DOI:10.1016/j.ijmecsci.2018.01.025.
- [17] Ma, Z., Luo, Y., Wang, Y. (2018). On the pitch error in the initial stage of gear roll-forming with axial-infeed. *Journal of Materials Processing Technology*, vol. 252, p. 659-672, DOI:10.1016/j.jmatprotec.2017.10.023.
- [18] Zhou, J., Wang, Z., Gao, Y., Lun Y. (1994). Flow stress mathematical model of aluminum alloy. *Journal of Beijing University of Science and Technology*, vol. 16, no. 4, p. 351-356 (in Chinese).
- [19] Guan, K., Fan, B., Zhou, J. (1996). Experimental study on thermal deformation of brass. *Acta Metallurgica Sinica*, vol. 32, no.7, p. 749-754, DOI:CNKI:SUN:JSXB.0.1996-07-011 (in Chinese).
- [20] Dai, Z., Zhou, J., Zhang, S. (1997). A mathematical model for flow stress of copper alloy in cold state. *Nonferrous Metals*, vol. 49, no. 2, p. 88-91, DOI:CNKI:SUN:YOUS.0.1997-02-018 (in Chinese).
- [21] Zhang, S., Dai, Z., Zhou, J. (1997). Mathematical model of cold flow stress for aluminum alloy. *Journal of Beijing University of Science and Technology*, vol. 19, no. A02, p. 65-68, DOI:CNKI:SUN:BJKD.0.1997-S1-01 (in Chinese).
- [22] Challen, J.M., Oxley, P.L.B. (1984). Slip-line fields for explaining the mechanics of polishing and related processes. *International Journal of Mechanical Sciences*, vol. 26, no. 6, p. 403-418, DOI:10.1016/0020-7403(84)90030-4.
- [23] Busquet, M., Torrance, A.A. (1999). Investigation of surface deformation and damage when a hard cylindrical asperity slides over a soft smooth surface. *Tribology Series*, vol. 36, p. 101-109, DOI:10.1016/S0167-8922(99)80032-7.
- [24] Hill, R. (1950). *The Mathematical Theory of Plasticity*. Oxford University Press, Inc., New York.
- [25] Zhang, H., Wang, M. (1989). Effect of aluminum adhesion on rolling friction coefficient. *Light Alloy Processing Technology*, vol. 9, p. 17-19 (in Chinese).

Design and Optimization of an Umbrella-Type Shield Based on 3D CFD Simulation Technology

Longfei Li¹ – Xin He¹ – Taowei Jiao¹ – Yumeng Xiao¹ – Xipan Wei^{1,2} – Wei Li^{1,*}

¹ Northwest A&F University, College of Mechanical and Electronic Engineering, China

² Weichai Power Co., Ltd, China

Mechanical shields can effectively alleviate the problems of low pesticide utilization and severe environmental pollution. This manuscript uses a computational fluid dynamics (CFD) method to investigate the anti-drift mechanism of mechanical shields, study the airflow forms around them, and establish an accurate simulation model. The aerodynamic characteristics of six shields were studied, and their anti-drift effect was compared. Then, the size and working parameters were optimized using the response surface methodology (RSM). Mechanical shields can significantly improve the fog droplet deposition rate (DR) compared with the conventional spray method (no shield), among which the umbrella-type shield has the best effect; optimizing the size and selecting suitable working parameters can increase the DR to 77.31 %. The field trial showed that the DR of the conventional spray method was reduced by 31.9 % at 5 m/s compared with 3 m/s, while the DR of the shield spray method was reduced by only 3.6 % at 5 m/s compared with 3 m/s, which proved the excellent performance of the mechanical shields. The field trial results were consistent with the CFD simulation, and the relative deviation of the DR between the two was within 4 %, so the accuracy and reliability of the CFD simulation model were proved.

Keywords: mechanical shield, anti-drift, CFD simulation

Highlights

- Designed and optimized a new shield (umbrella-type shield) and conducted experimental validation.
- Put the mechanical shields into a 3D model to study them and establish an accurate simulation model.
- CFD was applied to simulate the spray flow fields of six mechanical shields to obtain their continuous phase and discrete phase information.
- Simulate the spray process deposited on the leaf surface of the target plant and compare it with the field trial results.

0 INTRODUCTION

Spraying pesticides is a powerful means of combatting plant diseases, pests, and weeds. The smaller the particles of the sprayed solution, the better the coverage and penetration of the solution [1]; spraying can improve the control effect of diseases, pests, and weeds [2]. However, the smaller the particle size of the drug solution, the weaker its ability to resist external environmental changes. This is mainly seen in poor drift resistance and a low fog droplet deposition rate (DR).

Mechanical shields are deflector devices installed near the nozzles of sprayers. During spray operation, the shields can change the velocity and direction of airflow around the nozzles, thus changing the trajectory of the fog droplets and deposition of coercive fog droplets to the target [3]; mechanical shields have thus demonstrated significant value in reducing droplet drift and improving pesticide utilization. While some studies examined the application of mechanical shields, research focusing on their drift reduction mechanisms and optimization remains relatively limited [4] and [5].

In previous research, Ozkan et al. [6] investigated the effectiveness of nine types of mechanical shields in reducing droplet loss using the distance from the nozzle to the droplet mass centre as an evaluation parameter in wind tunnel conditions. Although the experiments ultimately demonstrated the effective reduction of droplet drift by the shields, wind tunnel test conditions are demanding, with high costs per trial and results that may lack intuitiveness. Similarly, Tasy et al. [7] evaluated several types of mechanical shields using two-dimensional (2D) computational fluid dynamics (CFD) software and noted their good drift reduction performance when appropriate operating parameters such as spray pressure and droplet release angles were selected, but they did not delve into other factors or causes.

In contrast, this study seeks to explore the airflow patterns and aerodynamics surrounding mechanical shields in greater depth and simulate the three-dimensional (3D) dynamics of droplet drift and deposition. By employing 3D CFD simulation, we aim to investigate the drift reduction mechanisms of shields and further enhance their effectiveness, providing valuable technical insights for optimizing and improving mechanical shields. The motion of

the droplets can be considered to be a fluid motion. Methods for studying fluid motion are usually characterized by complex experiments and difficult-to-observe results; however, the emergence of CFD has broken this deadlock. CFD simulation is a method dedicated to studying fluid motion; compared to traditional wind tunnel experiments, CFD simulation offers advantages in terms of lower device complexity, cost-effectiveness, reliable variables, and experimental reproducibility, thereby presenting extensive prospects for application [8] and [9].

The primary objective of this study is to explore the drift reduction mechanisms of mechanical shields through 3D simulation models and further improve their effectiveness in reducing drift. This research aims to provide technical references for the optimization and improvement of mechanical shields. By studying the airflow models surrounding the shields and corresponding droplet trajectories, we will determine the impact of different shields on the DR and select the shield with the best performance. Additionally, we will investigate the optimal size and operating parameters of the shield to further enhance its drift reduction efficiency. Finally, we will validate the reliability of the simulation results through field experiments, thereby confirming the practical value and novelty of this research.

1 METHODS AND EXPERIMENTAL

1.1 Mechanical Shield Structure Determination

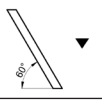
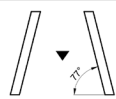
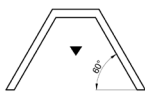



Mechanical shields can be divided into many types according to shape. In this manuscript, six types of shields were designed and selected for comparative investigation based on several mainstream shield forms. Their specific structural shapes are shown in Table 1.

1.2 Air-Liquid Two-Phase Flow Theory

The choice of using the theory of continuous phase and dispersed phase is based on the characteristics and phenomena of multiphase flow, which involves the interaction and transfer processes between two or more phases, such as the interaction between gas and liquid droplets, droplet collision, and deposition. These phenomena need to be described using appropriate physical property models to achieve accurate simulation and prediction.

In the air-liquid two-phase flow process, the FLUENT module treats the air as a continuous phase and the fog droplets as discrete phases in the

Table 1. Types of shields (triangles indicate nozzles)

Name	Type	Structure schematic	Characteristic	Application
a	Single baffle		One baffle	
b	Double baffle		Two baffles	
c	Three-sided baffle		Three sides baffles	Whole row nozzles
d	Double circular arc		Two arc baffles with different diameters	
e	U		Arc baffle	
f	Umbrella		Hemisphere, wind-assisted	Single nozzle

continuous phase [10]. This choice stems from the relative stability of air's physical properties, making it easier to model and solve using the equations of continuous media. The motion and transfer processes of air can be described using the Navier-Stokes equations, which are commonly employed in CFD simulations as fundamental fluid mechanics equations. In contrast, the droplets are the primary focus of attention because their behaviour determines the diffusion, deposition, and effectiveness of the pesticide. Therefore, it is essential to consider the mass, size, velocity, and shape of the droplets. These attributes can be described using droplet dynamics equations and other relevant models. The standard $K-\varepsilon$ turbulence model was used in the numerical simulation of the air-liquid two-phase flow of the shield spray. Considering that the volume of fog droplets is tiny in proportion to the whole flow field, the momentum of fog droplets is much smaller than the momentum of the airflow. The influence of fog droplets on the airflow field is ignored and can be calculated as steady-state incompressible flow. Since the spray operation is carried out at room temperature, there is no need to consider energy transfer; only the conservation of mass and the conservation of momentum needs to be considered [11] and [12].

The conservation of mass equation is:

$$\frac{\partial p}{\partial t} + \text{div}(\rho U) = 0, \quad (1)$$

where ρ is the density of fluid [kg/m³], t time [s], div divergence, and U velocity vectors.

For steady-state incompressible flow, the velocity dispersion is zero, i.e.:

$$\text{div}(U) = \frac{\partial u}{\partial x} + \frac{\partial u}{\partial y} + \frac{\partial u}{\partial z} = 0. \quad (2)$$

The conservation of momentum equation is the Navier-Stokes equation [8], and the conservation of momentum equation of viscous incompressible fluid is:

$$\frac{\partial(u)}{\partial t} + \text{div}(uU) = S_u - \frac{1}{\rho} \frac{\partial p}{\partial x} + \text{div}(v\text{grad}u), \quad (3)$$

$$\frac{\partial(v)}{\partial t} + \text{div}(vU) = S_v - \frac{1}{\rho} \frac{\partial p}{\partial y} + \text{div}(v\text{grad}v), \quad (4)$$

$$\frac{\partial(w)}{\partial t} + \text{div}(wU) = S_w - \frac{1}{\rho} \frac{\partial p}{\partial z} + \text{div}(v\text{grad}w). \quad (5)$$

Among which:

$$\left\{ \begin{aligned} \text{grad}(u) &= \frac{\partial(u)}{\partial(x)} + \frac{\partial(u)}{\partial(y)} + \frac{\partial(u)}{\partial(z)} \\ \text{grad}(v) &= \frac{\partial(v)}{\partial(x)} + \frac{\partial(v)}{\partial(y)} + \frac{\partial(v)}{\partial(z)} \\ \text{grad}(w) &= \frac{\partial(w)}{\partial(x)} + \frac{\partial(w)}{\partial(y)} + \frac{\partial(w)}{\partial(z)} \end{aligned} \right. , \quad (6)$$

$$\left\{ \begin{aligned} S_u &= Fx / \rho \\ S_v &= Fy / \rho, \\ S_w &= Fz / \rho \end{aligned} \right. \quad (7)$$

where u, v, w are the components of U in the $x, y,$ and z directions, ν kinematic viscosity [m²/s], p intensity of pressure [MPa], and S_u, S_v, S_w generalized source items.

In the process of gas-liquid two-phase flow, there is always a mutual transfer of mass and momentum between the two phases. Therefore, the control equations for the continuous phase (air) and the discrete phase (fog droplet) must be solved alternately until the solutions for both phases converge.

The momentum value and mass value transferred from the continuous phase to the discrete phase are calculated according to the change in momentum and mass [13].

The value of the change in fog droplet momentum is:

$$F = \sum \left[\frac{3\beta\mu C_D Re}{4\rho_p d_p^2} (u_p - u) + F_O \right] \cdot m_p \Delta t. \quad (8)$$

The value of the change in fog droplet mass is:

$$M = \frac{\Delta m_p}{m_{p,0}} \dot{m}_{p,0}, \quad (9)$$

where μ is viscosity of continuous phase fluid [N·s/m²], C_D drag coefficient, Re relative Reynolds number of fog droplets, ρ_p density of discrete phases [kg/m³], d_p diameter of the droplets [m], u_p discrete phase velocity [m/s], u continuous phase velocity [m/s], F_O other forces [N], \dot{m}_p mass flow rate of fog droplets [kg/s], and t time [s].

1.3 CFD Simulation Model Building

The nozzles were selected from the Lechler 110-05 standard vertebral fan nozzle produced by Lechler, Germany, whose fog droplet size distribution meets the Rosin-Rammler distribution law. The Visi Sizer DP Particle Sizing System Model 6401 (Tianjin Celes Automation Technology Co., Ltd., Tianjin, China) can measure the nozzle fog droplet spectrum, where the smallest fog droplet size of 17.5 μm , the largest particle size of 340 μm , and the medium diameter of 150.4 μm . The Rosin-Rammler distribution law assumes an exponential relationship between the fog droplet diameter and the mass fraction of fog droplets larger than this diameter.

$$Y_d = e^{-(d/\bar{d})^n}, \quad (10)$$

where Y_d is the mass percentage of fog droplets with a diameter greater than d [%], d fog droplet diameter [μm], \bar{d} average fog droplet diameter [μm], and n dispersion coefficient.

When $d = \bar{d}$, $Y_d = e^{-1} \approx 0.368$ is obtained by the interpolation method $\bar{d} = 171.7 \mu\text{m}$. The fog droplet parameters d and Y_d are arranged in the format of the Rosin-Rammler distribution, and the dispersion coefficient n is calculated and finally averaged \bar{n} .

The dispersion coefficient n is calculated as follows:

$$n = \frac{\ln(-\ln Y_d)}{\ln(d/\bar{d})}. \quad (11)$$

From Eqs. (10) and (11), the average value of the dispersion coefficient $\bar{n} = 2.762$ can be calculated.

In the FLUENT simulation, the jet source (nozzle) released 2000 fog droplets at the same velocity of 20 m/s. A simulation area is established to

simulate a wind tunnel. Referring to previous studies [14] and [15], the nozzle is set in the shield from the bottom of the simulated flow field height of 0.5 m, 1 m downwind from the natural wind inlet, and the fog droplet release angle vertically down, as shown in Fig. 1.

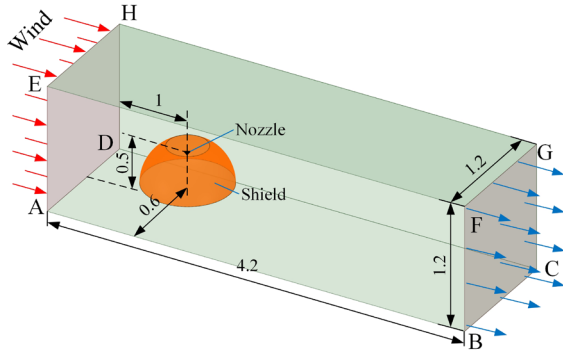


Fig. 1. Flow field simulation area, units in [m]

In the calculation area shown in Fig. 1, the ground (ABCD) is set to “trap”, and the trajectory calculation is terminated when the fog droplet moves this, and the fog droplet is deposited. The sides (ABFE, CDHG), top (EFGH), and back (BCGF) are set as the “escape” boundary. When the fog droplets move to the “escape” boundary, they are considered to have drifted, and the trajectory calculation is terminated. By setting the shield surface to “trap”, the trajectory calculation is terminated when the fog droplet reaches this interface, and the fog droplet is considered to have drifted. According to the operation specification of the plant protection machinery, the sprayer is not allowed to work when the natural wind in the field is above level 3 (3.4 m/s to 5.4 m/s), so the wind speed is set to 5 m/s.

The physical properties of the continuous and discrete phases used in the model are shown in Table 2 (the data are calculated values, except for temperature, and flow velocity, which are measured data).

Table 2. Properties of continuous and discrete phases

Continuous phase (air)		Discrete phase (fog droplet)	
Temperature [K]	293	Temperature [K]	293
Density [kg/m ³]	1.225	Density [kg/m ³]	998.2
Thermal conductivity [W/(mK)]	0.025	Thermal conductivity [W/(mK)]	0.599
Viscosity [mPa·s]	0.0176	Viscosity [mPa·s]	1.0100
Molar mass [g/mol]	28.97	Molar mass [g/mol]	18.02
Turbulence intensity [%]	20	Vaporization temperature [K]	273
Flow velocity [m/s]	5	Surface tension [N/m]	0.07275

2 RESULTS AND DISCUSSION

2.1 CFD Simulation

Due to the disjointed nature of the 3D space, the simulation results are visualized using the centre section of the model.

2.1.1 Mechanical Shields Performance Comparison

Fig. 2. shows the results of concurrent flow field simulations of continuous phase velocities for six types of shields, with colour differences to distinguish the flow velocities.

The blocking effect of the baffles (Figs. 2a, b and c) inevitably leads to a low-velocity area behind the shield. The shield (Fig. 2d) creates a high-velocity airflow directly behind the spray outlet, which may force fog droplets downward and reduce interference with fog droplet trajectories in the low-velocity region. The shield (Fig. 2e) will form a certain amount of cyclonic flow inside, preventing the tiny diameter fog droplets from leaving the shield and being deposited on the inner surface of the shield. The top and bottom of the shield (Fig. 2f) will form two high-velocity zones because of the auxiliary airflow effect, eliminating the internal vortex. In addition, the shield (Fig. 2f) can better resist the wind from all directions in the plane. In comparison, the shield (Fig. 2f) effect is more desirable.

Fig. 3. shows the trajectory of the discrete phase of the shield, with different colours representing the corresponding fog droplet diameters. It can be roughly seen that the fog droplets less than 77 µm in diameter move upward most easily.

The simulation shows that in the low velocity zone formed by the geometry of shield (Fig. 3a, b, and c) the fog droplets with smaller diameter will move in the low velocity zone and eventually drift away downwind; High velocity airflow is generated directly behind the spray outlet of the shield (Fig. 3d) forcing the smaller fog droplets downward, and only fog droplets less than 137 µm in diameter are lost from the viewing field; From the fog droplet trajectories of the shield (Fig. 3e), it can be seen that most of the fog droplets with diameters less than 77 µm cannot be detached from the inside of the shield under the action of the cyclonic flow inside the shield, and finally deposited on the shield, while fog droplets with diameters less than 166 µm will be lost from the observation field; The shield (Fig. 3f) eliminates internal cyclonic flow due to the auxiliary airflow, and the fog droplets move downward under the action

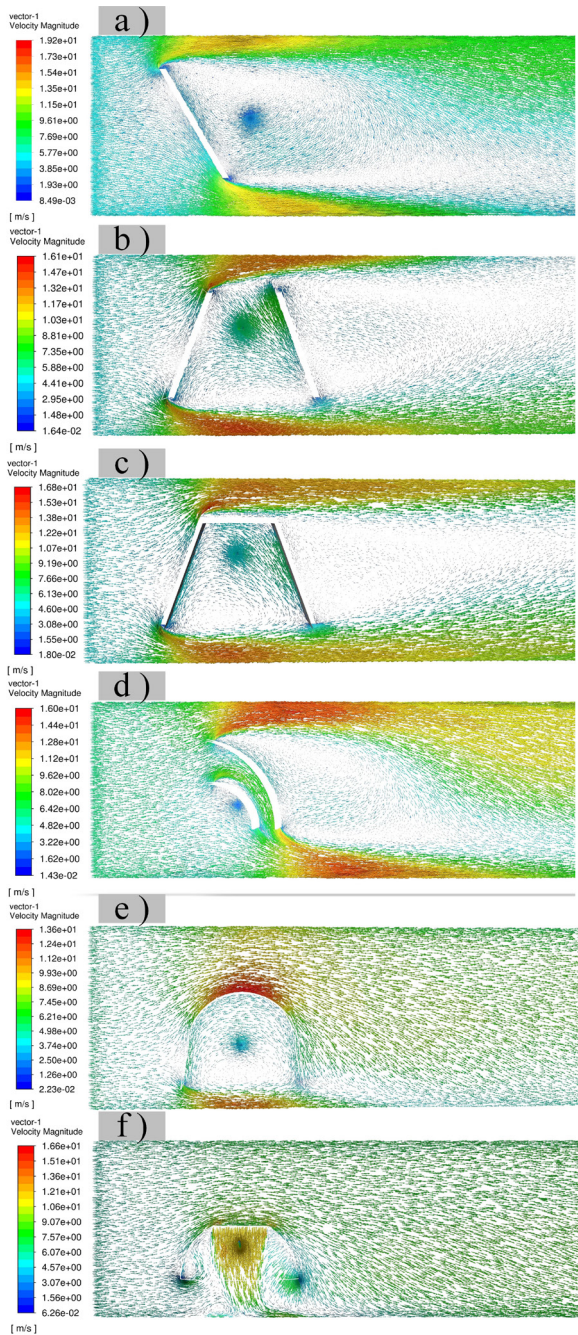


Fig. 2. Convergent flow field with continuous phase velocity

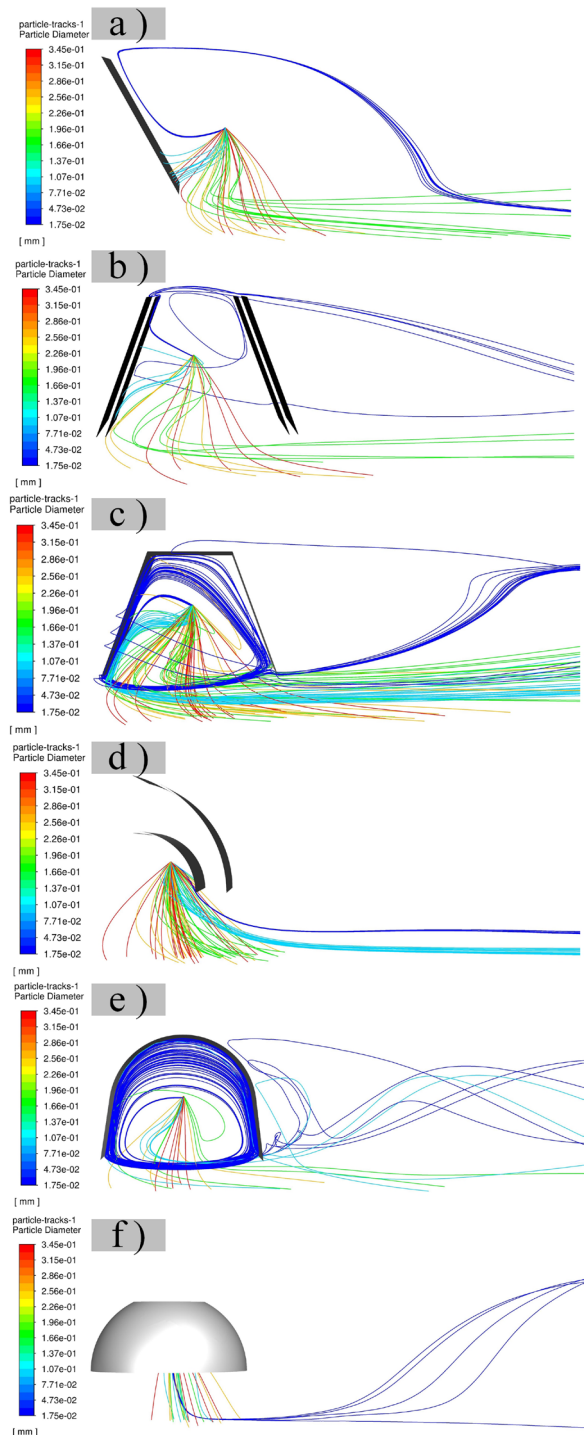


Fig. 3. Discrete phase motion trajectory of different shields

of the auxiliary airflow and are not deposited on the shield. Meanwhile, some of the fog droplets that would otherwise be lost and fog droplets larger than $77\ \mu\text{m}$ in diameter are deposited under the pushing effect of the auxiliary airflow.

The final state of the droplets can be divided into two types: deposition and loss, while droplet loss

can be divided into loss deposited on the shield and droplet drift loss, etc., where the loss deposited on the shield can be derived directly from the calculation, so the performance of several shields was evaluated by using the *DR* and the *DS* (percentage of fog droplets

deposited on the shield) as evaluation indexes. The larger the DR , the smaller the DS , and the better the anti-drift effect.

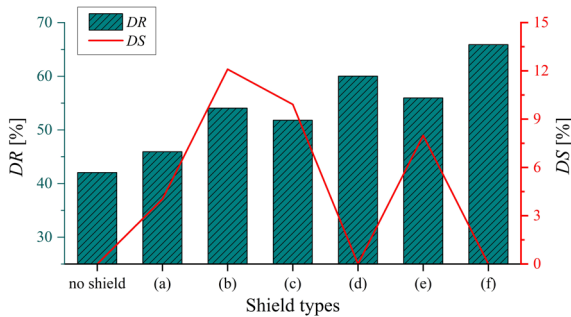


Fig. 4. Shield performance comparison

The simulation results are shown in Fig. 4, and it can be found that shield (f) (umbrella-type shield) has the highest DR and almost zero DS , so shield (f) has the best anti-drift effect among the six types of shields mentioned above.

2.2 Optimization of Shield Size and Working Parameters

The umbrella-type shield (f) structural size is shown in Fig. 5; the nozzle maximum spray angle of 110° .

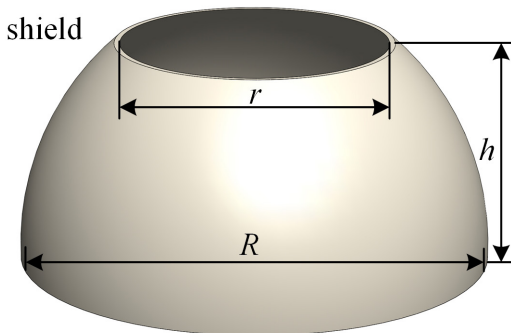


Fig. 5. Umbrella-type shield structure

2.2.1 Optimization of Shield Size Parameters

Simulation tests were conducted to improve the umbrella-type shield’s anti-drift effect for different sizes. Based on the Response Surface Methodology, the DR is used as the response value. The R (diameter of the outlet), r (diameter of auxiliary air inlet), and h (height) are used as factors, and a regression equation of response values and factors was established to obtain the optimal size parameters of the shield.

The specific factors and levels are shown in Table 3.

Table 3. Size parameters test factors and levels table

Levels	Factors		
	R [mm]	r [mm]	h [mm]
-1	400	250	200
0	500	300	240
1	600	350	280

Table 4. Simulation tests result for shield size parameters optimization

No.	Factors			DR [%]
	R [mm]	r [mm]	h [mm]	
1	500	300	240	72.62
2	400	300	200	55.46
3	400	350	240	56.44
4	500	250	280	62.63
5	500	250	200	62.75
6	600	350	240	65.45
7	500	300	240	73.87
8	500	350	280	64.46
9	600	300	200	63.64
10	500	300	240	73.11
11	400	250	240	56.63
12	600	300	280	63.21
13	500	300	240	70.21
14	500	300	240	72.53
15	400	300	280	57.88
16	600	250	240	59.89
17	500	350	200	63.17

With the help of the Box-Behnken method in Design-expert 13 software. The optimization algorithm obtained the optimal value of DR , considering multiple factors simultaneously (As Table 4).

The model’s fit $R^2 = 0.9852$ indicates that the model fits well to the DR , and the test error is small. The regression equation of the DR was imported into Origin 2022 software, and the effects of the R , r , and h on the DR were obtained, as shown in Fig. 6.

It is evident from Fig. 6 that when two of the three size parameters of the shield are fixed, the DR tends to increase and then decrease with another factor, which shows that the shield size parameters can be optimized to obtain the best value.

The nozzle’s working area can be considered a conical area with the nozzle as the vertex. Under the premise of other consistent parameters, the DR depends on the ratio X of the exit plane of the shield and the projection of the nozzle working area in the exit plane of the shield. The R , r , and h are the three primary parameters influencing the ratio X . The closer the ratio X is to the C (constant value related to the

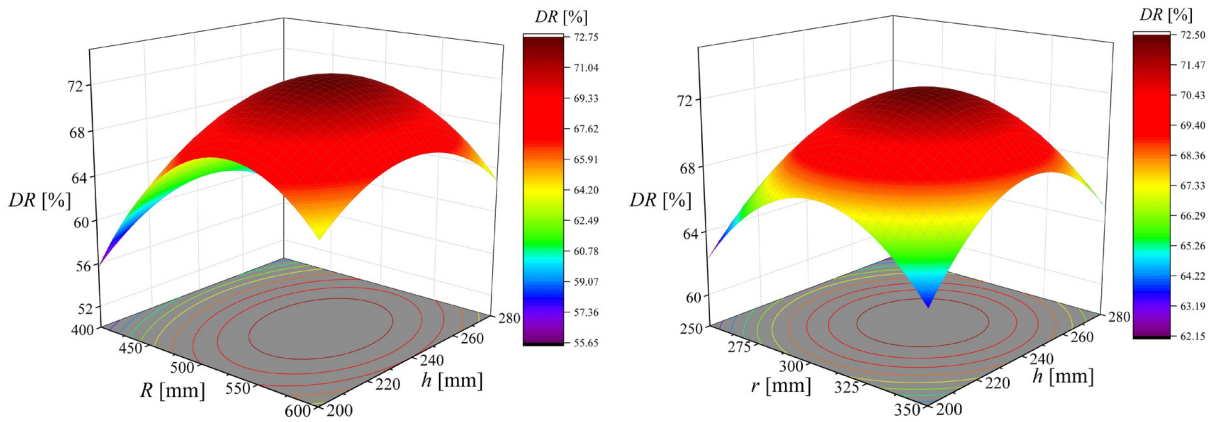


Fig. 6. Effect of shield size parameters on DR

working parameters and nozzle characteristics), the higher the DR . When the ratio X is less than C , the spray will form a high-velocity airflow in the shield, causing fog droplets to collide and be ejected, forming larger fog droplets, affecting their trajectories so that the DR decreases. In contrast, when the ratio X is bigger than C , a vortex region will be formed between the auxiliary wind and the natural wind, reducing the anti-drifting effect of the shield and the DR .

According to manufacturing accuracy and the calculation prediction of the software, when $R = 521$ mm, $r = 307$ mm, and $h = 241$ mm, the maximum DR can be 72.93 %.

2.2.2 Optimization of Working Parameters

To investigate the effect of working conditions on the anti-drift effect of the shield further [13], [16], and [17], the optimal working conditions were investigated based on the size parameters of the shield (f) obtained by optimization in the previous. The plant model is

added to the spray simulation area, consisting of dual nozzles and two parallel rows for simulation. The spray model was built, as shown in Fig. 7.

Simulation sampling and data processing are conducted by changing the blower speed N , nozzle height H (the distance between the nozzle and the shield outlet plane), and spray pressure P . The factors and levels of N , H , and P are shown in Table 5.

Table 5. Factors and levels table

Levels	Factors		
	N [rpm]	H [mm]	P [MPa]
-1	1500	100	0.3
0	2500	140	0.4
1	3500	180	0.5

With the help of Design-expert 13 software, 17 simulation tests were carried out for the design, and the optimization algorithm obtained the optimal value of DR , considering multiple factors simultaneously.

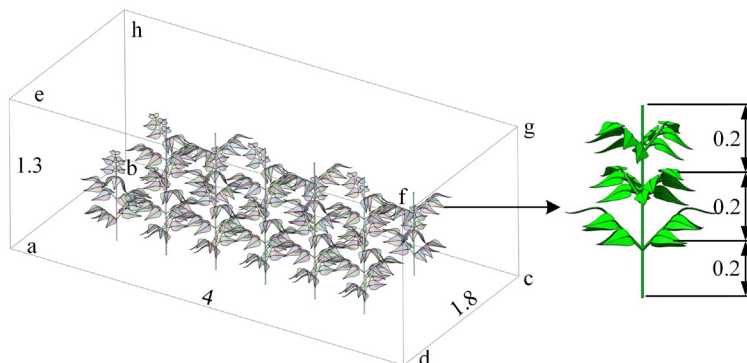


Fig. 7. Optimization model of working parameters; units in [m]

Table 6. Simulation result for working parameters

No.	Factors			DR [%]
	N [rpm]	H [mm]	P [MPa]	
1	2500	100	0.3	71.36
2	2500	140	0.4	73.67
3	3500	100	0.4	71.16
4	2500	180	0.3	76.81
5	1500	140	0.3	69.91
6	2500	140	0.4	76.56
7	2500	140	0.4	74.28
8	3500	140	0.5	67.59
9	2500	180	0.5	67.50
10	3500	140	0.3	73.82
11	1500	100	0.4	64.24
12	2500	140	0.4	73.77
13	2500	140	0.4	75.08
14	3500	180	0.4	67.90
15	1500	180	0.4	64.84
16	2500	100	0.5	69.36
17	1500	140	0.5	63.44

The simulation results (Table 6) show that the model fits well, and the possibility of test error is slight.

The regression equation and the range of values of each factor were imported into Origin 2022 software, and the effects of the N , H , and P on the fog droplet deposition rate DR were obtained, as shown in Fig. 8.

From Fig. 8, it can be seen that the rest of the factors are fixed values.

The DR increases and then decreases with increasing the N . It is because the bigger the N in a particular range, the greater the blower creates the auxiliary wind, and the more the rapid deposition of fog droplets reduces drift; however, due to the limitations of the shield structure, the auxiliary wind speed is too large to make the droplets too concentrated and difficult to spread, resulting in reduced DR .

The DR increases and then decreases with increasing the H . This is because in a particular range, with the increase of the H , the ratio X gradually close to C , and DR gradually increases; however, more than the critical value, the formation of vortex areas between the auxiliary wind and natural wind, DR decreases.

The DR decreases with increasing the P . This is because the smaller the P , the larger the fog droplet particles and the stronger the ability to resist the

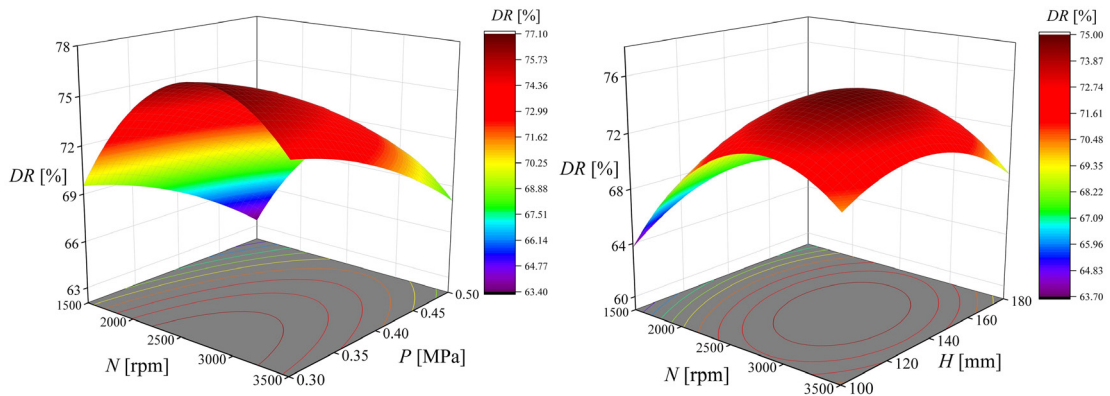


Fig. 8. Effect of each working parameter on DR

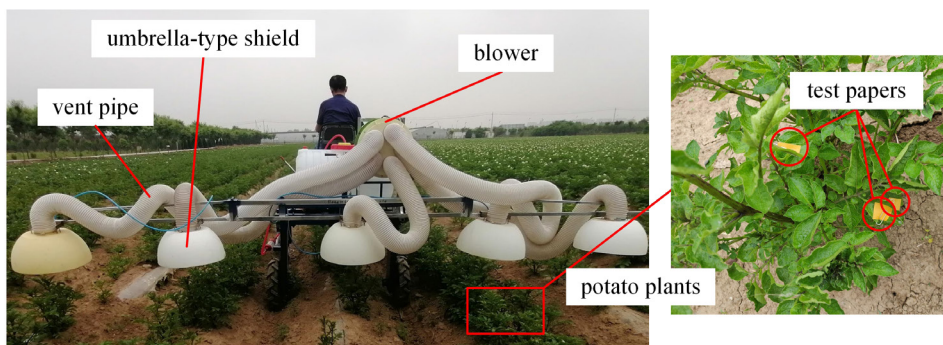


Fig. 9. Spray system structure

natural wind; however, in practice, the P must not be less than 0.3 MPa.

By combining calculation and practice, the optimum spray working conditions were found when $P = 2700$ rpm, $H = 150$ mm, $P = 0.3$ MPa, and the maximum DR can be 77.31 %.

2.3 Validation

To evaluate both the anti-drift effectiveness of the shield spray system and validate the accuracy of our CFD model, two experimental studies were conducted.

As shown in Fig. 9, the spray system used in the experiment consists of a blower, vent pipes, umbrella-type shields, nozzles, and related controllers. The nozzles of the sprayer were selected as the standard vertebral fan fog nozzle SC 110-05 produced by Lechler, Germany. The design of the umbrella-type shield was based on the specific test conditions required for the simulation tests.

For each group of experiments, 30 consecutive potato plants in the same row were selected, and sampling points were arranged at the highest point, 3/4 height, and 1/4 height of the leaves of 10 potato plants. Fog droplet test papers (30 mm × 40 mm) were used as the sampling sheets, with one sheet placed on the surface of each selected leaf. A dye (Rhodamine-B) was added to the water used as the pesticide (concentration: 0.2 %). The amount of spray liquid applied was recorded after the completion of the test and the drying of the fog droplets on the sampling sheets. Similar to the principle of water-sensitive paper, the fog droplets reacted with the dye and appeared blue.

Based on the results obtained from the fog droplet test papers, the DR was derived using Eq. (12), which is an equation specific to the analysis of the test data. Each experiment was repeated three times, and the average value was calculated to ensure the accuracy and reliability of the results.

2.3.1 Anti-Drift Effect Comparison Test

The test was designed to verify the practical effectiveness of the umbrella shield in reducing spray drift. External wind speeds were set as independent variables at 3 m/s and 5 m/s, and the rest of the parameters were kept constant: spray pressure was 0.4 MPa, blower speed was 3000 rpm, and nozzle height was 150 mm. The control group was set up with conventional spray (no shield).

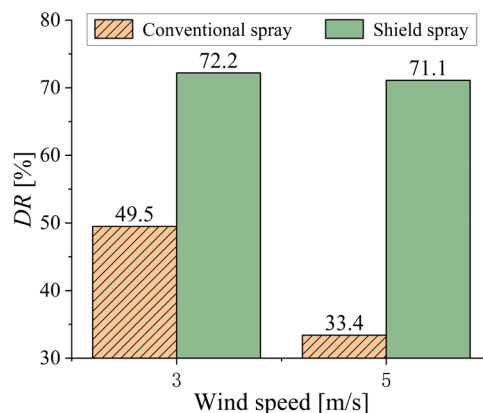


Fig. 10. Comparison of DR between the two methods

It can be seen from Fig. 10. that the DR of the shield spray method is much higher than that of the conventional spray method. The DR of the conventional spray method is greatly affected by the wind speed, and the DR decreases significantly as the wind speed increases. When the external wind speed increased from 3 m/s to 5 m/s, the DR before and after comparison during the conventional spray method decreased by 32.5 %, which was a large change, while the DR before and after comparison of the shield spray method decreased by only 1.5 % which was an insignificant change. The comparison test proved that the mechanical shield played a significant role in anti-drift during the spray process.

2.3.2 CFD Simulation Accuracy Verification Test

The simulation results were evaluated using the DR and the distribution coefficient of variation (CV) as evaluation indexes to verify the accuracy of the CFD model. The blower speed N was adjusted to 1000 rpm, 2000 rpm, and 2700 rpm, the nozzle height H was 150 mm, the spray pressure P was 0.3 MPa, and the natural wind speed was about 3.4 m/s.

(1) The fog droplet deposition rate

The test value of DR can be obtained from the ratio of the deposition volume per unit area to the spray volume per unit area in the application area [18], calculated as:

$$DR = \frac{\bar{m} \times LAI \times S_a}{m_a} \quad (12)$$

where \bar{m} is the mean value of fog droplet deposition rate per unit area of target plants, LAI leaf area index, S_a the projected area of leaves in the test area, and m_a application rate in the test area.

The results were entered in Table 7, where DR is the fog droplet deposition rate obtained from the field trial and DR_F is the fog droplet deposition rate obtained from the simulation.

Table 7. The fog droplet deposition rate

N [rpm]	DR [%]	DRF [%]	Relative deviation [%]
1000	68.25	70.83	3.78
2000	71.84	73.59	2.44
2700	74.56	77.22	3.67

(2) The distribution coefficient of variation

Numerical analysis was used to calculate the mean values of fog droplet deposition on the target plants' upper, middle, and lower foliage to calculate the CV , which indicates the deviation of fog droplet deposition on each leaf layer of the target plant from the mean value; the smaller the value, the better the uniformity of fog droplet deposition distribution [19].

$$CV = \left(\sqrt{\frac{\sum_{i=1}^n (q_i - \bar{q})^2}{n-1}} / \bar{q} \right) \times 100 \%, \quad (13)$$

where q_i is fog droplet deposition for the i^{th} sample [$\mu\text{g}/\text{cm}^2$], \bar{q} is the average value of fog droplet deposition [$\mu\text{g}/\text{cm}^2$], and n is total number of samples.

Table 8. Coefficient of variation of the distribution of fog droplet deposition

N [rpm]	CV [%]	CVF [%]	Relative deviation [%]
1000	18.59	17.34	6.72
2000	20.32	18.98	5.59
2700	13.58	12.76	6.01

The calculated results are shown in Table 8, where CV is the coefficient of variation of the fog droplet deposition distribution from the field trial, and CV_F is the coefficient of variation of the fog droplet deposition distribution from the simulation.

It can be seen from the comparison results that the field trial results are consistent with the CFD simulation test results, with only minor deviations. The DR of the field trial is slightly smaller than the CFD simulation, and the relative deviation is within 4 %. The CV of the field trial is slightly larger than the CFD simulation, and the relative deviation is within 7 %. The main reason for the discrepancy is uncontrollable factors, such as the natural wind variation and the bounce phenomenon of fog droplets. That is what causes the loss of a small amount of fog droplets.

The field trial proved that the deviation between the CFD simulation and the actual is small and negligible, and the accuracy of the CFD model can fully meet the requirements of practical use.

3 CONCLUSIONS

The 3D CFD simulation model is more in line with the field reality (fog droplets can move in three dimensions), which is an economical and practical method for performance evaluation, especially for shield design and optimization.

1. A new type of shield has been designed. By comparing six types of shields, it was found that the umbrella-type shield has the best performance.
2. Dimensions of the umbrella-type shield have been optimized according to agronomic requirements. When $R = 521$ mm, $r = 307$ mm, and $h = 241$ mm, the maximum DR can be 72.93 %.
3. Optimal working parameters were selected according to the field operating conditions. The optimum parameters were found when $P = 2700$ rpm, $H = 150$ mm, $P = 0.3$ MPa, and the maximum DR can be 77.31 %.

Future research on mechanical shields should consider the effect of multiple nozzles working simultaneously on the simulation results and needs further study to be verified.

4 ACKNOWLEDGEMENTS

This research was funded by the Science and Technology Project of China Tobacco Corporation Shaanxi Province, Construction of a Standard System for Suitable Mechanized Tobacco Agriculture in Shaanxi Tobacco Area and Demonstration and Promotion of Integration of Agricultural Machinery (KJ-2022-02) and Agriculture and the Key Industry Chain Innovation Project of the Shaanxi Province (2018ZDCXL-NY-03-06).

5 REFERENCES

- [1] Boudimos, G., Koutsiaras, M., Psiroukis, V., Balafoutis, A., Fountas, S. (2019). Development and field evaluation of a spray drift risk assessment tool for vineyard spraying application. *Agriculture*, vol. 9, no. 8, DOI:10.3390/agriculture9080181.
- [2] Miranda-Fuentes, A., Marucco, P., Gonzalez-Sanchez, E.J., Gil, E., Grella, M., Balsari, P. (2018). Developing strategies to reduce spray drift in pneumatic spraying in vineyards: Assessment of the parameters affecting droplet size in pneumatic spraying. *Science of the Total Environment*, vol. 616-617, p. 805-815, DOI:10.1016/j.scitotenv.2017.10.242.

- [3] Osuch, A., Przygodzinski, P., Rybacki, P., Osuch, E., Kowalik, I., Piechnik, L., Przygodzinski, A., Herkowiak, M. (2020). Analysis of the effectiveness of shielded band spraying in weed control in field crops. *Agronomy*, vol. 10, no. 4, DOI:10.3390/agronomy10040475.
- [4] Perkins, D.B., Abi-Akar, F., Goodwin, G., Brain, R.A. (2022). Characterization of field-scale spray drift deposition and non-target plant biological sensitivity: A corn herbicide (mesotrione/s-metolochlor) case study. *Pest Management Science*, vol. 78, no. 7, p. 3193-3206, DOI:10.1002/ps.6950.
- [5] Duga, A.T., Delele, M.A., Ruysen, K., Dekeyser, D., Nuyttens, D., Bylemans, D., Nicolai, B.M., Verboven, P. (2017). Development and validation of a 3D CFD model of drift and its application to air-assisted orchard sprayers. *Biosystems Engineering*, vol. 154, p. 62-75, DOI:10.1016/j.biosystemseng.2016.10.010.
- [6] Ozkan, H.E., Miralles, A., Sinfort, C., Zhu, H., Fox, R.D. (1997). Shields to reduce spray drift. *Journal of Agricultural Engineering Research*, vol. 67, no. 4, p. 311-322, DOI:10.1006/jaer.1997.0174.
- [7] Tsay, J., Ozkan, H.E., Fox, R.D., Brazee, R.D. (2002). CFD simulation of mechanical spray shields. *Transactions of the ASAE*, vol. 45, no. 5, p. 1271-1280, DOI:10.13031/2013.11055.
- [8] Hong, S.-W., Zhao, L., Zhu, H. (2018). CFD simulation of airflow inside tree canopies discharged from air-assisted sprayers. *Computers and Electronics in Agriculture*, vol. 149, p. 121-132, DOI:10.1016/j.compag.2017.07.011.
- [9] Ellis, M.C.B., Lane, A.G., O'Sullivan, C.M., Jones, S. (2021). Wind tunnel investigation of the ability of drift-reducing nozzles to provide mitigation measures for bystander exposure to pesticides. *Biosystems Engineering*, vol. 202, p. 152-164, DOI:10.1016/j.biosystemseng.2020.12.008.
- [10] Li, H., Wang, J., Wang, P., Liu, J., Yuan, X., Han, H. (2022). Effect of the installation angle of nozzle on the atomizing performance of air-assisted spraying dust suppression device. *Atmosphere*, vol. 13, no. 4, DOI:10.3390/atmos13040520.
- [11] Han, H., Wang, P., Liu, R., Tian, C. (2020). Experimental study on atomization characteristics and dust-reduction performance of four common types of pressure nozzles in underground coal mines. *International Journal of Coal Science & Technology*, vol. 7, no. 3, p. 581-596, DOI:10.1007/s40789-020-00329-w.
- [12] Wang, P., Shi, Y., Zhang, L., Li, Y. (2019). Effect of structural parameters on atomization characteristics and dust reduction performance of internal-mixing air-assisted atomizer nozzle. *Process Safety and Environmental Protection*, vol. 128, p. 316-328, DOI:10.1016/j.psep.2019.06.014.
- [13] Brown, R.B., Sidahmed, M.M. (2001). Simulation of spray dispersal and deposition from a forestry airblast sprayer - part II: Droplet trajectory model. *Transactions of the ASAE*, vol. 44, no. 1, p. 11-17, DOI:10.13031/2013.2298.
- [14] Sakakibara, N., Manabe, Y., Hiromoto, Y., Kobayashi, Y. (2008). Development of high quality thermal spraying process by shielding control. *Science and Technology of Welding and Joining*, vol. 13, no. 4, p. 344-348, DOI:10.1179/174329307x236887.
- [15] Hong, S.-W., Zhao, L., Zhu, H. (2018). CFD simulation of pesticide spray from air-assisted sprayers in an apple orchard: Tree deposition and off-target losses. *Atmospheric Environment*, vol. 175, p. 109-119, DOI:10.1016/j.atmosenv.2017.12.001.
- [16] Bonds, J.A.S., Leggett, M. (2015). A literature review of downwind drift from airblast sprayers: Development of standard methodologies and a drift database. *Transactions of the ASABE*, vol. 58, no. 6, p. 1471-1477, DOI:10.13031/trans.58.11057.
- [17] Salcedo, R., Vallet, A., Granell, R., Garcera, C., Molto, E., Chueca, P. (2017). Eulerian-Lagrangian model of the behaviour of droplets produced by an air-assisted sprayer in a citrus orchard. *Biosystems Engineering*, vol. 154, p. 76-91, DOI:10.1016/j.biosystemseng.2016.09.001.
- [18] Lv, X., Fu, X., Song, J., He, X. (2011). Influence of spray operating parameters on spray drift. *Transactions of the CSAM*, vol. 42, no. 1, p. 59-63, DOI:10.3969/j.issn.1000-1298. (in Chinese)
- [19] Wang, C., He, X., Zeng, A., Andreas, H., Supakorn, W., Qiao, B. (2020). Measuring method and experiment on spray drift of chemicals applied by uav sprayer based on an artificial orchard test bench. *Transactions of the CSAE*, vol. 36, no. 13, p. 56-66, DOI:10.11975/j.issn.1002-6819.2020.13.007. (In Chinese)

Vsebina

Strojniški vestnik - Journal of Mechanical Engineering
letnik 69, (2023), številka 9-10
Ljubljana, september-oktober 2023
ISSN 0039-2480

Izhaja dvomesečno

Razširjeni povzetki (extended abstracts)

- Andrzej Perek, Elżbieta Kawecka, Aleksandra Radomska-Zalas, Frank Pude: Optimizacija rezanja z abrazivnim vodnim curkom po metodi CODAS ob upoštevanju medsebojno odvisnih parametrov obdelave SI 41
- Dragan Rodić, Marin Gostimirović, Milenko Sekulić, Borislav Savković, Andjelko Aleksić: Uporaba mehke logike za napovedovanje površinske hrapavosti po elektroerozijski obdelavi titanove zlitine s primešanim prahom SI 42
- Jamuna Elangandhi, Suresh Periyagounder, Mahalingam Selavaraj, Duraisivam Saminatharaja: Analiza mehanskih in mikrostrukturnih lastnosti kompozita z bakreno matrico in ojačitvijo B4C/W po varjenju z gnetenjem SI 43
- Amjad Alsakarneh, Lina Momani, Taha Tabaza: Modeliranje plinskih hladilnih ciklov z mehko logiko in v okolju Matlab/Simulink SI 44
- Qun Ma, Xiangwei Zhang: Raziskava analitične metode za določitev sil pri hladnem tolkalnem valjanju večutornih gredi SI 45
- Longfei Li, Xin He, Taowei Jiao, Yumeng Xiao, Xipan Wei, Wei Li: Zasnova in optimizacija dežnikastega ščita s tehnologijo simulacij 3D CFD SI 46

Optimizacija rezanja z abrazivnim vodnim curkom po metodi CODAS ob upoštevanju medsebojno odvisnih parametrov obdelave

Andrzej Perec^{1,*} – Elżbieta Kawecka¹ – Aleksandra Radomska-Zalas¹ – Frank Pude^{2,3}

¹ Univerza Jakoba iz Paradiža, Tehniška fakulteta, Gorzów Wielkopolski, Poljska

² Steinbeis Consulting Center High-Pressure Waterjet Technology, Horgau, Nemčija

³ Inspire AG (ETH Zürich), Zürich, Švica

Optimizacija regulacijskih parametrov se uporablja takrat, ko lahko več omenjenih parametrov znatno vpliva na rezultate obdelave. Rezanje z abrazivnim vodnim curkom (AWJ) je ena od uvoženih metod, ki se uvršča med napredne proizvodne tehnologije. Slabo zasnovani procesi so lahko dragi in časovno zamudni, zato je treba z optimizacijo poskrbeti za njihovo učinkovitost, kakovost in uspešnost. Optimizacija regulacijskih parametrov procesa obdelave AWJ je ključna za doseganje zelenih rezultatov rezanja z največjo učinkovitostjo in kakovostjo ter z najmanjšo količino odpadkov.

Obstajajo različne študije na temo optimizacije rezalnih parametrov (vključno z globino rezanja in hrapavostjo površine reže), uporabe različnih metod kot so Entropy/CODAS, VIKOR, metoda odzivnih površin, ter uporabe tehnik večkriterijskega odločanja kot so CODAS, ARAS in funkcijska analiza zaželenosti. Omenjene študije obravnavajo rezanje materialov kot so običajna jekla, protiobrabno obstojna konstrukcijska jekla, orodna jekla, Inconel 718 in superzlitine. Metoda CODAS je bila sicer uporabljena tudi na drugih področjih, ni pa je bilo mogoče zaslediti na področju optimizacije rezanja z abrazivnim vodnim curkom. Na ta način se torej odpirajo priložnosti za nove raziskave.

Namen članka je uporaba metode Entropy/CODAS za določitev optimalne kombinacije regulacijskih parametrov za maksimalno globino reza, minimalno hrapavost površin ter opredelitev vpliva vsakega reguliranega parametra na globino rezanja, širino reže in njeno površinsko hrapavost.

Preskusi so bili opravljeni na obdelovalnem centru WaterJet CNC OMAX 60120. Vodni curek je bil usmerjen pravokotno na obdelovanec in se je premikal linearno z določeno hitrostjo. Z izbiro primerne debeline preizkušancev je bilo preprečeno popolno ločevanje materiala za točno določitev globine reza.

Za proces rezanja jekla 18CrNiMo7-6 z abrazivnim vodnim curkom so bili izbrani ti parametri; tlak: 360 MPa, 380 MPa, 400 MPa, hitrost pomika: 50 mm/min; 150 mm/min in 250 mm/min, pretok vode z abrazivom: 250 g/min; 350 g/min in 450 g/min, abrazivni material: granat #80 (drobljen), notranji premer vodne šobe: 0,33 mm, notranji premer fokusirne šobe: 0,76 mm in oddaljenost: 2 mm.

Rezultati so prikazani v tabelah, med drugim izračun vpliva normalizacije, vrednosti utežene normalizirane zmogljivosti, evklidske in 'taxicab' razdalje za alternative, faktor ocene in rangiranje.

Pri izračunu H_i velja, da višje vrednosti predstavljajo boljši status. Od vseh vrednosti H_i smo najboljšo kombinacijo in zato priporočeno vrednost v okvirju referenčne sekvence dokazali z naslednjimi parametri. Optimalni pogoji za doseganje zelene globine reza in površinske hrapavosti, ki so bili doseženi pri teh parametrih, so: pretok abraziva: 350 g/min, tlak: 400 MPa, in hitrost pomika: 50 mm/min.

Opravljen raziskava potrjuje primernost uporabe metode za večkriterijsko optimizacijo procesa rezanja jekla 18CrNiMo7-6 z abrazivnim vodnim curkom. Metoda CODAS pretvori več lastnosti rezalnega procesa v posamezne količnike H_i , s čimer je bistveno poenostavljeno računanje. Optimalne kombinacije spremenljivk obdelave so rangirane glede na rezultate izračunov.

Prihodnje študije bodo zajele tudi vpliv ostalih regulacijskih parametrov.

Ključne besede: rezanje z abrazivnim vodnim curkom, optimizacija procesa, metoda CODAS, največja globina reza, najmanjša površinska hrapavost

Uporaba mehke logike za napovedovanje površinske hrapavosti po elektroerozijski obdelavi titanove zlitine s primešanim prahom

Dragan Rodić* – Marin Gostimirović – Milenko Sekulić – Borislav Savković – Andjelko Aleksić

Univerza v Novem Sadu, Fakulteta tehniških znanosti, Srbija

Elektroerozijska obdelava (EDM) spada med najbolj napredne obdelovalne postopke in se uspešno uporablja za obdelavo težavnih materialov v različnih industrijskih aplikacijah. Izbrana titanova zlitina je zaradi svojih izjemnih lastnosti, kot sta obstojnost proti visokim temperaturam in koroziji, prisotna v letalski in vesoljski industriji, v biomedicini in na mnogih drugih področjih. Elektroerozijska obdelava omenjenega materiala je zahtevna in še ni dovolj raziskana. Uporabnost EDM je trenutno omejena zaradi razmeroma nizke produktivnosti in pomanjkljive kakovosti površin. Rezultate EDM je mogoče izboljšati z dodajanjem električno prevodnega prahu v dielektrik. Tak postopek odnašanja materiala se imenuje elektroerozijska obdelava s primešanim prahom (PMEDM) in lahko pomembno prispeva h kakovosti elektroerozijske obdelave titanovih zlitin.

Objav na temo PMEDM sicer ne manjka, vseeno pa še ni jasnega odgovora na vprašanje, katera kombinacija koncentracije prahu in vhodnih parametrov procesa daje najbolj kakovostne površine. Glavni cilj študije je zato prispevek k razvoju adaptivnega nevro-mehkega inferenčnega sistema za napovedovanje površinske hrapavosti pri PMEDM titanovih zlitin. Uporabljena je bila tehnika centralne kompozitne zasnovne eksperimentov (CCD). Izbrani variabilni parametri PMEDM so bili tok razelektritve, trajanje impulza, impulzni faktor in koncentracija grafitnega prahu. Pred načrtovanjem glavnega eksperimenta je treba določiti razpon spreminjanja vhodnih parametrov obdelave ter vrednosti drugih dejavnikov, ki med preizkusi ostanejo konstantne. Primerni pogoji za PMEDM so bili določeni na podlagi razpoložljive literature in preliminarnih eksperimentalnih študij.

Z orodjem ANFIS je bil na podlagi načrta CCD postavljen pametni model za napovedovanje površinske hrapavosti titanovih zlitin PMEDM. Prvi tip napake, ki je bil analiziran med razvojem modela, je bila srednja kvadratna napaka (MSE), ki je med učenjem in preizkušanjem modela znašala $2,293 \cdot 10^{-5}$ oz. 0,4509. Poleg MSE je bila izračunana tudi srednja absolutna napaka MAE za kvantitativno ovrednotenje sposobnosti napovedovanja v obliki odstotne vrednosti odstopanj med pridobljenimi in pričakovanimi vrednostmi. Napaka modela po učenju in preizkusih je znašala 1,11 %, kar je bilo pričakovano glede na to, da so bili za učenje modela uporabljeni prav ti podatki. Povprečna vrednost v eksperimentih za potrditev modela je znašala 10,46 %. Poleg analize osnovnih tipov napak je bila opravljena tudi potrditev modela z determinacijskim koeficientom in po metodi Bland-Altman. Model ANFIS je bil razen za napovedovanje rezultatov uporabljen tudi za analizo vpliva vhodnih parametrov. Ugotovljeno je bilo, da ima največji vpliv na površinsko hrapavost tok razelektritve. Analiza variance je pokazala, da je drugi najvplivnejši parameter trajanje impulza, sledita pa mu grafitni prah in impulzni faktor. Preizkušen je bil tudi vpliv grafitnega prahu. Največje, 27-odstotno zmanjšanje površinske hrapavosti, je bilo doseženo pri koncentraciji 12 g/l in toku razelektritve 4,5 A.

Pričujoča raziskava pokriva le manjši del področja PMEDM, praktična uporabnost njenih rezultatov pa je zato omejena le na kontekst opravljenih eksperimentov. Predmet prihodnjih raziskav na področju modeliranja PMEDM bo lahko preizkušanje postopka obdelave PMEDM na titanovih zlitinah z večjim številom in razponom vhodnih dejavnikov, kakor tudi z različnimi globlinami erozije. Na rezultate PMEDM bi lahko vplivala tudi granulacija grafitnega prahu kot eden od vhodnih dejavnikov.

Študija odgovarja na vprašanje o koncentraciji grafitnega prahu, ki ima največji vpliv na površinsko hrapavost pri določenih vhodnih parametrih. Glavni prispevek študije je razkrivanje kompleksnih odvisnosti med spremenljivimi vhodnimi parametri (tok razelektritve, trajanje impulza, impulzni faktor in koncentracija grafitnega prahu) ter rezultati PMEDM obdelave (površinska hrapavost) titanove zlitine. Študija tako odgovarja na nekatera nerazrešena raziskovalna vprašanja in potrjuje uporabnost predlagane metode v industriji.

Ključne besede: ANFIS, tok razelektritve, trajanje impulza, impulzni faktor, grafitni prah

Analiza mehanskih in mikrostrukturnih lastnosti kompozita z bakreno matrico in ojačitvijo B₄C/W po varjenju z gnetenjem

Jamuna Elangandhi¹ – Suresh Periyagounder² – Mahalingam Selavaraj³ – Duraisivam Saminatharaja¹

¹ Tehniški kolidž Kavery, Oddelek za strojništvo, Indija

² Tehniški kolidž Sona (avtonomni), Oddelek za mehatroniko, Indija

³ Tehniški kolidž Sona (avtonomni), Oddelek za strojništvo, Indija

Kompozitni materiali z bakreno matrico (CMC) so razširjeni v različnih aplikacijah na področju letalske in vesoljske industrije, avtomobilske industrije in elektronike. Konvencionalno varjenje CMC je zaradi kristalne strukture kompozita zelo težavno in drago. Varjenje z gnetenjem (FSW) je obetaven in zanesljiv alternativni postopek varjenja in v članku so zato analizirane lastnosti materiala CMC po varjenju z omenjenim postopkom. Čisti baker (Cu) je bil ojačen z delci volframa (W) in borovega karbida (B₄C) v različnih kombinacijah, nato pa je bilo opravljeno poskusno varjenje kompozita z gnetenjem za preučitev mehanskih in mikrostrukturnih lastnosti.

Za določitev optimalne kombinacije parametrov sta bili uporabljeni metodi večkriterijskega odločanja TOPSIS (tehnika razvrstitve po podobnosti z idealno rešitvijo) in GRA (siva relacijska analiza).

Eksperimenti so bili zasnovani z ortogonalnim poljem L16, vplivni parametri pa so bili odstotni delež ojačitve z B₄C, vrtilna hitrost orodja, varilna hitrost in aksialna sila.

Rezultati so bili ovrednoteni na podlagi naslednjih odgovorov: natezna trdnost, trdota in udarna trdnost zvarnega spoja. Rezultati analiz TOPSIS in GRA so pokazali, da znašajo varilni parametri za optimalno mehansko trdnost 15 % delež ojačitve z B₄C, vrtilna hitrost 900 obr./min, varilna hitrost 15 mm/min in aksialna sila 6 kN.

Opravljena je bila tudi preiskava mikrostrukturnih sprememb po varjenju pod vrstičnim elektronskim mikroskopom (SEM).

Ključne besede: varjenje z gnetenjem, baker, kompozitni material s kovinsko osnovo, borov karbid

Modeliranje plinskih hladilnih ciklov z mehko logiko in v okolju Matlab/Simulink

Amjad Alsakarneh^{1,*} – Lina Momani² – Taha Tabaza³

¹ Tehnološka fakulteta Hijjawi, Univerza Yarmouk, Jordanija

² Višji tehniški kolidž, Oddelek za strojništvo, Združeni arabski emirati

³ Jordanska univerza Al-Zaytoonah, Oddelek za strojništvo, Jordanija

Članek obravnava oceno hladilnega števila (COP) plinskih hladilnih ciklov na podlagi dveh različnih pristopov: z modeliranjem v okolju Matlab/Simulink in z mehko logiko. Metodi prinašata dragocene uvide v učinkovitost in uporabnost tehnik za ocenjevanje COP.

Raziskava se je začela z razvojem celovitega modela v okolju Matlab/Simulink za natančno računanje COP in primerjavo s teoretičnimi podatki. Model tako predstavlja zanesljivo merilo za vrednotenje zmogljivosti plinskih hladilnih ciklov. Uporabljena je bila tudi mehka logika za oceno COP pri poljubnih vrednostih tlaka, s čimer je analiza postala bolj prilagodljiva.

Rezultati študije razkrivajo močno korelacijo med modelom v okolju Matlab/Simulink in teoretičnimi vrednostmi ter tako potrjujejo njegovo točnost in robustnost. Pristop z mehko logiko je podobno posebej primeren za ocenjevanje vrednosti COP in se tako ponuja kot alternativna metoda za analiziranje plinskih hladilnih ciklov. Ugotovitve potrjujejo vsestranski potencial modelov v okolju Matlab/Simulink in tehnik mehke logike na področju termodinamike.

Razvoj modela plinskega hladilnega cikla v okolju Matlab/Simulink je podrobno opisan. Najprej so bile umerjene različne termodinamične lastnosti zraka, vključno z entalpijo (h), relativnim tlakom (p_r) in temperaturo (T). Za natančen model entalpije in njegovo oblikovanje sta bila uporabljena potenčna funkcija in komplet orodij za iskanje krivulj najboljšega priloga v Matlabu. Točnost modela je bila ovrednotena z izračunom korena srednje kvadratne napake (RMSE). Odstopanje od teoretičnih podatkov je bilo manjše od 1 %. Z istim kompletom orodij so bile izpeljane tudi odvisnosti med relativnim tlakom in temperaturo oz. med temperaturo in relativnim tlakom. Vrednost RMSE za izpeljane enačbe je pod 1,5 %, kar pomeni odlično ujemanje z izvirnimi podatki. Omenjene funkcije najboljšega priloga so bile tudi osnova za razvoj celovitega modela plinskega hladilnega cikla v okolju Simulink. Vhodni veličini sta vrednosti nizkega in visokega tlaka, izhodna veličina pa je COP. Model Simulink zajema več podsistemov, vključno s kompresorjem, turbino in uparjalnikom. Zrak vstopa v podsistem kompresorja z začetno temperaturo 285 K in tlakom ene atmosfere. Termodinamične lastnosti za izračune so bile določene z izpeljanimi enačbami. Podobni izračuni so bili opravljeni tudi za podsistem turbine, v katerega vstopa zrak iz kondenzatorja v tretjem stanju in iz njega izstopa v četrtem stanju. Model uparjalnika omogoča izračun absorbirane energije v kondenzatorju.

Predstavljen je tudi alternativni model za ocenjevanje COP s pomočjo mehke logike. Model v okolju Matlab/Simulink in model z mehko logiko uporabljata za vhodni veličini nizki in visoki tlak, izhodna veličina pa je COP. S tem izboljšujeta razumevanje plinskih hladilnih ciklov in možnosti za njihovo analizo. Sledi sklep, da sta oba pristopa primerna za natančno ocenjevanje COP, pri čemer ima model z mehko logiko izjemno stopnjo korelacije s simulirano vrednostjo COP (RMSE < 2 %). Mehka logika v primerjavi z okoljem Matlab/Simulink torej omogoča učinkovito modeliranje hladilnih ciklov tudi z manj predhodnega znanja.

Raziskava tako podaja dragocene ugotovitve, ki bodo lahko osnova za nadaljnje študije na tem področju. Omogoča tudi integracijo strategij za krmiljenje hladilnih ciklov na podlagi razvitega modela v okolju Matlab/Simulink za dodatno optimizacijo zmogljivosti. Z izboljšanjem kakovosti podatkov bo mogoče izpopolniti model na podlagi mehke logike in razširiti njegovo uporabnost. Upoštevati pa je treba tudi omejitve raziskave, kot sta osredotočenost na plinske hladilne cikle in subjektivna narava gradnje modelov na podlagi mehke logike.

Ključne besede: hladilno število, Matlab/Simulink, Takagi-Sugeno-Kang, hladilni cikli

Raziskava analitične metode za določitev sil pri hladnem tolkalnem valjanju večutornih gredi

Qun Ma* – Xiangwei Zhang

Znanstveno-tehniška šola za vojaško orožje, Tehniška univerza Xi'an, Kitajska

Hladno tolkalno valjanje je učinkovit postopek za plastično preoblikovanje kovine pri izdelavi večutornih gredi. Dva valja z visoko hitrostjo valjata kovino s prekinitvami, kovina pa se pri tem plastično deformira in nastanejo utori, ki ustrezajo obliki profila valjev. V članku je za preučitev procesa deformacije kovine ter za točno in učinkovito določitev parametrov sil in energije pri hladnem tolkalnem valjanju postavljen diskreten analitični model, ki omogoča izračun poteka preoblikovalne sile pri hladnem tolkalnem valjanju.

Preučena so bila gibanja med preoblikovanjem in lastnosti v coni deformacije kovine. Proces hladnega tolkalnega valjanja je bil diskretiziran na podlagi spreminjanja lokacije in parametrov deformacijske cone v kovini. Sila preoblikovanja v vsaki diskretni točki je bila izračunana po metodi glavnih napetosti. Končno je bil postavljen še diskreten analitični model za izračun sil pri obravnavanem procesu.

Deformiranje kovine je bilo simulirano v programskem paketu za analize po metodi končnih elementov DEFORM-3D in izračunana je bila sila pri preoblikovanju. Valj je bil modeliran kot togo telo, obdelovanec pa kot plastično telo. Analiza lastnosti deformacijske cone v kovini je bila tudi eksperimentalno verificirana. Za potrebe izvedbe eksperimentalnega hladnega tolkalnega valjanja in meritev je bil predelan horizontalni rezkalni stroj. Izdelan je bil valj, ki je bil vpet v vreteno horizontalnega rezkalnega stroja. Sila pri preoblikovanju je bila izmerjena s triosnim senzorjem PCB261A03.

Radialna sila, določena s simulacijo po metodi končnih elementov in eksperimentalno, je veliko večja od tangencialne sile, za verifikacijo diskretnega analitičnega modela pa je bila zato upoštevana samo radialna sila. Napaka maksimalne vrednosti radialne sile, izračunane po diskretnem analitičnem modelu, je znašala 7 % v primerjavi z rezultati simulacije po metodi končnih elementov oz. 4 % v primerjavi z rezultati eksperimentov. Trend spremenljive radialne sile, izračunan z diskretnim analitičnim modelom, se ujema z rezultati simulacije po metodi končnih elementov in z rezultati eksperimentov. Tudi čas hladnega tolkalnega valjanja, izračunan z diskretnim analitičnim modelom, se ujema z rezultati simulacije po metodi končnih elementov, od rezultatov eksperimentov pa je manjši. Diskretni analitični model in simulacija po metodi končnih elementov ne upoštevata vpliva elastične deformacije in trenja valja, prav tako pa ne zajemata oblike kovine po deformaciji. Čas hladnega tolkalnega valjanja je zato razmeroma kratek.

Opis kompleksnega procesa plastične deformacije kovin je v vsakem primeru težaven matematični problem, saj so lega in parametri deformacijske cone v kovini odvisni od časa. Trenutno se večina raziskav izvaja s simulacijami po metodi končnih elementov, saj ni ustreznih analitičnih modelov ali empiričnih formul. Z diskretizacijo kontinuirnega procesa deformacije kovine in obravnavo posameznih časovnih rezin je mogoče postaviti točen analitični model. Celoten deformacijski proces je mogoče popisati z numeričnim iskanjem najboljšega priloga na diskretnih rezultatih. Diskretni analitični model za hitro in točno določitev sil pri hladnem tolkalnem valjanju je lahko v pomoč pri raziskavah parametrov postopka in pri razvoju opreme, zato ima veliko tehnično aplikativno vrednost.

Simulacije po metodi končnih elementov lahko v primerjavi z analitičnimi modeli zajamejo celoten proces deformacije kovine, rezultati pa so bolj intuitivni in podrobni. Raziskave bo v prihodnje mogoče usmeriti v kombiniranje s simulacijami po metodi končnih elementov, preučitev procesa deformacije kovin in oblik po deformaciji, zajeti pa bo treba tudi vpliv elastične deformacije valja. Z omenjenimi raziskavami bo mogoče še dodatno optimizirati diskretni analitični model.

Ključne besede: diskretna analitična metoda, hladno tolkalno valjanje, preoblikovalna sila, deformacijska cona, simulacija po metodi končnih elementov, radialna sila

Zasnova in optimizacija dežnikastega ščita s tehnologijo simulacij 3D CFD

Longfei Li¹ – Xin He¹ – Taowei Jiao¹ – Yumeng Xiao¹ – Xipan Wei^{1,2} – Wei Li^{1,*}

¹ Severozahodna univerza A&F, Kolidž za strojništvo in elektrotehniko, Kitajska

² Weichai Power Co., Ltd, Kitajska

Človeštvo že dolgo uporablja škropljenje s pesticidi za nadzor nad škodljivci in plevelom. Pod vplivom zunanjih dejavnikov, kot so naravni vetrovi, pa se večina odloženih pesticidov ne oprime površine rastlin. Namesto tega pronicajo v zemljo in podtalnico, kjer povzročajo hude težave z onesnaženjem okolja. Mehanski ščiti so usmerjevalni pripomočki, ki se vgradijo v bližini škropilnih šob ter predstavljajo ceneno in učinkovito sredstvo za izboljšanje izkoristka pesticidov. Delujejo tako, da s spremembo hitrosti in smeri zračnega toka v bližini škropilnih šob spremenijo trajektorijo kapljic tekočine. Tradicionalne eksperimentalne metode, ki se uporabljajo za vrednotenje zmogljivosti ščitov, so povezane z dolgotrajnimi raziskavami in razvojem, visokimi stroški ter težavami pri vizualizaciji vplivov.

Pričujoča študija naslavlja omenjene izzive z uporabo metode računalniške dinamike fluidov (CFD). Uporabljena je bila programska oprema Ansys za temeljito analizo mehanizmov za preprečevanje drifta, podrobno preučitev zračnih tokov v okolici in konstruiranje visokonatančnega simulacijskega modela. Podrobno so bile preučene aerodinamične lastnosti šestih različnih vrst ščitov in predstavljena je primerjava njihove učinkovitosti pri preprečevanju drifta.

Najboljše rezultate daje ščit v obliki dežnika. Nato je bil postavljen simulacijski model CFD. Po opredelitvi ustreznih parametrov v paketu Fluent je bila opravljena optimizacija dimenzij in delovnih parametrov ščita po metodi odzivnih površin. Pri premeru izstopa $R = 521$ mm, premeru vstopa pomožnega zraka $r = 307$ mm, višini $h = 241$ mm, hitrosti ventilatorja $N = 2700$ obr./min, razdalji med šobo in izstopno ravnino ščita $H = 150$ mm in tlaku škropljenja $P = 0,3$ MPa se je vrednost DR povečala na 77,31 %. Terenski poskusi so pokazali, da se je vrednost DR med konvencionalnim škropljenjem pri hitrosti vetra 5 m/s znižala za 31,9 % v primerjavi s 3 m/s, medtem ko se je vrednost DR pri škropljenju s ščitom pri 5 m/s zmanjšala za samo 3,6 % v primerjavi s 3 m/s, kar dokazuje odlično delovanje mehanskih ščitov.

Rezultati terenskih preskusov se ujemajo z rezultati simulacij CFD. Relativno odstopanje DR med omenjenimi rezultati je bilo znotraj 4 %, s čimer sta bili dokazani točnost in zanesljivost simulacijskega modela CFD. Pričujoča študija ima omejitve kakor vse druge – razmere na polju se stalno spreminjajo, medtem ko so bili pogoji v tej študiji konstantni. Študija v zvezi z dejanskimi aritmetičnimi pogoji ne upošteva trkov in odbojev med kapljicami v meglici in rastlinami.

V prihodnjih raziskavah bo mogoče raziskati sočasno delovanje več škropilnih šob s kombiniranjem interakcij med kapljicami meglice in rastlinami. Članek tako bolj točno razkriva mehanizem delovanja mehanskega ščita z uporabo metode 3D CFD pri snovanju in optimizaciji dežnikastega ščita. Predlagana metoda predstavlja novo praktično uporabo metode CFD za intuitivno preučevanje mehanizmov preprečevanja drifta s ščiti in dodatno izboljšanje njihovega učinka. Metoda je primerna za snovanje in optimizacijo mehanskih ščitov. Z zasnovo in optimizacijo ščita po predstavljeni metodi je mogoče prihraniti veliko časa, naporov in stroškov zaradi zagotovljene natančnosti, to pa prinaša široko uporabnost in solidno teoretično podlago za raziskave mehanskih ščitov.

Ključne besede: mehanski ščit, mehanizem za preprečevanje drifta, računalniška dinamika fluidov, aerodinamične lastnosti, stopnja odlaganja kapljic, metoda odzivnih površin

Guide for Authors

All manuscripts must be in English. Pages should be numbered sequentially. The manuscript should be composed in accordance with the Article Template given above. The suggested length of contributions is 10 to 20 pages. Longer contributions will only be accepted if authors provide justification in a cover letter. For full instructions see the Information for Authors section on the journal's website: <http://en.sv-jme.eu>.

SUBMISSION:

Submission to SV-JME is made with the implicit understanding that neither the manuscript nor the essence of its content has been published previously either in whole or in part and that it is not being considered for publication elsewhere. All the listed authors should have agreed on the content and the corresponding (submitting) author is responsible for having ensured that this agreement has been reached. The acceptance of an article is based entirely on its scientific merit, as judged by peer review. Scientific articles comprising simulations only will not be accepted for publication; simulations must be accompanied by experimental results carried out to confirm or deny the accuracy of the simulation. Every manuscript submitted to the SV-JME undergoes a peer-review process.

The authors are kindly invited to submit the paper through our web site: <http://ojs.sv-jme.eu>. The Author is able to track the submission through the editorial process - as well as participate in the copyediting and proofreading of submissions accepted for publication - by logging in, and using the username and password provided.

SUBMISSION CONTENT:

The typical submission material consists of:

- A **manuscript** (A PDF file, with title, all authors with affiliations, abstract, keywords, highlights, inserted figures and tables and references),
- Supplementary files:
 - a **manuscript** in a WORD file format
 - a **cover letter** (please see instructions for composing the cover letter)
 - a ZIP file containing **figures** in high resolution in one of the graphical formats (please see instructions for preparing the figure files)
 - possible **appendices** (optional), cover materials, video materials, etc.

Incomplete or improperly prepared submissions will be rejected with explanatory comments provided. In this case we will kindly ask the authors to carefully read the Information for Authors and to resubmit their manuscripts taking into consideration our comments.

COVER LETTER INSTRUCTIONS:

Please add a **cover letter** stating the following information about the submitted paper:

1. Paper **title**, list of **authors** and their **affiliations**. **One** corresponding author should be provided.
2. **Type of paper**: original scientific paper (1.01), review scientific paper (1.02) or short scientific paper (1.03).
3. A **declaration** that neither the manuscript nor the essence of its content has been published in whole or in part previously and that it is not being considered for publication elsewhere.
4. State the **value of the paper** or its practical, theoretical and scientific implications. What is new in the paper with respect to the state-of-the-art in the published papers? Do not repeat the content of your abstract for this purpose.
5. We kindly ask you to suggest at least two **reviewers** for your paper and give us their names, their full affiliation and contact information, and their scientific research interest. The suggested reviewers should have at least two relevant references (with an impact factor) to the scientific field concerned; they should not be from the same country as the authors and should have no close connection with the authors.
6. Please confirm that authors are willing/able to pay the Open Access **publication fee** as indicated in the Guide for Authors under Publication Fee, available at <https://www.sv-jme.eu/guide-for-authors-online/>.

FORMAT OF THE MANUSCRIPT:

The manuscript should be composed in accordance with the Article Template. The manuscript should be written in the following format:

- A **Title** that adequately describes the content of the manuscript.
- A list of **Authors** and their **affiliations**.
- An **Abstract** that should not exceed 250 words. The Abstract should state the principal objectives and the scope of the investigation, as well as the methodology employed. It should summarize the results and state the principal conclusions.
- 4 to 6 significant **key words** should follow the abstract to aid indexing.
- 4 to 6 **highlights**; a short collection of bullet points that convey the core findings and provide readers with a quick textual overview of the article. These four to six bullet points should describe the essence of the research (e.g. results or conclusions) and highlight what is distinctive about it.
- An **Introduction** that should provide a review of recent literature and sufficient background information to allow the results of the article to be understood and evaluated.
- A **Methods** section detailing the theoretical or experimental methods used.
- An **Experimental section** that should provide details of the experimental set-up and the methods used to obtain the results.
- A **Results** section that should clearly and concisely present the data, using figures and tables where appropriate.
- A **Discussion** section that should describe the relationships and generalizations shown by the results and discuss the significance of the results, making comparisons with previously published work. (It may be appropriate to combine the Results and Discussion sections into a single section to improve clarity.)
- A **Conclusions** section that should present one or more conclusions drawn from the results and subsequent discussion and should not duplicate the Abstract.
- **Acknowledgement** (optional) of collaboration or preparation assistance may be included. Please note the source of funding for the research.
- **Nomenclature** (optional). Papers with many symbols should have a nomenclature that defines all symbols with units, inserted above the references. If one is used, it must contain all the symbols used in the manuscript and the definitions should not be repeated in the text. In all cases, identify the symbols used if they are not widely recognized in the profession. Define acronyms in the text, not in the nomenclature.
- **References** must be cited consecutively in the text using square brackets [1] and collected together in a reference list at the end of the manuscript.
- **Appendix(-ices)** if any.

SPECIAL NOTES

Units: The SI system of units for nomenclature, symbols and abbreviations should be followed closely. Symbols for physical quantities in the text should be written in italics (e.g. v , T , n , etc.). Symbols for units that consist of letters should be in plain text (e.g. ms^{-1} , K, min, mm, etc.). Please also see: <http://physics.nist.gov/cuu/pdf/sp811.pdf>.

Abbreviations should be spelt out in full on first appearance followed by the abbreviation in parentheses, e.g. variable time geometry (VTG). The meaning of symbols and units belonging to symbols should be explained in each case or cited in a **nomenclature** section at the end of the manuscript before the References.

Figures (figures, graphs, illustrations digital images, photographs) must be cited in consecutive numerical order in the text and referred to in both the text and the captions as Fig. 1, Fig. 2, etc. Figures should be prepared without borders and on white grounding and should be sent separately in their original formats. If a figure is composed of several parts, please mark each part with a), b), c), etc. and provide an explanation for each part in Figure caption. The caption should be self-explanatory. Letters and numbers should be readable (Arial or Times New Roman, min 6 pt with equal sizes and fonts in all figures). Graphics (submitted as supplementary files) may be exported in resolution good enough for printing (min. 300 dpi) in any common format, e.g. TIFF, BMP or JPG, PDF and should be named Fig1.jpg, Fig2.tif, etc. However, graphs and line drawings should be prepared as vector images, e.g. CDR, AI. Multi-curve graphs should have individual curves marked with a symbol or otherwise provide distinguishing differences using, for example, different thicknesses or dashing.

Tables should carry separate titles and must be numbered in consecutive numerical order in the text and referred to in both the text and the captions as Table 1, Table 2, etc. In addition to the physical quantities, such as t (in italics), the units [s] (normal text) should be added in square brackets. Tables should not duplicate data found elsewhere in the manuscript. Tables should be prepared using a table editor and not inserted as a graphic.

REFERENCES:

A reference list must be included using the following information as a guide. Only cited text references are to be included. Each reference is to be referred to in the text by a number enclosed in a square bracket (i.e. [3] or [2] to [4] for more references; do not combine more than 3 references, explain each). No reference to the author is necessary.

References must be numbered and ordered according to where they are first mentioned in the paper, not alphabetically. All references must be complete and accurate. Please add DOI code when available. Examples follow.

Journal Papers:

Surname 1, Initials, Surname 2, Initials (year). Title. *Journal*, volume, number, pages, DOI code.

- [1] Hackenschmidt, R., Alber-Laukant, B., Rieg, F. (2010). Simulating nonlinear materials under centrifugal forces by using intelligent cross-linked simulations. *Strojniški vestnik - Journal of Mechanical Engineering*, vol. 57, no. 7-8, p. 531-538, DOI:10.5545/sv-jme.2011.013.

Journal titles should not be abbreviated. Note that journal title is set in italics.

Books:

Surname 1, Initials, Surname 2, Initials (year). Title. Publisher, place of publication.

- [2] Groover, M.P. (2007). *Fundamentals of Modern Manufacturing*. John Wiley & Sons, Hoboken.

Note that the title of the book is italicized.

Chapters in Books:

Surname 1, Initials, Surname 2, Initials (year). Chapter title. Editor(s) of book, book title. Publisher, place of publication, pages.

- [3] Carbone, G., Ceccarelli, M. (2005). Legged robotic systems. Kordić, V., Lazinica, A., Merdan, M. (Eds.), Cutting Edge Robotics. Pro literatur Verlag, Mammendorf, p. 553-576.

Proceedings Papers:

Surname 1, Initials, Surname 2, Initials (year). Paper title. Proceedings title, pages.

- [4] Štefanič, N., Martinčević-Mikić, S., Tošanović, N. (2009). Applied lean system in process industry. *MOTSP Conference Proceedings*, p. 422-427.

Standards:

Standard-Code (year). Title. Organisation. Place.

- [5] ISO/DIS 16000-6.2:2002. *Indoor Air - Part 6: Determination of Volatile Organic Compounds in Indoor and Chamber Air by Active Sampling on TENAX TA Sorbent, Thermal Desorption and Gas Chromatography using MSD/FID*. International Organization for Standardization. Geneva.

WWW pages:

Surname, Initials or Company name. Title, from <http://address>, date of access.

- [6] Rockwell Automation. Arena, from <http://www.arenasimulation.com>, accessed on 2009-09-07.

EXTENDED ABSTRACT:

When the paper is accepted for publishing, the authors will be requested to send an **extended abstract** (approx. one A4 page or 3500 to 4000 characters or approx. 600 words). The instruction for composing the extended abstract are published on-line: <http://www.sv-jme.eu/information-for-authors/>.

COPYRIGHT:

Authors submitting a manuscript do so on the understanding that the work has not been published before, is not being considered for publication elsewhere and has been read and approved by all authors. The submission of the manuscript by the authors means that the authors automatically agree to publish the paper under CC-BY 4.0 Int. or CC-BY-NC 4.0 Int. when the manuscript is accepted for publication. All accepted manuscripts must be accompanied by a Copyright Agreement, which should be sent to the editor. The work should be original work by the authors and not be published elsewhere in any language without the written consent of the publisher. The proof will be sent to the author showing the final layout of the article. Proof correction must be minimal and executed quickly. Thus it is essential that manuscripts are accurate when submitted. Authors can track the status of their accepted articles on <https://en.sv-jme.eu>.

PUBLICATION FEE:

Authors will be asked to pay a publication fee for each article prior to the article appearing in the journal. However, this fee only needs to be paid after the article has been accepted for publishing. The fee is 380 EUR (for articles with maximum of 6 pages), 470 EUR (for articles with maximum of 10 pages), plus 50 EUR for each additional page. The additional cost for a color page is 90.00 EUR (only for a journal hard copy; optional upon author's request). These fees do not include tax.



<http://www.sv-jme.eu>

Contents

Papers

- 367 Andrzej Perec, Elżbieta Kawecka, Aleksandra Radomska-Zalas, Frank Pude:
Optimization of Abrasive Waterjet Cutting by Using the CODAS Method with Regard to Interdependent Processing Parameters
- 376 Dragan Rodić, Marin Gostimirović, Milenko Sekulić, Borislav Savković, Andjelko Aleksić:
Fuzzy Logic Approach to Predict Surface Roughness in Powder Mixed Electric Discharge Machining of Titanium Alloy
- 388 Jamuna Elangandhi, Suresh Periyagounder, Mahalingam Selavaraj, Duraisivam Saminatharaja:
Mechanical and Microstructural Properties of B4C/W Reinforced Copper Matrix Composite Using a Friction Stir-Welding Process
- 401 Amjad Alsakarneh, Lina Momani, Taha Tabaza:
Fuzzy and Matlab/Simulink Modelling of the Air Compression Refrigeration Cycle
- 409 Qun Ma, Xiangwei Zhang:
Research on an Analytical Method for the Forming Force of External Spline Cold Roll-Beating
- 422 Longfei Li, Xin He, Taowei Jiao, Yumeng Xiao, Xipan Wei, Wei Li:
Design and Optimization of an Umbrella-Type Shield Based on 3D CFD Simulation Technology